universität wien

DISSERTATION / DOCTORAL THESIS

Titel der Dissertation /Title of the Doctoral Thesis

„Simulation of spin-torque driven magnetization dynamics in the diffusive and coherent transport regime“

verfasst von / submitted by

Peter Flauger, MSc

angestrebter akademischer Grad / in partial fulfilment of the requirements for the degree of

Doktor der Naturwissenschaften (Dr. rer. nat.)

Wien, 2022 / Vienna, 2022

Studienkennzahl lt. Studienblatt / degree programme code as it appears on the student record sheet:	UA 796 605 411
Dissertationsgebiet lt. Studienblatt / field of study as it appears on the student record sheet:	Physik / Physics
Betreut von / Supervisor:	Univ.-Prof. Dipl.-Ing. Dr. techn. Dieter Süss, Privatdoz.

Kurzzusammenfassung

(English version on the next page)

Im Kontext mikromagnetischer Betrachtungen ist es ein gängiger Ansatz, das Spin-Drift-Diffusionsmodell mit der Landau-Lifshitz-Gilbert-Gleichung zu koppeln, um das Zusammenspiel von Magnetisierungsdynamik und Spintransport im diffusiven Regime zu beschreiben. In diesem Regime, das auf eine Bandbreite spintronischer Bauelemente in der Größenordnung einiger Mikrometer anwendbar ist, kann das Spin-Diffusionsproblem auf demselben Finite-Differenzen- oder Finite-Elemente-Mesh wie die Magnetisierungsdynamik numerisch gelöst werden. Dabei liegt die Diskretisierungslänge in der Regel nahe der Austauschlänge. Das Spin-Drift-Diffusionsmodell kann jedoch nicht zur Beschreibung magnetischer Tunnelkontakte verwendet werden, denn es ist davon auszugehen, dass der Spin-Transport durch diese kohärent ist. Die Transporteigenschaften werden in diesem Fall aus Lösungen der Schrödinger-Gleichung abgeleitet, was eine Diskretisierung des Transportproblems erforderlich macht, die mindestens eine Größenordnung feiner ist, als es für mikromagnetische Simulationen notwendig wäre. Darüber hinaus erfordert der für die Ermittlung kohärenter Transporteigenschaften bewährte non-equilibrium Green's function-Formalismus rechenintensive Matrizeninversionen.

In dieser Arbeit werden beide Transport-Regime hinsichtlich ihrer Anwendung und der Art und Weise, wie sie mit der Landau-Lifshitz-Gilbert-Gleichung gekoppelt sind, diskutiert und verglichen. Für den diffusiven Grenzfall wird insbesondere die Modifikation der effektiven Dämpfung der Magnetisierungsbewegung durch Spin-Orbit-Torque diskutiert und mit experimentellen Untersuchungen an out-of-plane Pt/Co/Ta-Strukturen unter dem Einfluss eines externen Magnetfelds verglichen.
Für den Fall von kohärentem Transport wird eine performante Lösungsstrategie vorgestellt, die unter Ausnutzung der konstanten Koeffizienten des transportierten Drehmoments eine wiederholte Matrixinversion vermeiden kann.
Die in diesem Rahmen vorgestellten Simulationen der Magnetisierungsdynamik beinhaltet auch eine Untersuchung zweier möglicher Ursachen des sogenannten back-hopping-Effekts in STT-MRAM-Zellen: die quadratische Abhängigkeit des Slonczewski-Drehmomentterms in magnetischen Tunnelkontakten von der Spannung, die zu einer zusätzlichen Hystereseschleife führen kann, und die Destabilisierung des Referenzsystems, die zu einem dynamischen Hin- und Herschalten der Magnetisierung führt.

Abstract

In the context of micromagnetism, it is a common approach to couple the spin-drift diffusion model with the Landau-Lifshitz-Gilbert equation to describe the interplay of magnetization dynamics and spin transport in the diffusive regime. In this limit, that applies to a wide range of spintronic devices on the micron scale, numerical solutions to the spin-diffusion problem can be found on the same finite-differences or finite elements mesh as for the magnetization dynamics, with the discretization length being usually close to the exchange length. However, the spin-drift-diffusion model is not applicable to magnetic tunnel junctions. In them, spin-transport is assumed to be coherent and to be governed by the Schrödinger equation. This requires a discretization at least one order of magnitude smaller than it is required for micromagnetic simulations. Additionally, the matrix inversion that occurs in the non-equilibrium Green's function formalism, a well-known tool to obtain coherent spin-transport properties, is computationally expensive.

In this thesis, both spin-transport limits are discussed and compared with respect to their application and the way they couple to the Landau-Lifshitz-Gilbert equation. In the diffusive limit, the modification of the magnetization's effective damping coefficient by spin-orbit torque is discussed and compared to experimental results obtained for a Pt/Co/Ta structure with out-of-plane anisotropy and an applied external field.
For the coherent transport regime, the outline of a computationally efficient solution strategy is given that circumvents a repeated matrix inversion by taking advantage of the constant nature of the spin-torque coefficients. Coupled simulations of the magnetization dynamics present here also include an assessment of two potential origins of the back-hopping phenomenon in STT-MRAM cells: the quadratic voltage dependence of the dampinglike torque term in magnetic tunnel junctions that can result in an additional hysteresis loop, and the destabilization of the reference layer that leads to a dynamic back-and-forth switching of the magnetization.

Contents

1 Introduction

The development of spintronic read heads contributed significantly to the fast increase in storage capacity of hard disk drives (HDD) since the very early 1990s [1] when the first MR/inductive read-write head was conceived [2]. This hybrid device would still hold on to an inductive write head but introduced a separate anisotropic magnetoresistive (AMR) read head. This was the first utilization of a magnetoresistive (MR) effect in HDDs for reading purposes but was followed up within the same decade by a read head based on the giant magnetoresistance (GMR) effect that was discovered in 1988 by Grünberg [3] and Fert [4] and awarded them the Nobel prize in physics in 2007. In contrast to the AMR effect, the GMR effect only exists in stacks of magnetic materials and dictates that the resistance of such devices is low if the magnetization of the individual layers are in parallel to each other and high if they are in a so-to-speak anti-ferromagnetic configuration. The GMR effect became usable for reading a magnetic recording medium only after successfully decoupling two ferromagnetic layers in the stack, however. This breakthrough was provided by spin-valve structures [5–8] that usually consist of a pinned layer that is anti-ferromagnetically coupled to a reference system and is separated from a free layer by a conducting spacer layer. The magnetic properties of the free layer are such that its magnetization can be easily reversed by the stray field of the hard disc while the reference layer stays put, allowing to associate the resistance of the stack with the magnetization state of the recording medium [9, 10].
The GMR ratio in read heads usually does not exceed 20 percent [11]. Replacing the spacer layer in spin-valve structures by an insulator like MgO can significantly increase the contrast [12] with the underlying effect now being the tunnel magnetoresistance (TMR) [13–15]. TMR spin valves were implemented into HDD read heads only shortly before the recording direction in HDDs was changed from longitudinal to perpendicular [1, 16].

If the free layer of the spin-valve itself is sufficiently stable, a TMR stack could not only be used for read-out purposes but to store information directly. This is the basis of the magnetoresistive random-access memory (MRAM).
From a mesoscopic point of view, the xMR effects described above arise as a result of the magnetization of the ferromagnetic materials interacting with the spin of the conduction electrons. Naturally, this interaction acts in both directions and the free layer magnetization can therefore not only be reversed by an external field but also by the angular momentum transported by the electrons, if the current flow is large enough. This effect is called spin-transfer torque [17–19] (STT). It allows for bi-directional switching in TMR stacks [20] and can therefore be used to write data in MRAM cells [11, 21]. This form of random-access memory is non-volatile and consequently energy-efficient while allowing for fast reading and

writing compared to HDDs.

On the basis of Caroli et al. [22], detailed theoretical assessments of STT in magnetic tunnel junctions (MTJ) based on a free electron model and the tight-binding model within the framework of the Keldysh formalism were done in references [23–26], with the overall form of the obtained torques agreeing qualitatively with experimental findings of Kubota et al. in [27].

The aim of this thesis is to give a detailed comparison of the STT in ballistic MTJs calculated from the Keldysh Green's function formalism based on the work of Datta et. al in reference [28] to torques obtained from the micromagnetic spin-drift diffusion (SDD) model [29] in a diffusive transport regime that applies to a wide variety of spintronic devices. The ballistic transport calculations are then coupled to magnetization dynamics simulations [30] to investigate the back-hopping phenomenon in STT-MRAM [31, 32]. This effect leads to an increase in writing error rates at high voltages and manifests itself in a back and forth switching between the high and low resistance state of the device, posing a problem for reliable MRAM technology.

The thesis is organized as follows: A short introduction in chapter 2 to basic spintronic concepts, namely the spin-accumulation and spin-current, will be followed up in chapter 3 by a discussion of spin torques calculated from the SDD model in a micromagnetic context, including a comparison to simplified models. This discussion will conclude with a comparison of simulations to experimental results on the modulation of the magnetization's damping motion in spin-orbit torque (SOT) based devices.
The focus will then shift from the diffusive transport regime to the coherent or ballistic transport regime. To give a better understanding of the used formalism, it is first discussed how the non-equilibrium Green's function (NEGF) formalism i.e. the Keldysh Green's function formalism accounts for open boundary conditions and how the formalism can provide numerical solutions to the Schrödinger equation in the chapters 4 and 5 before discussing a spin-polarized Hamiltonian that models MTJs in chapter 6. Finally, the NEGF calculations are coupled in a self-consistent manner to magnetization dynamics simulations in a computationally efficient way to investigate magnetization switching and back-hopping in STT-MRAM cells.

2 Free electrons in magnetic materials

Whenever an electron is located in a magnetic material, its spin-states are no longer degenerated and its spin has to be accounted for explicitly. Solutions to such a spin-dependent problem are called spin-polarized solutions. Since these properties are of high conceptual importance for the discussions in this work, it is illustrative to see how the spin-polarized probability density (i.e. the spin-accumulation) and the spin-polarized probability current (i.e. the spin-current) differ from their respective spin-independent counterparts.

2.1 The concept of spin-accumulation

Let us assume that we have a homogeneous magnetic material with electrons propagating through it. Due to the interaction with the localized magnetic moments, spin-up and spin-down electrons have a different wave vector, $\boldsymbol{k}^{\uparrow}$ and $\boldsymbol{k}^{\downarrow}$ respectively. We assume that this quantization is along the z-axis, meaning that $|\uparrow\rangle$ and $|\downarrow\rangle$ refer to the spin states parallel and antiparallel to the z-axis, but the particle's spin does not have to be collinear to that direction. Instead, it can be rotated in the direction (φ, θ) at $x = 0$ and if the electron can be described by plane waves, the corresponding time-independent wave function would be

$$|\psi(\boldsymbol{x})\rangle = e^{-i\varphi/2} \cos(\theta/2)\, e^{i\boldsymbol{k}^{\uparrow}\boldsymbol{x}} |\uparrow\rangle + e^{i\varphi/2} \sin(\theta/2)\, e^{i\boldsymbol{k}^{\downarrow}\boldsymbol{x}} |\downarrow\rangle . \tag{1}$$

The probability density of this particular wave function is equal to 1 everywhere, but what is the probability density of the individual spin-components? The answer to this question is the spin density or spin-accumulation [33].

$$\boldsymbol{s}(\boldsymbol{x}) = -\mu_B \langle \psi(\boldsymbol{x}) | \boldsymbol{\sigma} | \psi(\boldsymbol{x}) \rangle \tag{2}$$

This vectorial property is obtained with the help of the Pauli vector

$$\boldsymbol{\sigma} = \begin{bmatrix} \sigma_x \\ \sigma_y \\ \sigma_z \end{bmatrix} \tag{3}$$

with the individual Pauli matrices being

$$\sigma_x = \begin{bmatrix} 0 & 1 \\ 1 & 0 \end{bmatrix} \qquad \sigma_y = \begin{bmatrix} 0 & -i \\ i & 0 \end{bmatrix} \qquad \sigma_z = \begin{bmatrix} 1 & 0 \\ 0 & -1 \end{bmatrix} \tag{4}$$

such that the components of (2) are the average values

$$s_k(\boldsymbol{x}) = -\mu_B \langle \psi(\boldsymbol{x}) | \sigma_k | \psi(\boldsymbol{x}) \rangle. \tag{5}$$

Using the observable $-\mu_B \sigma_k$ instead of $\hbar/2\sigma_k$ means that the spin-accumulation is a measure of the local angular momentum in units of Am^{-1} instead of the local spin in units of Js. Plugging the exemplary wave function (1) into (2) yields the spin-accumulation

$$\boldsymbol{s}(\boldsymbol{x}) = -\mu_B \begin{bmatrix} \cos\left(\left[\boldsymbol{k}^{\downarrow} - \boldsymbol{k}^{\uparrow}\right] \cdot \boldsymbol{x} + \varphi\right) \sin(\theta) \\ \sin\left(\left[\boldsymbol{k}^{\downarrow} - \boldsymbol{k}^{\uparrow}\right] \cdot \boldsymbol{x} + \varphi\right) \sin(\theta) \\ \cos(\theta) \end{bmatrix} \tag{6}$$

and can be interpreted as the particles angular momentum being tilted out of the z-axis by θ and precessing around this axis. This appears reminiscent of how the angular momentum would precess around an external magnetic field, but the energy splitting of the conduction electrons is due to the exchange interaction with the localized spins.

The overall spin-accumulation won't be due to a single electronic state, however. In the context of spintronics, the total spin-accumulation is usually thought of as being the local magnetic moment from all electrons contributing to the current flow through the system. Thus, it is the sum of spin-densities of a number of electrons given by the density of states for some energy interval around the Fermi-level. Assuming that the conduction electrons do not interact with each other explicitly, each of them contributes to the total spin-accumulation according to (6).

Judging from this expression, it might seem that if the electrons are injected from a non-magnetic lead into the ferromagnet completely unpolarized i.e. if they all have a random spin-direction, the total spin accumulation will average out, but this is not the case. The reason for this are the different spin-up and spin-down reflection coefficients at the interface to the ferromagnetic material.
For the purpose of illustrating the situation, let's assume that all electrons travel perpendicular to the interface between the non-magnetic (NM) and the ferromagnetic (FM) region. Outside the ferromagnetic material, the spin states are degenerated and the wavenumber is spin-independent. An incoming electron with its spin directed along (φ, θ) can therefore be described by

$$|\psi_{\mathrm{NM}}(x)\rangle = R(\theta, \varphi) \cdot \begin{bmatrix} e^{ikx} + r^{\uparrow} e^{-ikx} \\ r^{\downarrow} e^{-ikx} \end{bmatrix} \tag{7}$$

with $r^{\uparrow}$ and $r^{\downarrow}$ being the part of the wave function reflected at the NM/FM interface into the spin-up and spin-down component and

$$R(\theta, \varphi) = \begin{bmatrix} e^{-i\varphi/2} \cos(\theta/2) & -e^{-i\varphi/2} \sin(\theta/2) \\ e^{i\varphi/2} \sin(\theta/2) & e^{i\varphi/2} \cos(\theta/2) \end{bmatrix} \tag{8}$$

being a unitary rotation matrix.

Staying with the assumption that the localized spins in the ferromagnet are directed in the positive z-direction, meaning that the material's magnetization points in the negative z-direction, the wave function within this region is

$$|\psi_{\mathrm{FM}}(x)\rangle = \begin{bmatrix} t^{\uparrow} e^{ik^{\uparrow}x} \\ t^{\downarrow} e^{ik^{\downarrow}x} \end{bmatrix}. \tag{9}$$

Matching the two wave functions (7) and (9) as well as their respective derivatives yields the spin-up and spin-down reflectivities

$$R^{\uparrow} = 1 - \frac{k^{\uparrow}|t^{\uparrow}|^2}{k} = 1 - \frac{2kk^{\uparrow}(1+\cos(\theta))}{(k+k^{\uparrow})^2} \tag{10}$$

$$R^{\downarrow} = 1 - \frac{k^{\downarrow}|t^{\downarrow}|^2}{k} = 1 - \frac{2kk^{\downarrow}(1-\cos(\theta))}{(k+k^{\downarrow})^2}. \tag{11}$$

The z-component of the spin-accumulation in the ferromagnetic region is

$$s_z = -2\mu_B k^2 \left[\frac{1+\cos(\theta)}{(k+k^{\uparrow})^2} + \frac{\cos(\theta)-1}{(k+k^{\downarrow})^2} \right] \tag{12}$$

and by looking at the special cases of an incoming electron being in the $|\uparrow\rangle$ or $|\downarrow\rangle$ state

$$\boldsymbol{s}\Big|_{\theta=0} = -\mu_B \left[0, 0, \frac{4k^2}{(k+k^{\uparrow})^2} \right] \tag{13}$$

$$\boldsymbol{s}\Big|_{\theta=\pi} = \mu_B \left[0, 0, \frac{4k^2}{(k+k^{\downarrow})^2} \right] \tag{14}$$

one can see that the spin-dependent reflection leads to an imbalance of spin-up and spin-down electrons within the ferromagnetic region, while other components vanish.

By injecting electrons that are already polarized along an axis different from the magnetization direction, one could also invoke non-zero components of the total spin-accumulation perpendicular to the magnetization direction. However, such a transversal component will decay rapidly in a process known as dephasing. The reason is that in (6), the velocity of the precession depends on the wavenumbers $k^{\uparrow}$ and $k^{\downarrow}$, which in turn depend on the energy. Since states from an energy interval around the Fermi-level contribute to the total spin-accumulation, the amplitude of the transversal component will decrease with the individual precessions losing phase the further away they are from the interface.

2.2 The concept of spin-current

The local density is not the only property that can be split into different spin components. We can do the same with the current. The spin-current is a 3×3 matrix and is defined as the real part of the expectation value of the spin-resolved velocity operator $-\mu_B \boldsymbol{\sigma} \otimes \hat{\boldsymbol{v}}$ [33].

$$\hat{Q}(\boldsymbol{x}) = -\mu_B \Re \left\{ \langle \psi(\boldsymbol{x}) | \boldsymbol{\sigma} \otimes \hat{\boldsymbol{v}} | \psi(\boldsymbol{x}) \rangle \right\} \tag{15}$$

The velocity operator $\hat{\boldsymbol{v}} = \hat{\boldsymbol{p}}/m_e$ in (15) is the momentum operator

$$\hat{\boldsymbol{p}} = -i\hbar\nabla \tag{16}$$

divided by the electron mass. The spin-current (15) is of course very similar to the probability current

$$\boldsymbol{j}(\boldsymbol{x}) = \frac{1}{2m} \Re \left\{ \psi(\boldsymbol{x}) \hat{\boldsymbol{p}} \psi(\boldsymbol{x}) \right\} \tag{17}$$

associated with the wave function ψ, which differs from the charge current only by a factor of $-e$.

$$\boldsymbol{j}_e = -e\boldsymbol{j} \tag{18}$$

But just as we went from a scalar property with the probability density to the vectorial spin-accumulation, we went from a vector to a matrix with the probability current to the spin-current. The definitions (2) and (15) are true for arbitrary wave functions, but (15) can be simplified if ψ is a plane wave. For example, the current of the spin's z-component would then be obtained in the following way:

$$Q_{z,j}(\boldsymbol{x}) = -\mu_B \Re \left\{ -\langle \psi(\boldsymbol{x}) | \sigma_z \frac{i\hbar}{m} \frac{\partial}{\partial x_j} | \psi(\boldsymbol{x}) \rangle \right\} \tag{19}$$

$$= -\mu_B \Re \left\{ \begin{bmatrix} \psi^{\uparrow *}(\boldsymbol{x}) \\ \psi^{\downarrow *}(\boldsymbol{x}) \end{bmatrix}^T \cdot \begin{bmatrix} 1 & 0 \\ 0 & -1 \end{bmatrix} \cdot \begin{bmatrix} v_j^{\uparrow} \psi^{\uparrow}(\boldsymbol{x}) \\ v_j^{\downarrow} \psi^{\downarrow}(\boldsymbol{x}) \end{bmatrix} \right\} \tag{20}$$

$$= -\mu_B \left(n^{\uparrow}(\boldsymbol{x}) v_j^{\uparrow} - n^{\downarrow}(\boldsymbol{x}) v_j^{\downarrow} \right) \tag{21}$$

$$= -\mu_B \left(j_j^{\uparrow}(\boldsymbol{x}) - j_j^{\downarrow}(\boldsymbol{x}) \right) \tag{22}$$

We could go one step further and introduce the concept of a polarization P that measures the imbalance of spins contributing to the current, such that

$$\boldsymbol{j}^{\uparrow} - \boldsymbol{j}^{\downarrow} = P\boldsymbol{j}. \tag{23}$$

Naturally, this requires the probability current direction to be the same as the direction of the spin-current, which is not always true. If the direction of the local

spin-accumulation is $\hat{\boldsymbol{s}}$ such that $\boldsymbol{s}(\boldsymbol{x}) = s(\boldsymbol{x})\hat{\boldsymbol{s}}(\boldsymbol{x})$, then the complete spin-current matrix is

$$\hat{Q} = -\mu_B P \hat{\boldsymbol{s}} \otimes \boldsymbol{j} = -\mu_B P \begin{bmatrix} \hat{s}_x j_x & \hat{s}_x j_y & \hat{s}_x j_z \\ \hat{s}_y j_x & \hat{s}_y j_y & \hat{s}_y j_z \\ \hat{s}_z j_x & \hat{s}_z j_y & \hat{s}_z j_z \end{bmatrix} \tag{24}$$

In this simplified form, it is especially easy to see that the columns of the spin-current matrix represent the spin flowing in the direction indicated by the column number while the rows of the matrix are the vectorial currents for a single spin component.

2.3 The spin-Hall effect

Again, (24) is only true if the flow of charge and spin is collinear, but there are effects of different origin [34, 35] that lead to a spin-current flowing in a different direction than the charge current. In fact, applying a current might even directly generate a spin-current perpendicular to the charge current. This can be the result of spin-orbit effects at the interface of non-magnetic metals and ferromagnetic material [36] or can be attributed to the bulk spin-Hall effect [37, 38] of some non-magnetic metals. Perpendicular spin-currents can originate in a mixture of these effects, but they can also be clearly dominated by one or the other [39, 40].

The spin-Hall effect (SHE) [41] together with its counterpart, the inverse spin-Hall effect (ISHE) [42] lead to the conversion of a charge current to a perpendicular spin-current and vice-versa, according to the phenomenological relation [43, 44]

$$\boldsymbol{j}_{\mathrm{SHE}} = -\frac{\mu_B}{e}\theta_{\mathrm{SHE}}\, \boldsymbol{j}_e \times \hat{\boldsymbol{s}} \tag{25}$$

with electrons of polarization $\hat{\boldsymbol{s}}$ contributing to a current along $\boldsymbol{j}_{\mathrm{SHE}}$. Equivalently, the spin-components can be handled explicitly by obtaining the full matrix form of the spin-current by utilizing the Levi-Cevita tensor ϵ_{ijk}

$$Q_{\mathrm{SHE},ij} = -\frac{\mu_B}{e}\epsilon_{ijk}\theta_{\mathrm{SHE}}\, \boldsymbol{j}_{e,k}, \tag{26}$$

such that the two expressions are connected by

$$\boldsymbol{j}_{\mathrm{SHE}} = Q_{\mathrm{SHE}}^{\mathrm{T}} \cdot \hat{\boldsymbol{s}}. \tag{27}$$

The dimensionless parameter θ_{SHE} in both expressions is the so-called spin-Hall angle. This system property measures the conversion ratio of the charge current into the transversal spin-current. Although one can differentiate a variety of effects

that can contribute to the spin-Hall current [45], the spin-Hall effect is fundamentally the result of spin-orbit coupling (SOC) [35, 44]. The effect is usually found to be significant in 5d metals [46] such as Pt, Ta, W and Hf [44].

The spin-Hall angle should be considered to be a system parameter rather than a material parameter since it strongly depends on the thickness of the material [47] but also on proper material parameters, most importantly the favorably small spin diffusion length λ_{sf} [46, 48]. Indeed, the measured values for a single material can vary greatly. For example, according to [48], the reported values for Pt lie between 0.01 and 0.20 with the spin diffusion length differing also by one order of magnitude. References [44, 46, 48] give an overview over reported values of θ_{SHE}, which are typically in the order of magnitude from 10^{-1} to 10^{-3}.

3 Micromagnetism

Due to the high degree of uncertainties and the overall size of modern spintronic devices, ab initio simulations in an atomistic fashion on the length scale of angstrom or below is often not desirable. Micromagnetism gives a framework to describe rather large devices on a micron scale. The basic idea is to assume that if the magnetic moment changes only very slightly from atomic site to atomic site, the magnetization can be viewed as a continuous function of the position.
Our discussion on the micromagnetic model will follow mainly the review article of Abert [49] and we will adopt the notation used in the referenced article throughout this work.

We have already discussed how the magnetization of a ferromagnetic material polarizes the angular momentum of the electrons flowing through it, but the magnetization state of the material might not be fixed. Especially in the context of sensor applications, one should think of the magnetization as a dynamic property instead. In this semi-classical theory, the dynamics of the magnetization are described by the Landau-Lifshitz-Gilbert (LLG) equation [50, 51].

$$\frac{\partial \boldsymbol{m}}{\partial t} = -\gamma \boldsymbol{m} \times \boldsymbol{H}^{\text{eff}} + \alpha \boldsymbol{m} \times \frac{\partial \boldsymbol{m}}{\partial t}. \tag{28}$$

In it, $\gamma = \mu_0 \gamma_e$ is the reduced gyromagnetic ratio and α is the Gilbert damping parameter. This equation models the dynamics of the local magnetization direction $\boldsymbol{m}$ under the assumption that the local magnetization $\boldsymbol{M}$ stays saturated such that

$$\boldsymbol{M} = M_s \boldsymbol{m} \tag{29}$$

with M_s being the saturation magnetization and $\boldsymbol{m}$ being a unit vector. Since the length of $\boldsymbol{M}$ is assumed to be constant, the velocity $\partial_t \boldsymbol{m}$ can be split into two components, just as they occur in the explicit form of (28).

$$\frac{\partial \boldsymbol{m}}{\partial t} = -\frac{\gamma}{1+\alpha^2} \boldsymbol{m} \times \boldsymbol{H}^{\text{eff}} - \frac{\alpha\gamma}{1+\alpha^2} \boldsymbol{m} \times \left(\boldsymbol{m} \times \boldsymbol{H}^{\text{eff}} \right) \tag{30}$$

The first component is directed along $-\boldsymbol{m} \times \boldsymbol{H}^{\text{eff}}$ and it lets the magnetization precess around the local effective field $\boldsymbol{H}^{\text{eff}}$. The second term along $-\boldsymbol{m} \times \left(\boldsymbol{m} \times \boldsymbol{H}^{\text{eff}} \right)$ is orthogonal to the first and tries to align the local magnetization direction with the effective field.

3.1 Purely magnetic effects

The effective field can vary locally and is the sum of all fields acting on the magnetization. Such fields can be external fields, but it is also possible to attribute

fields to every energy contributions [52]

$$\boldsymbol{H}^{\text{eff}} = -\frac{1}{\mu_0 M_s}\frac{\delta E}{\delta \boldsymbol{m}} \tag{31}$$

such that the components of the effective field are functional derivatives with respect to the magnetization components.

$$H_k^{\text{eff}}(\boldsymbol{x}) = -\frac{1}{\mu_0 M_s}\frac{\delta E\,[m]}{\delta m_k(x)}. \tag{32}$$

In the absence of an external field $\boldsymbol{H}^{\text{ext}}$, the magnetization of ferromagnetic materials aligns itself parallel or antiparallel with the uniaxial anisotropy axis $\boldsymbol{e}_u$.

$$\boldsymbol{H}^{\text{aniso}} = \frac{2K_u}{\mu_0 M_s}\boldsymbol{e}_u\,(\boldsymbol{e}_u \cdot \boldsymbol{m}) \tag{33}$$

The anisotropy energy

$$E^{\text{aniso}} = -K_u \int (\boldsymbol{e}_u \cdot \boldsymbol{m})^2\,\mathrm{d}\boldsymbol{x} \tag{34}$$

is a symmetric function of the angle between the magnetization and the anisotropy axis around $\pi/2$ with the minima $-VK_u$ of the function being located at $\boldsymbol{m} = \pm\boldsymbol{e}_u$.

If there was no anisotropy and in the absence of any other field, the magnetization of a material would not be random at every atomic site. Instead, the exchange energy tries to align neighboring spins parallel to each other. Therefore, the exchange energy gives justification for the continuous approach taken to magnetization in the micromagnetic model. Within the micromagnetic framework, the exchange field is given by

$$\boldsymbol{H}^{\text{ex}} = \frac{2}{\mu_0 M_s}\nabla \cdot (A\nabla \boldsymbol{m}) \tag{35}$$

with A being the exchange parameter. $\nabla\boldsymbol{m}$ is to be understood as the matrix-valued gradient of $\boldsymbol{m}$.

The demagnetization field or stray field is the magnetic field due to the magnetization. We are going to only motivate its derivation here, without following it through in every detail. The magnetic flux is the sum of the magnetization and the demagnetization field.

$$\boldsymbol{B} = \mu_0\left(\boldsymbol{H}^{\text{dem}} + \boldsymbol{M}\right) \tag{36}$$

Without any current flowing through the material, the Maxwell equations state that the divergence of the magnetic flux and the rotation of the demagnetization

field are both zero.

$$\nabla \cdot \boldsymbol{B} = 0 \tag{37}$$

$$\nabla \times \boldsymbol{H}^{\mathrm{dem}} = 0 \tag{38}$$

Due to the latter, the demagnetization field is a conservative field and can be written as the gradient of a potential function.

$$\boldsymbol{H}^{\mathrm{dem}} = -\nabla u \tag{39}$$

This can be plugged into the definition of the magnetic flux (36) and requiring (37) gives the Poisson equation

$$\Delta u = \nabla \cdot \boldsymbol{M} \tag{40}$$

to which the solution is well-known. The spatial integration required by the convolution of the Green's function with the source term, which results in a volume term and a boundary term [53]

$$u = -\frac{1}{4\pi}\left[\int_{\Omega} \frac{M_s \nabla' \cdot \boldsymbol{m}(\boldsymbol{x}')}{|\boldsymbol{x}-\boldsymbol{x}'|}\mathrm{d}\boldsymbol{x}' - \int_{\partial\Omega} \frac{M_s \boldsymbol{m}(\boldsymbol{x}') \cdot \boldsymbol{n}}{|\boldsymbol{x}-\boldsymbol{x}'|}\mathrm{d}\boldsymbol{s}'\right] \tag{41}$$

can be interpreted as the local effect of the field generated by all the magnetic material considered.

While the exchange field aims to keep the magnetization direction uniform, the demagnetization field favors antiparallel spins. The formation of magnetic domains and domain walls can be explained by simultaneously considering exchange and demagnetization field and by recognizing, that the exchange field is the dominant term only on short ranges [54].

Magnetizations of layers in magnetic stacks that are separated by a non-magnetic spacer layer might not only interact by the means of the demagnetization field. Instead, there can be a sort of exchange between the magnetizations on the interfaces to the spacer layer. This effect is called Ruderman-Kittel-Kasuya-Yosida (RKKY) interaction [55, 56] or interlayer-exchange coupling. Similar to the demagnetization field, it introduces a sort of non-locality to the LLG. If the interfaces of the two involved magnetic layers to the spacer layer are Γ_1 and Γ_2, then the energy of the interlayer exchange coupling is

$$E^{\mathrm{iex}} = -\int_{\Gamma_1 \cup \Gamma_2} A_{\mathrm{iex}} \boldsymbol{m}(x) \cdot \boldsymbol{m}\left(P\left\{\boldsymbol{x}\right\}\right) \mathrm{d}\boldsymbol{s} \tag{42}$$

with $P\{\boldsymbol{x}\}$ being a projection that yields the closest position on Γ_2 for every position on Γ_1 and vice versa. The value of the interlayer-exchange parameter A_{iex} was found to oscillates with the thickness of the spacer layer and can be either positive or negative.

3.2 Numerical micromagnetism

All micromagnetic simulations carried out in this work are performed with the python library magnum.fe [57] based on the finite elements method. The fundamentals of numerical micromagnetism are outlined in great detail in a review article by Abert [49] and we are not going to discuss them here. However, a point should be made about the discretization of meshes for micromagnetic simulations, whether they are finite differences or finite elements meshes. The micromagnetic assumption states that the magnetic moments localized at atomic sites change only slightly from one lattice site to a neighboring site and that we can therefore reasonably approximate the magnetization by a continuous vector function. If we now introduce a discretization again, we should take this assumption into consideration by requiring that the discretization length is shorter than the exchange length [58]. The exchange length determines the width of domain walls and is defined by

$$L_{\text{ex}} = \sqrt{\frac{A}{K_{\text{eff}}}} \tag{43}$$

with K_{eff} being the effective anisotropy constant, which, in addition to the crystalline anisotropy, also includes the shape anisotropy. Later, when we will couple coherent transport calculations with discretization lengths in the Angstrom scale to micromagnetic simulations, we will also refer back to the exchange length when averaging the magnetization.

3.3 Inclusion of spintronic effects

In chapter 2.1, where the concept of the spin-accumulation was introduced, we already argued how the local magnetization could act on the magnetic moments of conducting electrons. We found that the magnetization of a material polarizes incoming electrons by invoking an imbalance between spin-up and spin-down states and by dephasing any transversal components to the local magnetization axis. All these effects are due the magnetization or, more precisely, the d-electrons in a transition metal, acting on the conducting s-electrons. This interaction is bidirectional and the magnetic moments of the electrons traveling through the material consequently can act back on the magnetization. The rate of change of the local magnetization induced by the flow of angular momentum that is transported by the conduction electrons is the torque $\boldsymbol{T}$ that can be added to the LLG.

$$\frac{\partial \boldsymbol{m}}{\partial t} = -\gamma \boldsymbol{m} \times \boldsymbol{H}^{\text{eff}} + \alpha \boldsymbol{m} \times \frac{\partial \boldsymbol{m}}{\partial t} + \boldsymbol{T} \tag{44}$$

To avoid confusion, we will denote this form of the LLG as the *modified* LLG. Since the LLG assumes that $\boldsymbol{m}$ is a unit vector, the torque can be split into two

terms with the same symmetry as seen in the explicit form of the LLG (30). These two contributions are the fieldlike torque $\boldsymbol{T}_{\mathrm{fl}}$ and the dampinglike torque $\boldsymbol{T}_{\mathrm{dl}}$ [59].

$$\boldsymbol{T} = \boldsymbol{T}_{\mathrm{fl}} + \boldsymbol{T}_{\mathrm{dl}} \tag{45}$$

$$\boldsymbol{T}_{\mathrm{fl}} = \tau_{\mathrm{fl}}\, \boldsymbol{m} \times \boldsymbol{p} \tag{46}$$

$$\boldsymbol{T}_{\mathrm{dl}} = \tau_{\mathrm{dl}}\, \boldsymbol{m} \times (\boldsymbol{m} \times \boldsymbol{p}) \tag{47}$$

The dampinglike term is also known as the Slonczewski torque term. In (46) and (47), the polarization vector $\boldsymbol{p}$ can have different meanings, depending on the system under investigation but can be viewed as the intended polarization direction of the electron spin before entering the material in which the torque acts on the magnetization.

Two prominent designs that utilize spin-torque to alter the magnetization direction of a ferromagnetic material are depicted in figure 1. Figure 1(a) depicts a spin-transfer torque (STT) driven device layout. It consists of two ferromagnetic layers, FM1 and FM2, that are connected by a spacer layer. The basic idea is that one of these two ferromagnetic layers is pinned or fixed by a large anisotropy or by coupling it via the interlayer-exchange interaction to additional magnetic layers. Meanwhile, the second ferromagnetic layer is soft-magnetic and its magnetization is easily manipulated by the torque it is subjected to. Electrons that enter the device from the left are polarized by the first ferromagnetic layer and exert a torque on the second one, if its magnetization is not collinear to the one of FM1. If we would use the modified LLG to determine the magnetization dynamics of the second layer, the polarization vector is the magnetization of the first layer and vice versa.

$$\boldsymbol{p}_{\mathrm{STT}} = \begin{cases} \boldsymbol{m}_{\mathrm{FM2}} & \text{for torque acting on } \boldsymbol{m}_{\mathrm{FM1}} \\ \boldsymbol{m}_{\mathrm{FM1}} & \text{for torque acting on } \boldsymbol{m}_{\mathrm{FM2}} \end{cases} \tag{48}$$

Due to the spin-dependent reflectivities at the interfaces to ferromagnetic materials, the torque acts not solely on the right layer if the electrons enter from the left, however. Instead, the reflected electrons from the spacer/FM2-interface exert a torque back on FM1. If the two layers are in an antiparallel configuration, this reflected magnetic moments would stabilize the magnetization of FM1 while in a parallel configuration, they would act as a destabilizing force on $\boldsymbol{m}_{\mathrm{FM1}}$ and would try to turn it in the opposite direction. For that reason, it is possible to switch the magnetization in both directions by changing the polarity of the applied voltage. For a conducting spacer layer, the overall resistivity of the spin-valve structure depicted in figure 1(a) is governed by the GMR effect. The change of the magnetic configuration of the stack is therefore detectable in the resistance felt by the writing current.

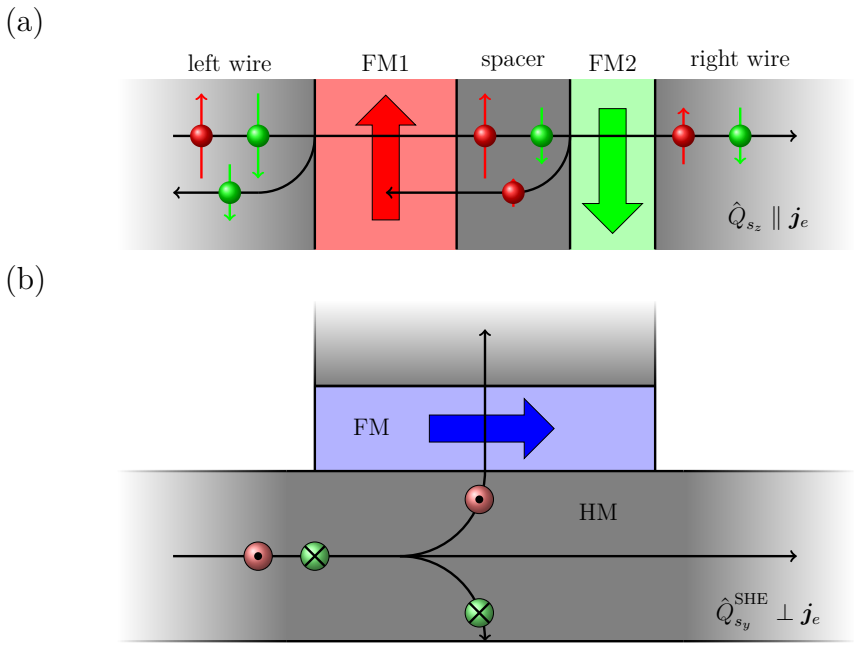

Figure 1: Comparison of STT and SOT device principles. (a) In STT-driven devices, angular momentum is transferred from one ferromagnetic layer to the other. Reversing the current direction allows for bi-directional switching since the spin accumulation due to previous polarization by the opposing layer and due to spin-dependent reflection from the opposing FM/spacer interface have different sign. (b) SOT devices use a spin-current generated by the spin-Hall effect in a heavy metal (HM) layer. This spin-current flows transversal to the charge current and injects spins into a FM layer on top of the HM layer. Changing the charge current polarity also changes the direction of the torque acting on the FM layer.

Instead of a second magnetic layer that acts as a polarizer, the spin-orbit torque (SOT) driven device shown in figure 1(b) utilizes the spin-Hall effect to obtain a spin-current to exert torque on a ferromagnetic layer. In this device principle, the free layer is stacked on top of a heavy metal layer that has a large enough spin-Hall angle so that the spin-current injected from it into the ferromagnetic layer can influence the magnetization of the latter. If the interface normal of the HM/FM-interface is along $\hat{\boldsymbol{n}}$, then the polarization vector of the SOT is

$$\boldsymbol{p}_{\mathrm{SOT}} = \hat{\boldsymbol{n}} \times \hat{\boldsymbol{v}} \tag{49}$$

with $\hat{\boldsymbol{v}}$ being the direction of the probability current.

So far, we have avoided to invoke the spin-accumulation or spin-current directly.

This is because our previous discussion of them assumed that we know the wave functions of the conduction electrons, but in a micromagnetic treatment, this is very unlikely. Scattering at crystallographic defects would be nearly impossible to include into wave function calculations on a micron scale but should be expected to dominate all electronic and spintronic properties. Within this diffusive regime, both the STT and the SOT scale linearly with the applied current and the torque coefficients can therefore be related by

$$\tau_{\mathrm{fl}} = \eta_{\mathrm{fl}}(\theta)\frac{j_e\gamma\hbar}{2e\mu_0 M_s t} \tag{50}$$

$$\tau_{\mathrm{dl}} = \eta_{\mathrm{dl}}(\theta)\frac{j_e\gamma\hbar}{2e\mu_0 M_s t} \tag{51}$$

to the dimensionless parameters η_{fl} and η_{dl}, with t being the thickness of the magnetic layer on which the torque acts. In the case of STT, the values of the torque efficiencies η_{fl} and η_{dl} depend on the concrete material of both magnetic layers and the angle θ between the two magnetizations. According to reference [60], η_{fl} and η_{dl} are a function of θ of the form

$$\eta_{\mathrm{STT}}(\theta) = \frac{q^+}{A + B\cos(\theta)} + \frac{q^-}{A - B\cos(\theta)} \tag{52}$$

so that the torque $\boldsymbol{T}$ including both the fieldlike and the dampinglike contribution can be modeled by eight additional parameters.

The SOT has no angular dependence but constant values of η_{fl} and η_{dl}. Referring back to our discussion of the spin-Hall effect in chapter 2.3, one might hope that the torque efficiencies η_{fl} and η_{dl} are true material parameters. In practice, one can extract the values of these parameters e.g. from second harmonic measurements for a specific system [61–63]. But as we have already discussed, a variety of effects that can also originate from the specific NM/FM-interface can contribute to the spin current that is injected in the FM layer. Reference [35] contains an extensive table of values for η_{fl} and η_{dl}, collected from a wide variety of measurements of SOT structures.

3.4 The spin-drift diffusion model

When we introduced the spin-accumulation in chapter 2.1, we defined it as the magnetic moment accumulating locally due to the current flow. In the context of micromagnetism, we might not be able to compute the spin-accumulation from the Schrödinger equation, but assuming a diffusive transport regime, we can argue

that it should be possible to obtain it from a drift-diffusion equation on the micron length scale. According to Zhang et al. in reference [29]

$$\frac{\partial \boldsymbol{s}}{\partial t} = -\nabla \cdot \hat{Q} - \frac{\boldsymbol{s}}{\tau_{\mathrm{sf}}} - J\frac{\boldsymbol{s} \times \boldsymbol{m}}{\hbar} \tag{53}$$

describes the dynamics of the spin accumulation $\boldsymbol{s}$. It is reasonable to assume that the spin-accumulation relaxes way faster than the magnetization and so it is usually sufficient to consider the static case

$$\nabla \cdot \hat{Q} = -\frac{\boldsymbol{s}}{\tau_{\mathrm{sf}}} - J\frac{\boldsymbol{s} \times \boldsymbol{m}}{\hbar} \tag{54}$$

with the component-wise divergence

$$\left(\nabla \cdot \hat{Q}\right)_i = \sum_j \frac{Q_{ij}}{\partial x_j}. \tag{55}$$

The spin-flip scattering time τ_{sf} and the spin-flip length λ_{sf} determine the diffusion constant related to the spin-accumulation.

$$D_0 = \frac{\lambda_{\mathrm{sf}}^2}{2\tau_{\mathrm{sf}}} \tag{56}$$

The spin-current in (54) depends not only on the change in spin-accumulation, but also on the gradient of the potential u.

$$\hat{Q} = 2C_0 P \frac{\mu_B}{e} \boldsymbol{m} \otimes \nabla u - 2D_0 \left(\nabla \otimes \boldsymbol{s}\right)^T. \tag{57}$$

It is instructive to compare the first term of (57), which is the polarization of the magnetic moments by the local magnetization, to the spin-current (24) obtained for a simple plain wave. The second term of (57) frames the spin-accumulation as a sort of potential for the spin-current, similar to the potential u for the charge current. The latter is defined by

$$\boldsymbol{j}_e = -2C_0 \nabla u + 2D_0 P' \frac{e}{\mu_B} \left(\nabla \otimes \boldsymbol{s}\right) \cdot \boldsymbol{m}. \tag{58}$$

The diffusion coefficient C_0 appearing in (58) is related to the conductivity by

$$\sigma = 2C_0. \tag{59}$$

Plugging (57) in (54) and (58) into the continuity equation

$$\nabla \cdot \boldsymbol{j}_e = 0 \tag{60}$$

yields a set of coupled equations that can be solved self-consistently with the LLG. This is called the spin-drift diffusion (SDD) model.

When modeling a spintronic device, one usually wants a charge current only to enter at interfaces of the device that are designated as contacts. At all other boundaries, no current, whether it is charge-current or spin-current, should be allowed to enter or exit the device. This can be achieved by setting

$$\hat{\boldsymbol{n}} \cdot \boldsymbol{j}_e = 0 \qquad \text{(at boundaries that are not a contact)} \tag{61}$$

whilst setting a chosen value of u as a Dirichlet boundary condition or alternatively for the current $\hat{\boldsymbol{n}} \cdot \boldsymbol{j}$ at boundaries acting as a contact. Setting a value for the current inflow or outflow is only equivalent to a Neumann boundary condition at boundaries of non-magnetic materials. For the same reason, setting (61) does not prevent a spin-current to flow out of magnetic boundaries and so additonally

$$\hat{Q} \cdot \hat{\boldsymbol{n}} = (0,0,0) \qquad \text{(all boundaries)} \tag{62}$$

should be set at all boundaries. This is fulfilled only if $\hat{\boldsymbol{n}} \cdot \nabla u = 0$ as well as $(\nabla \otimes \boldsymbol{s})^T \cdot \hat{\boldsymbol{n}} = (0,0,0)$ hold true. Note that this boundary condition, whilst being practical, requires the model of the device to include non-magnetic leads longer than λ_{sf} to all contacts to prevent reflections of the spin-accumulation from them.

The SDD model can be extended to include the spin-Hall effect. This extension was introduced in reference [64] and when it is included, the new currents $\boldsymbol{j}_e'$ and $\hat{Q}'$ defined by

$$j'_{e,i} = j_{e,i} + \frac{e}{\mu_B}\theta_{\mathrm{SHE}}\,\epsilon_{ijk}\hat{Q}_{jk} \tag{63}$$

$$\hat{Q}'_{ij} = \hat{Q}_{ij} + \frac{\mu_B}{e}\theta_{\mathrm{SHE}}\,\epsilon_{ijk}j_{e,k} \tag{64}$$

are considered to be the actual charge and spin-current and thus the boundary conditions as well as the source equations (54) and (60) should be reformulated with respect to them instead of the original currents.

3.5 Torque calculated from the SDD model

The torque due to the spin-accumulation calculated from the SDD model is

$$\boldsymbol{T} = -\frac{J}{\hbar M_s}\boldsymbol{m} \times \boldsymbol{s}. \tag{65}$$

Starting from the modified LLG (44), it is straight forward to identify a field with this torque.

$$\boldsymbol{H}^{\mathrm{s}} = \frac{J}{\hbar\gamma M_s}\boldsymbol{s} \tag{66}$$

One could do the same for the torque written in terms of the polarization vector (46) and (47), which results in the field

$$\boldsymbol{H}^{\mathrm{T}} = -\frac{1}{\gamma}\left(\tau_{\mathrm{fl}}\,\boldsymbol{p} + \tau_{\mathrm{dl}}\,\boldsymbol{m}\times\boldsymbol{p}\right). \tag{67}$$

Note how the fieldlike torque actually does behave like a field in the direction of $\boldsymbol{p}$ without any dependence on $\boldsymbol{m}$, giving this torque term its name. Inspecting the LLG in its explicit form (30) reveals that components of the effective field collinear to $\boldsymbol{m}$ cannot influence the dynamics. Consequently, one could project the field due to the spin-accumulation (66) on any two linearly independent basis vectors perpendicular to $\boldsymbol{m}$ and omit any component parallel to $\boldsymbol{m}$. Of course, this basis would be itself dynamic since it would change with a changing magnetization. For problems in which there is a meaningful polarization vector $\boldsymbol{p}$, comparing equation (67) to (65) and (66) does already give an adequate basis. Keeping in mind that $\boldsymbol{m}\times\boldsymbol{p} = -\boldsymbol{m}\times(\boldsymbol{m}\times(\boldsymbol{m}\times\boldsymbol{p}))$, the effective spin accumulation

$$\boldsymbol{s}^{\mathrm{eff}} = -s_{\mathrm{fl}}\boldsymbol{m}\times(\boldsymbol{m}\times\boldsymbol{p}) + s_{\mathrm{dl}}\boldsymbol{m}\times\boldsymbol{p} \tag{68}$$

with

$$s_{\mathrm{fl}} = \frac{\boldsymbol{s}\cdot\boldsymbol{b}_{\mathrm{fl}}}{\boldsymbol{b}_{\mathrm{fl}}\cdot\boldsymbol{b}_{\mathrm{fl}}} \tag{69}$$

$$s_{\mathrm{dl}} = \frac{\boldsymbol{s}\cdot\boldsymbol{b}_{\mathrm{dl}}}{\boldsymbol{b}_{\mathrm{dl}}\cdot\boldsymbol{b}_{\mathrm{dl}}} \tag{70}$$

$$\boldsymbol{b}_{\mathrm{fl}} = -\boldsymbol{m}\times(\boldsymbol{m}\times\boldsymbol{p}) \tag{71}$$

$$\boldsymbol{b}_{\mathrm{dl}} = \boldsymbol{m}\times\boldsymbol{p} \tag{72}$$

does result in exactly the same magnetization dynamics obtained from the LLG as the original spin-accumulation. This is since the torque of this effective spin-accumulation

$$\boldsymbol{T} = -\frac{J}{\hbar M_s}\left(s_{\mathrm{fl}}\,\boldsymbol{m}\times\boldsymbol{p} + s_{\mathrm{dl}}\,\boldsymbol{m}\times(\boldsymbol{m}\times\boldsymbol{p})\right) \tag{73}$$

is the same as the torque given by (65). Moreover, it is easy to see that the torque coefficients are

$$\tau_{\mathrm{fl}} = -\frac{Js_{\mathrm{fl}}}{\hbar M_s} \tag{74}$$

$$\tau_{\mathrm{dl}} = -\frac{Js_{\mathrm{dl}}}{\hbar M_s} \tag{75}$$

By looking just at (67) and (66), one might be easily fooled into thinking that $\boldsymbol{p}$ and $\boldsymbol{m}\times\boldsymbol{p}$ would be an adequate base too, but since $\boldsymbol{p}$ is not perpendicular to $\boldsymbol{m}$, this is not true.

In chapter 3.3, the torque for the SOT device structure was assumed to be characterized by constant values for the torque efficiency parameters η_{fl} and η_{dl}. For the STT device structure, these parameters were instead assumed to behave according to (52). In fact, both of these descriptions are consistent with the torques calculated from the spin-drift diffusion model for the respective device structures. This can easily be seen by computing the components (69) and (70) of the spin-accumulation obtained from the SDD model. Exemplary results are shown in figure 2(a) and (b) for STT and SOT, respectively.

The STT stack consists of two ferromagnetic layers FM1 and FM2, connected by a non-magnetic spacer layer and contacted by two non-magnetic leads. The first ferromagnetic layer is assumed to be the reference layer and its magnetization is the direction of the polarization vector. Its length is 2.8 nm and its saturation magnetization is $\mu_0 M_{s,\mathrm{FM1}} = 1.25$ T. The length of the free layer is $t = 1.2$ nm and its saturation magnetization is $\mu_0 M_{s,\mathrm{FM2}} = 1.25$ T. Besides the spin-flip scattering time, which is $\tau_{\mathrm{sf,FM1}} = 3 \cdot 10^{-14}$ s in the reference layer and $\tau_{\mathrm{sf,FM2}} = 5 \cdot 10^{-14}$ s in the free layer, both materials, share the same SDD parameters. These are $C_{0,\mathrm{FM}} = 1.2 \cdot 10^6$ A/Vm, $D_{0,\mathrm{FM}} = 1 \cdot 10^{-3}$ m^2/s, $J = 0.2$ eV, $P = 0.9$ and $P' = 0.8$. The spacer layer of 1 nm length is modeled by the same set of parameters as the leads, namely $C_0 = 6 \cdot 10^6$ A/Vm, $D_0 = 5 \cdot 10^{-3}$ m^2/s and $\tau_{\mathrm{sf}} = 1 \cdot 10^{-14}$ s. Extracting the torque efficiencies from the spin-accumulation in the free layer and fitting (52) towards the obtained data yields the fit parameters $q_{\mathrm{fl}}^{+} = -0.192$, $q_{\mathrm{fl}}^{-} = -0.0576$, $A_{\mathrm{fl}} = 1.14$ and $B_{\mathrm{fl}} = 0.315$ for the fieldlike torque and $q_{\mathrm{dl}}^{+} = -0.674$, $q_{\mathrm{dl}}^{-} = -0.130$, $A_{\mathrm{dl}} = 6.48$ and $B_{\mathrm{dl}} = 2.32$ for the dampinglike torque.

Meanwhile, the torques calculated from the SDD model for the SOT structure do correspond to constant values of η_{fl} and η_{dl}. This is shown in figure 2(b). The parameters that are used to model the magnetic layer are $\mu_0 M_{s,\mathrm{FM1}} = 1.25$ T, $C_{0,\mathrm{FM}} = 1.2 \cdot 10^6$ A/Vm, $D_{0,\mathrm{FM}} = 1 \cdot 10^{-3}$ m^2/s, $\tau_{\mathrm{sf,FM1}} = 5 \cdot 10^{-14}$ s, $J = 0.9$ eV, $P = 0.9$ and $P' = 0.8$ with the layer thickness being $t = 2.8$ nm. The heavy metal layer which generates the transversal spin-current due to the spin-Hall effect is characterized by the parameters $C_0 = 6 \cdot 10^6$ A/Vm, $D_0 = 5 \cdot 10^{-3}$ m^2/s, the spin-Hall angle $\theta_{\mathrm{SHE}} = 0.3$ and a spin-flip scattering length of $\lambda_{\mathrm{sf}} = 3.5$ nm. The thickness of the heavy metal layer is 4 nm and the lateral dimensions of the stack are 50×50 nm^2. The remaining domains are two non-magnetic leads and a capping layer on top of the structure with the same parameters as for the leads of the STT structure.

One might initially wonder how the dampinglike torque arises. It might seem reasonable to assume that no matter the device, the incoming spins of polarization $\boldsymbol{p}$ should act just like a field and thus result only in the fieldlike torque term. But this assumption ignores how the magnetization and the spin-accumulation

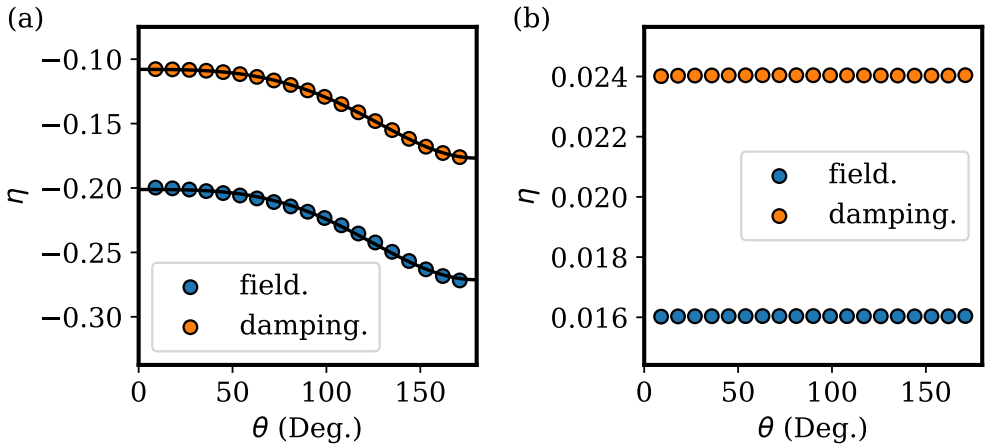

Figure 2: Dependence of the fieldlike and dampinglike torque efficiencies η_{fl} and η_{dl} on the angle θ between $\boldsymbol{m}$ and $\boldsymbol{p}$ for (a) STT with solid lines indicating fits of the model (52) and (b) SOT. The data points are obtained from the spin-drift diffusion model.

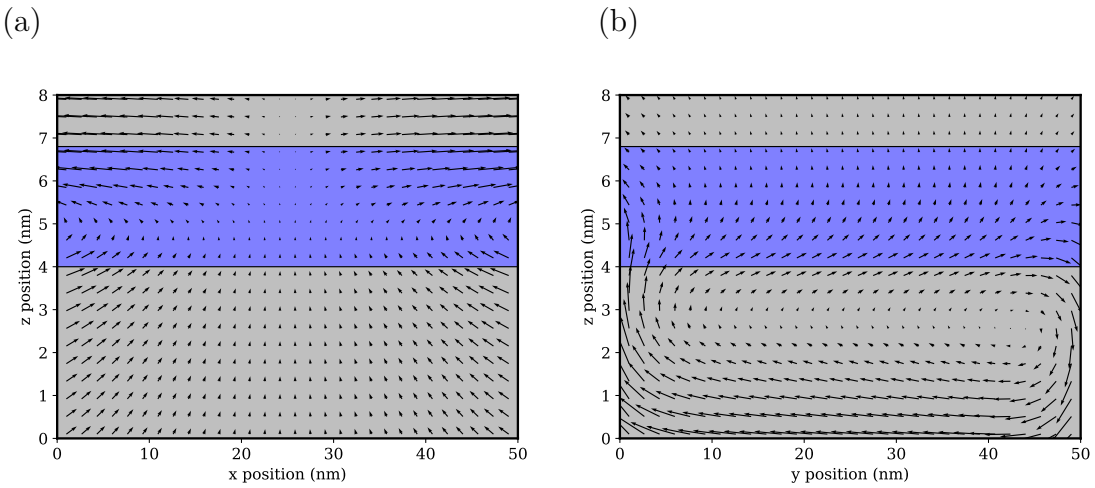

Figure 3: Slices through an SOT device. (a) is along the xz-plane and (b) is along the yz-plane. The charge current flows along the x-direction. The blue area indicates the ferromagnetic layer with $\boldsymbol{m} = \hat{\boldsymbol{x}}$. The solid black arrows indicate the local direction of the spin-accumulation. The curling of the spins beneath the FM layer in (b) is the result of the spin-Hall effect. Due to the coupling term with the local magnetization in (54), the spins entering the FM layer are tilted into the z-direction and give rise to the dampinglike torque.

interact. Figure 3 shows two vertical slices through the SOT device in its $\boldsymbol{m} \parallel \hat{\boldsymbol{x}}$-configuration, one in the xz-plane and one in the yz-plane, with small arrows indicating the direction of the local spin-accumulation. The second one i.e. figure 3(b) is the more meaningful one with the yz-plane being perpendicular to the current direction, which is along $\hat{\boldsymbol{x}}$. Below $z = 4$ nm, which is inside the heavy metal layer, the spin-Hall effect is easily observable. In the ferromagnetic region, marked by a blue background color, the spin-accumulation is tilted out of the xy-plane by the interaction with the local magnetization, giving rise to the dampinglike torque. To follow this argument, remember that $\boldsymbol{m} \times \boldsymbol{p} \parallel \hat{\boldsymbol{z}}$ holds true in the depicted configuration.

3.6 Damping Modulation

Adding the field associated with the torque (67) into the explicit form of the LLG (30) and reordering the terms according to their symmetry yields the explicit form of the modified LLG.

$$\begin{aligned}\frac{\partial \boldsymbol{m}}{\partial t} =& -\frac{\gamma}{1+\alpha^2}\boldsymbol{m} \times \left[\boldsymbol{H}^{\text{eff}} + \frac{1}{\gamma}\left(\alpha\tau_{\text{dl}} - \tau_{\text{fl}}\right)\boldsymbol{p}\right] \\ & -\frac{\alpha\gamma}{1+\alpha^2}\boldsymbol{m} \times \left[\boldsymbol{m} \times \left[\boldsymbol{H}^{\text{eff}} - \frac{1}{\gamma}\left(\frac{1}{\alpha}\tau_{\text{dl}} + \tau_{\text{fl}}\right)\boldsymbol{p}\right]\right] \end{aligned} \tag{76}$$

This form of the modified LLG has a noteworthy peculiarity to it: the axis around which the magnetization precesses and the axis towards its damping motion is directed are not the same. To investigate how the two torque terms influence the dynamics of the magnetization, we are defining two new terms.

$$\boldsymbol{L}_{\perp} = -\frac{\alpha\tau_{\text{dl}} - \tau_{\text{fl}}}{1+\alpha^2}\boldsymbol{m} \times \boldsymbol{p} \tag{77}$$

$$\boldsymbol{L}_{\parallel} = \frac{\tau_{\text{dl}} + \alpha\tau_{\text{fl}}}{1+\alpha^2}\boldsymbol{m} \times (\boldsymbol{m} \times \boldsymbol{p}) \tag{78}$$

With them, the explicit LLG reads

$$\begin{aligned}\frac{\partial \boldsymbol{m}}{\partial t} =& -\frac{\gamma}{1+\alpha^2}\boldsymbol{m} \times \boldsymbol{H}^{\text{eff}} + \boldsymbol{L}_{\perp} \\ & -\frac{\alpha\gamma}{1+\alpha^2}\boldsymbol{m} \times \left[\boldsymbol{m} \times \boldsymbol{H}^{\text{eff}}\right] + \boldsymbol{L}_{\parallel}. \end{aligned} \tag{79}$$

These terms appear to be similar to the fieldlike and dampinglike torque terms, given that they are also directed along $\boldsymbol{m} \times \boldsymbol{p}$ and $\boldsymbol{m} \times (\boldsymbol{m} \times \boldsymbol{p})$. However, there is an important difference: The torque terms (46) and (47) are added to the implicit form of the LLG. That way, the fieldlike term acts just like an external field, as

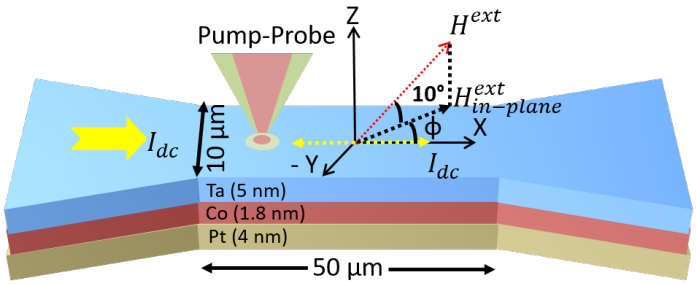

Figure 4: Layout of the experiment conducted in reference [65]. A current in x-direction exerts a spin-orbit torque on the magnetization of the Co layer via the spin-Hall effect in Pt and Ta. The magnetization is excited by a pump laser and its consequent relaxation is monitored by TR-MOKE measurements to determine the dependence of the effective damping on the current and the direction of an applied external field $\boldsymbol{H}^{\text{ext}}$.
Reprinted figure with permission from S. Saha et al., Phys. Rev. B, **101**, p. 224401, 2020, https://doi.org/10.1103/PhysRevB.101.224401. Copyright (2022) by the American Physical Society.

pointed out before, whilst the torque terms are orthogonal to each other. The in-plane and out-of-plane velocities $\boldsymbol{L}_{\perp}$ and $\boldsymbol{L}_{\parallel}$ are however contributions to the explicit form of the LLG and are in consequence the contributions to the actual motion of the magnetization in the plane of $\boldsymbol{m}$ and $\boldsymbol{p}$ and perpendicular to this plane. Only in the special case of vanishing α, $\boldsymbol{L}_{\perp}$ and $\boldsymbol{L}_{\parallel}$ would reduce to the fieldlike torque and the dampinglike torque, respectively.

We will now turn our attention to an experiment performed by Saha et al. in reference [65] to which a numerical comparison was contributed as part of this work. The idea of this experiment is summarized in figure 4 and is as follows: A current is applied to a Pt(4)/Co(1.8)/Ta(5) stack (the values in the brackets indicate the layer thickness), generating a spin-current due to the spin-Hall effect that exerts a torque on the magnetization of the Co layer. An external field $\boldsymbol{H}^{\text{ext}}$ of 150 mT is applied to the structure. This field is tilted by 10° out of the device plane i.e. the xy-plane and can be rotated around the out-of-plane axis with the angle ϕ between the x-axis and the in-plane component of the field being the measure for this rotation. A pulse laser of $\lambda = 515$ nm with a pulse width of ≈ 50 fs is used to excite the system and a probe laser of $\lambda = 1030$ nm and with approximately the same pulse width as the one of the pulse laser is used to measure the time-resolved magneto-optical Kerr effect (TR-MOKE) [66]. This technique allows to measure the dynamics of the magnetization's out-of-plane component,

which in turn allows to determine the effective damping constant of the system. This is done by subtracting two exponential functions with offset from the data and before fitting [67, 68]

$$\tilde{m}_z(t) = M_0 e^{2\pi\alpha_{\text{eff}} f t} \sin\left(2\pi f t + \varphi\right) \tag{80}$$

towards it. This means that the dynamics of the out-of-plane component should end up in a regime in which it can be described by

$$m_z(t) = \tilde{m}_z(t) + \frac{1}{2}\left(M_1 e^{-\lambda_1 t} + M_2 e^{\lambda_2 t}\right) + d \tag{81}$$

with f being the frequency of the oscillation, and M_0, M_1, M_2, λ_1, λ_2, φ and d being additional fit parameters to the effective damping parameter α_{eff}. The latter is expected to depend on the angle of the applied field ϕ and the applied current.

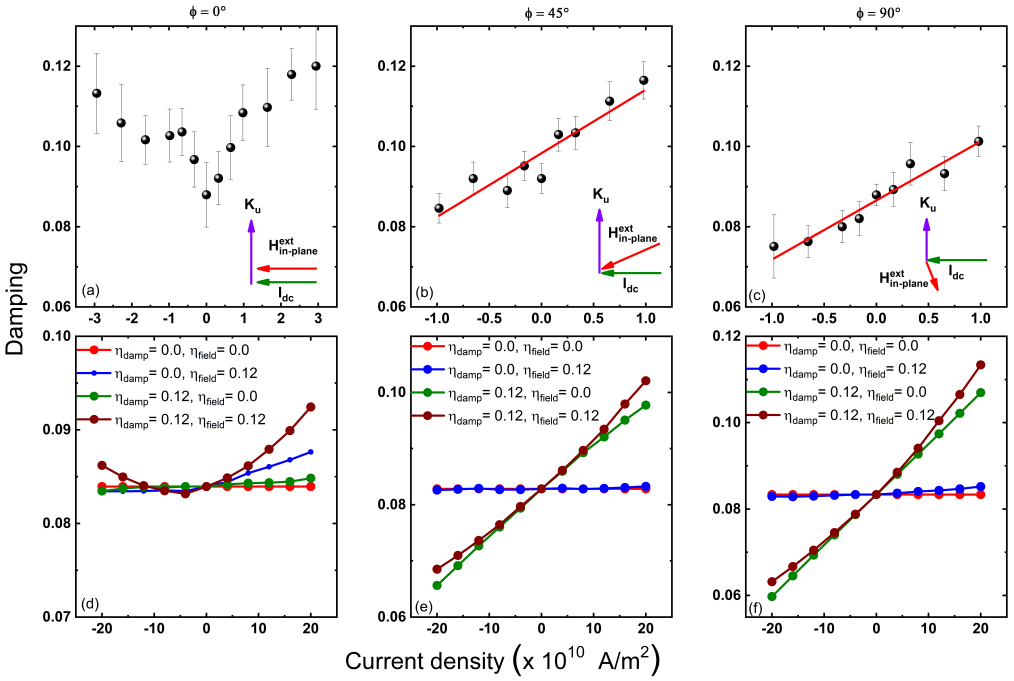

Figure 5: The dependence of the damping parameter on current density, determined from (a-c) TR-MOKE and (d-f) simulation for $\phi = 0°$, 45° and 90° are shown. The schematic of the current direction (I_{dc}) and in plane component of external magnetic field ($H^{\text{ext}}_{\text{in-plane}}$) are shown in inset of (a-c). In (d-f) the dependence of damping parameter on the current density for different combinations of η_{damp} and η_{field} are shown.
Reprinted figure with permission from S. Saha et al., Phys. Rev. B, **101**, p. 224401, 2020, https://doi.org/10.1103/PhysRevB.101.224401. Copyright (2022) by the American Physical Society.

To interpret the experimental outcome, it is helpful to reproduce the measurement computationally by solving the modified LLG (44). It is not necessary to simulate the whole device to get a good understanding of the damping modulation and simulating only a volume of $1 \times 1 \times 1.8$ nm^3 is sufficient. With its dimensions smaller than the exchange length, the description is basically reduced to a macrospin model. The parameters used to model the magnetic material are $M_s = 9.35 \cdot 10^5$ A/m, $K_u = 1.61 \cdot 10^5$ J/m^3 and $\alpha = 0.082$, all in accordance with experimental findings. M_s and K_u were determined from the device's in-plane and out-of-plane hysteresis and the unmodified damping parameter was measured as described above with no current applied. The value of the dampinglike torque efficiency of $\eta_{\mathrm{dl}} = 0.12$ was obtained from reference [47]. A comparison of the experimental and computational results is shown in figure 5 with good qualitative agreement between them. For $\phi = 45°$ and $\phi = 90°$, a linear dependence of the damping on the current is observed. For $\phi = 0°$, the dependence is highly nonlinear, however, with the modulation being quadratic in the case of both torques acting concurrently in the simulations.

To understand this, we will divert a bit and consider the magnetization dynamics in a simplified system that has no external field but only an uniaxial anisotropy field. We are going to consider two cases. In the first case, the anisotropy is directed in the positive y-direction, antiparallel to the direction of $\boldsymbol{p}$. A magnetization that is tilted out of its equilibrium position will precess around the y-axis and judging from the explicit form of the modified LLG (76), it is immediately clear that only (78) can influence the damping motion with (77) only influencing the rotational velocity. Even for η_{fl} and η_{dl} of similar size the damping motion would be dominated by the dampinglike torque with the fieldlike contribution being smaller by a factor of the Gilbert damping α. The dampinglike torque for this system is illustrated in figure 6(a).

The second case we are going to investigate is that of the anisotropy axis being in positive z-direction and therefore perpendicular to $\boldsymbol{p}$. In this case, the situation is a bit more complicated. We are still asking which torques can contribute the damping motion i.e. which can add a non-vanishing component along

$$\hat{\boldsymbol{v}} = \boldsymbol{v}/|\boldsymbol{v}| \tag{82}$$

$$\boldsymbol{v} = -\boldsymbol{m} \times (\boldsymbol{m} \times \hat{\boldsymbol{z}}) \tag{83}$$

As a measure, one could determine the time-integral of the projections of

$$\boldsymbol{L}_{\perp} = \frac{\alpha\tau_{\mathrm{dl}} - \tau_{\mathrm{fl}}}{1+\alpha^2} \left(-m_z,\, 0,\, m_x\right) \tag{84}$$

$$\boldsymbol{L}_{\parallel} = -\frac{\tau_{\mathrm{dl}} + \alpha\tau_{\mathrm{fl}}}{1+\alpha^2} \left(m_x m_y,\, -m_x^2 - m_z^2,\, m_y m_z\right) \tag{85}$$

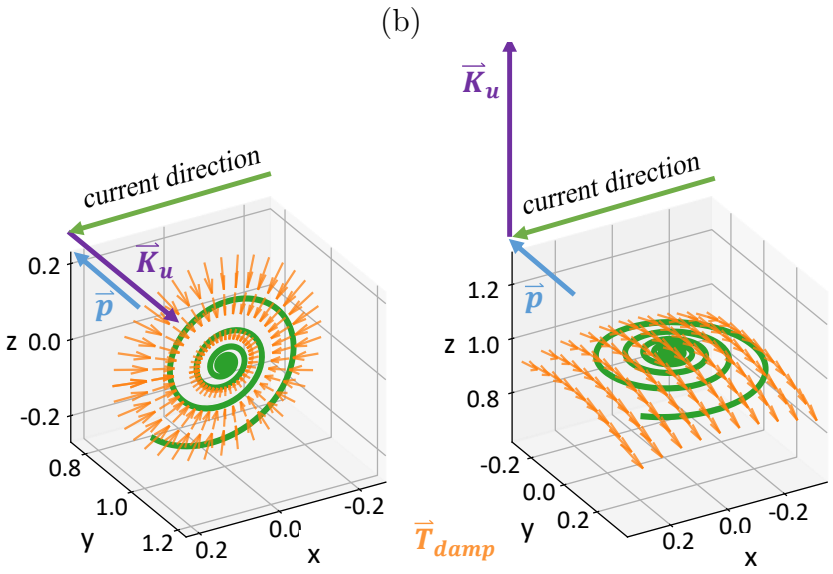

Figure 6: Magnetization trajectory and spin-torque contribution for two model systems. The green line depicts the magnetization trajectory in the three-dimensional space and the orange/brown arrows depict the spin-torque contributions acting on the magnetization. (a) A simplified system featuring only uniaxial anisotropy with $\boldsymbol{K}_u \parallel \hat{y}$ and the damping-like torque, but no external field. Since the current flows in the $\hat{x}$ direction, the spins injected into the system are polarized along $-\hat{y}$ i.e., $\boldsymbol{p} \parallel \hat{y}$. A damping modification is obtained since the torque (orange arrows) directs $\partial_t \boldsymbol{m}$ towards the precessional axis $\boldsymbol{r} \parallel \hat{y}$. (b) If the same system has an out-of-plane anisotropy, the damping of the system is not modified.
Reprinted figure with permission from S. Saha et al., Phys. Rev. B, **101**, p. 224401, 2020, https://doi.org/10.1103/PhysRevB.101.224401. Copyright (2022) by the American Physical Society.

on $\hat{\boldsymbol{v}}$. By looking at these projections

$$\hat{\boldsymbol{v}} \cdot \boldsymbol{L}_\perp = \frac{\alpha\tau_{\mathrm{dl}} - \tau_{\mathrm{fl}}}{1+\alpha^2} \frac{m_x}{\sqrt{1-m_z^2}} \tag{86}$$

$$\hat{\boldsymbol{v}} \cdot \boldsymbol{L}_\parallel = -\frac{\tau_{\mathrm{dl}} + \alpha\tau_{\mathrm{fl}}}{1+\alpha^2} \frac{m_y m_z}{\sqrt{1-m_z^2}} \tag{87}$$

one can see that they are odd functions of m_x and m_y, respectively. This is also illustrated in figure 6(b). Consequently, if the magnetization would move on a

perfect circle around $\hat{\boldsymbol{z}}$, the total current induced damping motion would vanish.

$$\int_0^{2\pi} \hat{\boldsymbol{v}} \cdot \boldsymbol{L}_\perp \, \mathrm{d}\varphi = 0 \tag{88}$$

$$\int_0^{2\pi} \hat{\boldsymbol{v}} \cdot \boldsymbol{L}_\parallel \, \mathrm{d}\varphi = 0 \tag{89}$$

Here, φ denotes the magnetization's azimuthal angle. This indicates that spin torque can only induce a net damping motion if the polarization vector has a non-zero component along the direction of the anisotropy axis. This damping is then not solely due to the dampinglike torque but due to both torques with the effect of the fieldlike torque being reduced by the damping parameter α.
We should point out that the argument is not perfect. For one, we assumed that the magnetization keeps moving on a steady orbit, which cannot be the case in this geometry if there is a torque applied and $\alpha \neq 0$. Secondly, according to (76), the target direction of the magnetization i.e. the direction towards which the damping motion is directed, will lack a contribution along $\boldsymbol{p}$ only in the very special case of the effective field compensating it.
It is very instructive nonetheless and holds approximately true, if the torque is not large enough to shift the rotational axis significantly. The net damping velocities for both of the described simplified systems is calculated in figure 7. The divergence of the integrals of (86) and (87) is a consequence of the convergence direction of the magnetization being misaligned with the rotational axis in the explicit form of the modified LLG.

Let us return to the actual experiment. In the $\phi = 0°$ case, the convergence direction of the magnetization lies within the xz-plane if no current is applied. If there is a current, this position will be shifted either in positive or negative y-direction, depending on the polarity of the bias voltage and for exceedingly large currents, the spin torque will influence the damping as a result. Note that positive and negative current do not result in perfectly symmetric motions however, as the rotational direction does not change. The torques in the simplified systems shown in figure 6 can be contrasted to the torques in the simulations of the actual experiment, which are shown in figure 8.

While the simulation and the measurement show good qualitative agreement, the quantitative difference might be explainable by a larger damping in the experiment due to current induced heating or by additional contributions to the spin-current. For example, the Ta could also inject a spin-current and according to to [35], the torque efficiencies of Ta and Pt are of different sign.

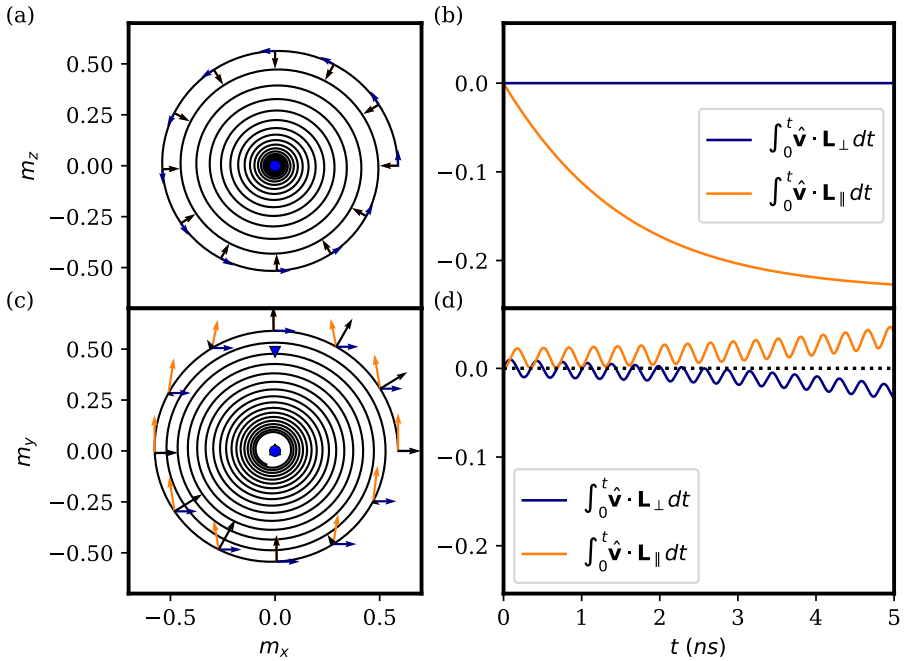

Figure 7: $\boldsymbol{L}_\perp$ and $\boldsymbol{L}_\parallel$ and their contribution to a damping motion for a simplified system with an uniaxial anisotropy as the only other field. $\boldsymbol{L}_\parallel$ is indicated in orange, $\boldsymbol{L}_\perp$ in dark blue. The projection onto the direction towards the anisotropy axis is marked by black arrows. (a) For the case collinear anisotropy axis and polarization, the in-plane component is exactly the damping motion. (b) The out-of-plane component does not contribute to the damping. (c) In case of the anisotropy axis being perpendicular to the polarization, the projections of $\boldsymbol{L}_\perp$ and $\boldsymbol{L}_\parallel$ on the damping direction change only sign under $(m_x, m_y) \to (-m_x, -m_y)$. Ideally, this would mean that they cancel out over a full rotation. (d) Practically, the overall torque-induced damping diverges due to a shift of the convergence direction resulting from the precession axis (blue circle in (a) and (c)) and the damping axis (blue triangle in (a) and (c)) not aligning in the explicit form of the modified LLG (76).

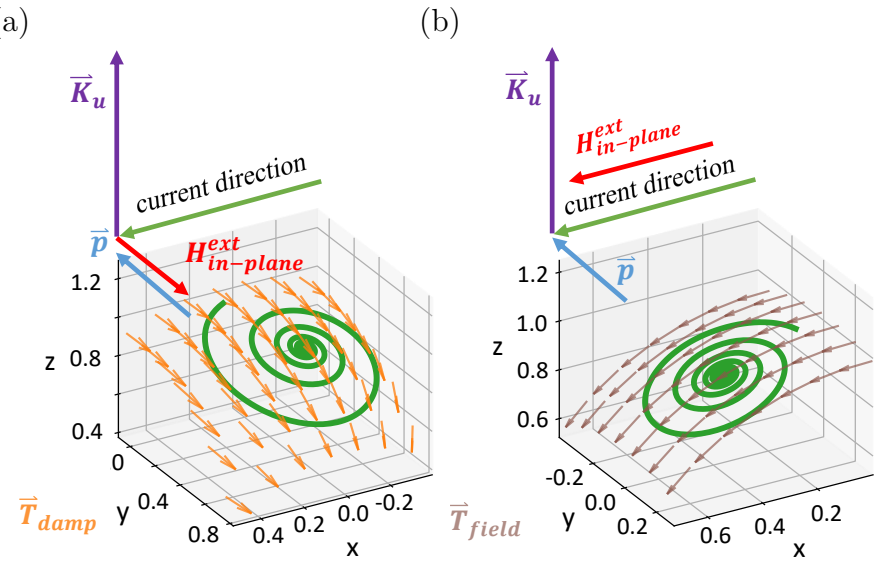

Figure 8: Magnetization trajectory and spin-torque contribution for various model systems. The green line depicts the magnetization trajectory in the three-dimensional space and the orange/brown arrows depict the spin-torque contributions acting on the magnetization. (a) The experimental system with the in-plane component of $\boldsymbol{H}^{\text{eff}}$ parallel to $\hat{y}$. The damping-like torque features a non-vanishing x-component directed towards the center of the rotation, so increasing the damping. (b) The experimental system with only the field-like torque (brown arrows) and with the in-plane component of $\boldsymbol{H}^{\text{eff}}$ directed along $\hat{x}$. No damping modification arises due to the $\boldsymbol{m} \times \boldsymbol{p}$ symmetry of the field-like torque.
Reprinted figure with permission from S. Saha et al., Phys. Rev. B, **101**, p. 224401, 2020, https://doi.org/10.1103/PhysRevB.101.224401. Copyright (2022) by the American Physical Society.

4 Numerical solution of the Schrödinger equation with open boundary conditions

Whenever the spin-drift diffusion model is used, the assumption is that the transport of angular momentum is dominated by scattering events and that the mean free path length is shorter than the characteristic length of the numerical solution. This is assumed to be incorrect for magnetic tunnel junctions and the transport regime is thought to be coherent instead, meaning that scattering events play no significant role and that the transport properties should instead be obtained from the coherent solutions of the Schrödinger equation.
But even starting from the well-known textbook example of tunneling through a potential barrier shows that a numerical solution consistent with the analytical one obtained from matching plane waves at the domain boundaries is not trivially obtained. One particular challenge is posed by the unobstructed propagation of the wave function into and out of the problem region. Boundary conditions that allow for such a behavior are known as open-boundary conditions or transparent boundary conditions and are a major focus of our discussion in this chapter.
We will first show how a spatial varying effective mass can be included into a discrete Hamiltonian and how a varying effective mass influences transverse modes. We will then show how open-boundary conditions can be treated when the Hamiltonian is derived from the midpoint method.

4.1 The finite-differences Hamiltonian

Whatever concrete form $\hat{H}$ will have, we are going to assume that the problem is one-dimensional in nature: we assume that the device is homogeneous perpendicular to the x-direction and that the device has two terminals connected to semi-infinite wires (or leads) from where electrons can enter or leave the device region. Semi-infinite means that the wires have one interface with the device each and that they continue to negative infinity in case of the left wire and to positive infinity in case of the right wire.
Naturally, only a region that encapsulates the device region will be of interest to our analysis. The numerical solutions of the Schrödinger equation will be obtained on a finite differences mesh $\{x_0, x_1, x_2, ..., x_{N-1}\}$ with discretization length a, that contains N nodes (or sites). The outermost nodes x_0 and x_{N-1} are located in the left and right wire region, respectively, as depicted in figure 9.

If the device Hamiltonian with spatially varying effective mass [69] can be written as

$$\hat{H}(x) = -\frac{\hbar^2}{2}\frac{\partial}{\partial x}\left(\frac{1}{m^*(x)}\frac{\partial}{\partial x}\right) + \hat{U}(x) \tag{90}$$

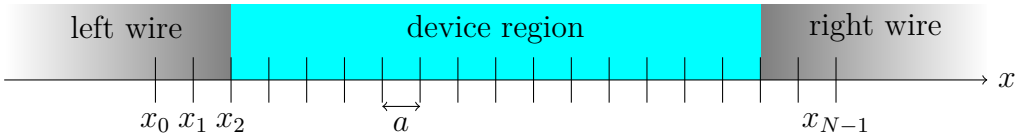

Figure 9: One-dimensional discretization scheme of the device Hamiltonian, including at least two sampling points within each of the semi-infinite homogeneous wires contacting the device on both sides.

then its discretized form can be obtained using a midpoint rule in two steps. First, we determine the discrete spatial derivative of a function $f(x)$

$$\left.\frac{\partial f(x)}{\partial x}\right|_{x=x_i} \to \frac{f_{i+1/2} - f_{i-1/2}}{a} \tag{91}$$

before going on to the full kinetic part

$$\left.-\frac{\hbar^2}{2}\frac{\partial}{\partial x}\left(\frac{1}{m^*(x)}\frac{\partial f(x)}{\partial x}\right)\right|_{x=x_i} \to -\frac{\hbar^2}{2a^2}\left[\frac{f_{i+1} - f_i}{m^*_{i+1/2}} - \frac{f_i - f_{i-1}}{m^*_{i-1/2}}\right]. \tag{92}$$

Therefore, the Hamiltonian reads [70]

$$H_{ij} = \begin{cases} u_i + t_{i-1/2} + t_{i+1/2} & i = j \\ -t_{i+1/2} & j = i+1 \\ -t_{i-1/2} & j = i-1 \\ 0 & \text{else} \end{cases} \tag{93}$$

with $u_i = \hat{U}(x_i)$ and t_i being the hopping energy given by

$$t_i = \frac{\hbar^2}{2m_i^* a^2}. \tag{94}$$

Note how the Hamiltonian (93) depends on the effective mass between the sites.

4.2 Inclusion of transversal components

Not all electrons entering the device region from the leads will have their velocity aligned with x-direction. However, since we assume that the device is homogeneous perpendicular to this direction, the velocity components perpendicular to $\hat{\boldsymbol{x}}$ will cancel out and the net-transport direction is going to be the x-direction.

Nonetheless, components transversal to the net-transport direction will influence the transport properties of the device and should be accounted for. As a result of our assumptions, the solution to the Schrödinger equation can be written as a product.

$$\psi(\epsilon, \boldsymbol{x}) = \psi(\epsilon, x) e^{ik_\perp x_\perp} \tag{95}$$

For a single state, a set of two coordinates $\boldsymbol{x} = (x, x_\perp)$ is sufficient. Plugging the ansatz (95) into the Schrödinger equation reveals a convenient way to handle transversal components [70].

$$\left[\hat{U}(x) - \frac{\hbar^2}{2}\frac{\partial}{\partial x}\left(\frac{1}{m^*(x)}\frac{\partial}{\partial x}\right) - \frac{\hbar^2}{2m^*(x)}\frac{\partial^2}{\partial x_\perp^2}\right]\psi(\epsilon, \boldsymbol{x}) = \epsilon\psi(\epsilon, \boldsymbol{x}) \tag{96}$$

$$\left[\left(\hat{U}(x) + \frac{\hbar^2 k_\perp^2}{2m^*(x)}\right) - \frac{\hbar^2}{2}\frac{\partial}{\partial x}\left(\frac{1}{m^*(x)}\frac{\partial}{\partial x}\right)\right]\psi(\epsilon, \boldsymbol{x}) = \epsilon\psi(\epsilon, \boldsymbol{x}) \tag{97}$$

$$\left[\left(\hat{U}(x) + \epsilon_\perp\big(x\big)\right) - \frac{\hbar^2}{2}\frac{\partial}{\partial x}\left(\frac{1}{m^*(x)}\frac{\partial}{\partial x}\right)\right]\psi(\epsilon, \boldsymbol{x}) = \epsilon\psi(\epsilon, \boldsymbol{x}) \tag{98}$$

$$\left[\hat{U}^{\text{eff}}(x) - \frac{\hbar^2}{2}\frac{\partial}{\partial x}\left(\frac{1}{m^*(x)}\frac{\partial}{\partial x}\right)\right]\psi(\epsilon, x) = \epsilon\psi(\epsilon, x) \tag{99}$$

The energy of the transversal component $\epsilon_\perp(x)$ can be added to the potential to obtain an effective potential [28]

$$\hat{U}^{\text{eff}}(x) = \hat{U}(x) + \epsilon_\perp(x). \tag{100}$$

Two things should be noted. First, the above is also true if $\psi(\epsilon, \boldsymbol{x})$ is spin-dependent since the dispersion relation

$$\epsilon_\perp(x) = \frac{\hbar^2 k_\perp^2}{2m^*(x)} \tag{101}$$

does not depend on the spin. Second, the perpendicular energy contribution (101) is position dependent since the effective mass can vary. Consequently, this treatment assures that the perpendicular momentum component is preserved.

In the special case of a constant effective mass, the perpendicular contribution (101) is also a constant and therefore, it can be used to obtain an effective energy $\epsilon_\parallel = \epsilon - \epsilon_\perp$ instead of an effective potential, which is just the energy corresponding to the momentum component parallel to the transport direction [71].

$$\left[U(x) - \frac{\hbar^2}{2m^*}\frac{\partial^2}{\partial x^2}\right]\psi(\epsilon, x) = (\epsilon - \epsilon_\perp)\,\psi(\epsilon, x) \tag{102}$$

$$\left[U(x) - \frac{\hbar^2}{2m^*}\frac{\partial^2}{\partial x^2}\right]\psi(\epsilon, x) = \epsilon_\parallel\psi(\epsilon, x) \tag{103}$$

4.3 Open boundary conditions

Now that we know the general form of the Hamiltonian, we can address the boundary conditions. Specifically, we are looking for *open* or *transparent* boundary conditions, which means that the electrons propagate inwards and outwards of the problem area $[x_0, x_{N-1}]$ like plane waves. If we would take an analytical approach, this would of course be achieved simply by the ansatz but in our numerical assessment, we have to account for this behavior explicitly.
Keeping in mind that we are taking a single-particle approach with our Hamiltonian, let's focus on an electron entering from the left. For such an electron, the ansatz used to find analytical solutions would be

$$\psi(x)\Big|_{x\in\Omega_{\mathrm{L}}} = A\left[e^{ik_{\mathrm{L}}x} + re^{-k_{\mathrm{L}}x}\right] \tag{104}$$

in the left lead and

$$\psi(x)\Big|_{x\in\Omega_{\mathrm{R}}} = ue^{ik_{\mathrm{R}}x} \tag{105}$$

in the right lead. The wavenumbers are

$$k_m = \frac{1}{\hbar}\sqrt{2m_m^*\left(\epsilon - U_m^{\mathrm{eff}}\right)} \qquad\qquad m = \mathrm{L},\mathrm{R} \tag{106}$$

with ϵ being the energy and with U_m and m_m^* being the potential and effective mass in the leads. After matching these wave functions and their first derivatives with those in the device region at the interfaces, one would obtain a solution that can be scaled by changing the amplitude A.

The situation is very different in the numerical case, however. We cannot simply compute the boundary values from equations (104) and (105) since we do not know the values of reflectivity and transmittivity prior. Also we don't want to simply set the boundary values or require periodic boundary conditions. For one that would alter the solutions but moreover, it would restrict the allowed energies of the electrons to discrete values while the open problem allows for a continuous energy spectrum [70]. What we can do is to use the form of the Hamiltonian (93) within homogeneous domains such as the wires and the above ansatz to calculate a mixture of boundary conditions that satisfies our requirement of transparent boundaries.

On the right boundary, the situation is straight forward. At the outermost node, we have

$$t_{\mathrm{R}}\psi_{N-2} + (\epsilon - h_{\mathrm{R}})\psi_{N-1} + t_{\mathrm{R}}\psi_N = 0 \tag{107}$$

with h_{R} being the main diagonal entry of the Hamiltonian within the right lead. Since the solution should just propagate outwards like a plane wave according to

(105), we do know that

$$\psi_N = \psi_{N-1} e^{ik_{\mathrm{R}}a} \tag{108}$$

and thus, we have

$$t_{\mathrm{R}}\psi_{N-2} + (\epsilon - h_{\mathrm{R}} + t_{\mathrm{R}} e^{ik_{\mathrm{R}}a})\psi_{N-1} = 0. \tag{109}$$

at the right boundary.

The situation is more complicated on the left boundary. In addition to the outgoing reflected part, an incoming wave has to be accounted for. We start of by calculating the tight-binding dispersion relation. Within a homogeneous potential,

$$t\psi_{-1} + (\epsilon - h)\psi_0 + t\psi_1 = 0 \tag{110}$$

$$te^{-ika} + (\epsilon - h) + te^{ika} = 0 \tag{111}$$

holds true for a plane waves $\psi_i = C\exp(ikx_i)$. Therefore,

$$(\epsilon - U) = 2t\left[1 - \cos\left(ka\right)\right] \tag{112}$$

gives the relation between wavenumber and energy [72]. This relation can also be written down equivalently as

$$(\epsilon - h) = -t\left(e^{ika} + e^{-ika}\right) \tag{113}$$

which is the version we are going to use here. We precede similar to as we did for the right boundary, but for the first site outside of the problem region and using (104).

$$t_{\mathrm{L}}\psi_{-2} + (\epsilon - h_{\mathrm{L}})\psi_{-1} + t_{\mathrm{L}}\psi_0 = 0 \tag{114}$$

$$t_{\mathrm{L}}A\left[e^{-ik_{\mathrm{L}}a} + re^{ik_{\mathrm{L}}a}\right] + (\epsilon - h_{\mathrm{L}})A\left[1 + r\right] + t_{\mathrm{L}}\psi_0 = 0 \tag{115}$$

$$t_{\mathrm{L}}Ae^{-ik_{\mathrm{L}}a} + rA\left[t_{\mathrm{L}}e^{ik_{\mathrm{L}}a} + (\epsilon - h_{\mathrm{L}})\right] + (\epsilon - h_{\mathrm{L}})A + t_{\mathrm{L}}\psi_0 = 0 \tag{116}$$

$$rA\left[t_{\mathrm{L}}e^{ik_{\mathrm{L}}a} + (\epsilon - h_{\mathrm{L}})\right] = -t_{\mathrm{L}}Ae^{-ik_{\mathrm{L}}a} - (\epsilon - h_{\mathrm{L}})A - t_{\mathrm{L}}\psi_0 \tag{117}$$

$$rA = \frac{-t_{\mathrm{L}}Ae^{-ik_{\mathrm{L}}a} - (\epsilon - h_{\mathrm{L}})A - t_{\mathrm{L}}\psi_0}{t_{\mathrm{L}}e^{ik_{\mathrm{L}}a} + (\epsilon - h_{\mathrm{L}})} \tag{118}$$

This reflected amplitude can be rewritten as

$$rA = -Ae^{i2k_{\mathrm{L}}a} + \psi_0\, e^{ik_{\mathrm{L}}a} \tag{119}$$

due to equation (113). We look now at the next equation, centered on x_0 and plug in the above coefficient.

$$t_{\mathrm{L}}\psi_{-1} + (\epsilon - h_{\mathrm{L}})\psi_0 + t_{\mathrm{L}}\psi_1 = 0 \tag{120}$$

$$t_{\mathrm{L}}A\left[1 + r\right] + (\epsilon - h_{\mathrm{L}})\psi_0 + t_{\mathrm{L}}\psi_1 = 0 \tag{121}$$

$$t_{\mathrm{L}}\left[A - Ae^{i2k_{\mathrm{L}}a} + \psi_0\, e^{ik_{\mathrm{L}}a}\right] + (\epsilon - h_{\mathrm{L}})\psi_0 + t_{\mathrm{L}}\psi_1 = 0 \tag{122}$$

$$t_{\mathrm{L}}A(1 - e^{i2k_{\mathrm{L}}a}) + t_{\mathrm{L}}\psi_0 e^{ik_{\mathrm{L}}a} + (\epsilon - h_{\mathrm{L}})\psi_0 + t_{\mathrm{L}}\psi_1 = 0 \tag{123}$$

This last expression contains a term equivalent to the one obtained for the right boundary, but also an additional source term

$$S = -t_{\mathrm{L}} A \left(1 - e^{i2k_{\mathrm{L}}a}\right). \tag{124}$$

Thus, the equation at the left boundary reads

$$(\epsilon - h_{\mathrm{L}} + t_{\mathrm{L}} e^{ik_{\mathrm{L}}a})\psi_0 + t_{\mathrm{L}}\psi_1 = S \tag{125}$$

and the full problem for electrons entering from the left is therefore stated by the system of equations (126).

$$\begin{cases} (\epsilon - h_{00} + t_{\mathrm{L}} e^{ik_{\mathrm{L}}a})\psi_0 - h_{01}\psi_1 = S \\ -h_{i\,i-1}\psi_{i-1} + (\epsilon - h_{ii}) - h_{i\,i+1}\psi_{i+1} = 0 \qquad i \in \{1, 2, \ldots, N-2\} \\ -h_{N-1\,N-2}\psi_{N-2} + (\epsilon - h_{N-1\,N-1} + t_{\mathrm{R}} e^{ik_{\mathrm{R}}a})\psi_{N-1} = 0 \end{cases} \tag{126}$$

5 The non-equilibrium Green's function formalism

The tridiagonal system obtained in the previous chapter can be solved by a suitable algorithm like for example the Thomas algorithm. In case one is not concerned with the individual wave functions but only wants to calculate derived properties like the probability density and the probability current, the non-equilibrium Green's function (NEGF) formalism provides a framework to do so. In the end, the solutions will be equivalent, but the density and current are calculated simultaneously.
This introduction to the formalism follows in large parts the book by Datta [72] on the subject. In the end, we will have to introduce spin back into our considerations but at this point, it would only clutter the comparison we are going to make to the previous chapter.

5.1 The retarded Green's function

The first step within the framework of this formalism is to determine the so-called retarded Green's function G^R. In the case of a device connected to two semi-infinite leads, which is the same problem as depicted in figure 9, the full Green's function is given by [73]

$$\begin{bmatrix} \mathbb{1}\epsilon - H_\mathrm{L} & \tau_\mathrm{L} & 0 \\ \tau_\mathrm{L}^\dagger & \mathbb{1}\epsilon - H_d & \tau_\mathrm{R}^\dagger \\ 0 & \tau_\mathrm{R} & \mathbb{1}\epsilon - H_\mathrm{R} \end{bmatrix} \begin{bmatrix} G_\mathrm{L} & G_{\mathrm{L}d} & G_\mathrm{LR} \\ G_{d\mathrm{L}} & G_d & G_{d\mathrm{R}} \\ G_\mathrm{RL} & G_{\mathrm{R}d} & G_\mathrm{R} \end{bmatrix} = \begin{bmatrix} \mathbb{1} & 0 & 0 \\ 0 & \mathbb{1} & 0 \\ 0 & 0 & \mathbb{1} \end{bmatrix} \tag{127}$$

with H_d and G_d being an $N \times N$ matrix, while all other matrices are of infinite length in one or both dimensions. One could calculate the uncoupled Green's function corresponding to all three regions in figure 9 separately by matrix inversion

$$g_\mathrm{L} = [\mathbb{1}\epsilon - H_\mathrm{L}]^{-1} \tag{128}$$

$$g_d = [\mathbb{1}\epsilon - H_d]^{-1} \tag{129}$$

$$g_\mathrm{R} = [\mathbb{1}\epsilon - H_\mathrm{R}]^{-1} \tag{130}$$

but those belong to subsystems that do not interact with each other. The coupling in (127) is due to the matrices τ_L and τ_R, which have only a single non-zero entry, t_L and t_R at the respective boundary to the device region. The Green's function of the device region G_d is related to the leads via the following equations.

$$[\mathbb{1}\epsilon - H_\mathrm{L}]\, G_{\mathrm{L}d} + \tau_\mathrm{L} G_d = 0 \tag{131}$$

$$[\mathbb{1}\epsilon - H_d]\, G_d + \tau_\mathrm{L}^\dagger G_{\mathrm{L}d} + \tau_\mathrm{R}^\dagger G_{\mathrm{R}d} = \mathbb{1} \tag{132}$$

$$[\mathbb{1}\epsilon - H_\mathrm{R}]\, G_{\mathrm{R}d} + \tau_\mathrm{R} G_d = 0. \tag{133}$$

Inserting (128) and (130) into (131) and (133) yields

$$G_{\mathrm{L}d} = -g_{\mathrm{L}}\tau_{\mathrm{L}}G_d \tag{134}$$

$$G_{\mathrm{R}d} = -g_{\mathrm{R}}\tau_{\mathrm{R}}G_d \tag{135}$$

which can be in turn be plugged into (132).

$$\left[\mathbb{1}\epsilon - H_d - \tau_{\mathrm{L}}^{\dagger}g_{\mathrm{L}}\tau_{\mathrm{L}} - \tau_{\mathrm{R}}^{\dagger}g_{\mathrm{R}}\tau_{\mathrm{R}}\right] G_d = \mathbb{1} \tag{136}$$

If the isolated Green's functions on the non-interacting leads g_{L} and g_{R} are known, equation (136) allows us to calculate the fully interacting Green's function in the device region.

For homogeneous leads, this is the case. First, we should take note of the fact that (136) requires no knowledge of g_{L} and g_{R} at any other point than the ones adjacent to the device region. We will enumerate the nodes in the leads counting away from the device region boundary such that the one closest to device region is the node with the number 0. At this node, we have

$$tg_{10} + (\epsilon - h)\, g_{00} = 1 \tag{137}$$

and since h is a constant

$$g_{10} = g_{00}e^{ika} \tag{138}$$

holds true. Note that in the case of the left lead, the solution has a negative wavenumber, but we are counting nodes in the negative direction while for the right lead, the wavenumber is positive, and we are counting in the positive direction. From equations (137) and (138) and the tight-binding dispersion (113), we can easily see that the sought-after value of the non-interacting Green's function in the leads is

$$g_{00} = -\frac{1}{t}e^{ika}. \tag{139}$$

We can now rewrite equation (136) to

$$\left[\epsilon - H_d - \Sigma^R\right] G^R = \mathbb{1} \tag{140}$$

with Σ^R being the *self-energy* matrix

$$\Sigma^R = \begin{cases} \Sigma_{\mathrm{L}}^R & i = j = 0 \\ \Sigma_{\mathrm{R}}^R & i = j = N-1 \\ 0 & \text{else} \end{cases} \tag{141}$$

composed of the self-energies corresponding to the interaction with the left and right leads

$$\Sigma_{\mathrm{L}}^R = -t_{\mathrm{L}}e^{ik_{\mathrm{L}}a} \tag{142}$$

$$\Sigma_{\mathrm{R}}^R = -t_{\mathrm{R}}e^{ik_{\mathrm{R}}a}. \tag{143}$$

The meaning of these specific self-energy functions can also be inferred by comparing them to the open boundary condition without an incoming wave (109), that we have obtained for numerical solutions of the Schrödinger equation earlier.

In equation (140), we have also changed the notation from the coupled or interacting device Green's function G_d to the retarded Green's function G^R since we were able to drop the semi-infinite leads from our description. In this context, "retarded" means that the Green's function G^R_{ij} describes the reaction of the system at x_i to a unit-perturbation at the position x_j. The advanced Green's function

$$G^A = G^{R\dagger} \tag{144}$$

on the other hand could be thought of as the behavior leading up to an absorption at the position x_j.

5.2 The non-equilibrium Green's function

With a method to calculate the retarded Green's function, we can now proceed to the non-equilibrium Green's function G^n. It is obtained from the kinetic equation

$$G^n = G^R \Sigma^{\text{in}} G^A \tag{145}$$

that involves the in-scattering matrix

$$\Sigma^{\text{in}} = \begin{cases} f_{\text{L}}(\epsilon)\Gamma_{\text{L}} & i = j = 0 \\ f_{\text{R}}(\epsilon)\Gamma_{\text{R}} & i = j = N-1 \\ 0 & \text{else} \end{cases} \tag{146}$$

with the occupation functions $f_{\text{L}}(\epsilon)$ and $f_{\text{R}}(\epsilon)$ as well as the broadening functions

$$\Gamma_{\text{L}} = i\left(\Sigma^R_{\text{L}} - \overline{\Sigma^R_{\text{L}}}\right) = 2t_{\text{L}} \sin(k_{\text{L}} a) \tag{147}$$

$$\Gamma_{\text{R}} = i\left(\Sigma^R_{\text{R}} - \overline{\Sigma^R_{\text{R}}}\right) = 2t_{\text{R}} \sin(k_{\text{R}} a)\,. \tag{148}$$

Our objective now is to show that

$$G^n_{ij} = 2\pi a \sum\nolimits_k \psi_k(x_i)\overline{\psi_k(x_j)} \tag{149}$$

holds true, thus, that the non-equilibrium Green's function is in fact some sort of correlation coefficient with its main diagonal being proportional to the (occupied) local density. The sum in (149) is over all states i.e. over both spin states of the wave function entering from the left lead and the wave function entering from the right lead.

To do so, we start from the kinetic equation (145) and realize that due to the form of (146) the non-equilibrium Green's function itself can be decomposed into two parts, one for wave functions entering from the left lead and one for wave functions entering from the right lead.

$$G^n_{ij} = \sum_{k=0}^{N-1}\sum_{l=0}^{N-1} G^R_{ik}\Sigma^{\text{in}}_{kl}G^A_{lj} \tag{150}$$

$$= \sum_{k=0}^{N-1} G^R_{ik}\left[\Sigma_L\delta_{k0}G^A_{0j} + \Sigma_R\delta_{k\,N-1}G^A_{N-1\,j}\right] \tag{151}$$

$$= G^R_{i0}\Sigma_L G^A_{0j} + G^R_{i\,N-1}\Sigma_R G^A_{N-1\,j} \tag{152}$$

$$= G^R_{i0}\Sigma_L \overline{G^R}_{j0} + G^R_{i\,N-1}\Sigma_R \overline{G^R}_{j\,N-1} \tag{153}$$

Let's focus on the first part i.e. wave functions entering from the left. The only relevant part of the retarded Green's function G^R seems to be its first column which is the solution to a sub-problem of (140).

$$\sum_{j=0}^{N-1}\left[\epsilon\delta_{ij} - H_{ij} - \Sigma^R_{ij}\right]G^R_{j0} = \delta_{i0} \tag{154}$$

This is very similar to the numerical solution of the Schrödinger equation with the open boundary conditions (126) we derived earlier. Actually, when comparing the open boundary conditions (125) and (109) with the self-energy matrix (141), (126) can be rewritten as

$$\sum_{j=0}^{N-1}\left[\epsilon\delta_{ij} - H_{ij} - \Sigma^R_{ij}\right]\psi_j = S\delta_{i0} \tag{155}$$

The comparison of (154) and (155) indicates that the relation between the first column of the retarded Green's function and the solution to (126) should be

$$G^R_{j0}\,S = \psi_j \tag{156}$$

which is of course not necessarily unexpected since $S\delta_{i0}$ could be viewed as a source term and convolution with the problem's Green's function should therefore yield the full solution of the problem.

We now look again at (149), (153) and (156). Apparently, the in-scattering matrix is proportional to the square norm of the value S that is given by (124). The square norm of S is proportional to the square norm of the incoming wave function $|A|^2$,

but this is of course just the 1D density of states times the occupation function.

$$|S|^2 = t^2|A|^2\left(1-e^{i2ka}\right)\left(1-e^{-i2ka}\right) \tag{157}$$

$$= t^2 f(\epsilon)\frac{m^*}{2\pi\hbar^2 k}\left(1-e^{i2ka}\right)\left(1-e^{-i2ka}\right) \tag{158}$$

$$= t^2 f(\epsilon)\frac{1}{2\pi\hbar\nu}4\sin^2(ka) \tag{159}$$

$$= \frac{1}{2\pi a}2tf(\epsilon)\sin(ka) \tag{160}$$

In the last step, we used the derivative of the tight binding dispersion (112), which can be used to calculate the velocity

$$\hbar\nu = 2at\sin(ka) \tag{161}$$

and we can now see that the kinetic equation (145) does indeed yield a solution that satisfies (149). We should stress that we have used the density of states for just a single spin direction, so that the sum in (149) has to account for spin-up and spin-down states. We have done so to keep the statements made in this chapter easier to compare with the spin-polarized considerations in later chapters.

5.3 Current calculation

We will now make use of relation (149) to calculate the probability current flowing through the device. This current is calculated from the solution of the Schrödinger equation via

$$j = \frac{\hbar}{2m^* i}\left(\psi^*\frac{\partial\psi}{\partial x} - \psi\frac{\partial\psi^*}{\partial x}\right) \tag{162}$$

in the one-dimensional case. If non-interacting particles in multiple states k contribute to the total current with their corresponding wave functions, the overall current can be written as a sum of the individual currents.

$$j = \sum_k j_k \tag{163}$$

Numerically, the current due to a single particle at site p is

$$j_{k,p} = \frac{\hbar}{2am_p^* i}\left[\psi_{k,p}^*\left(\psi_{k,p+1}-\psi_{k,p}\right) - \psi_{k,p}\left(\psi_{k,p+1}^*-\psi_{k,p}^*\right)\right] \tag{164}$$

$$= \frac{\hbar}{2am_p^* i}\left[\psi_{k,p}^*\psi_{k,p+1} - \psi_{k,p}^*\psi_{k,p} - \psi_{k,p}\psi_{k,p+1}^* + \psi_{k,p}\psi_{k,p}^*\right] \tag{165}$$

$$= \frac{\hbar}{2am_p^* i}\left[\psi_{k,p}^*\psi_{k,p+1} - \psi_{k,p}\psi_{k,p+1}^*\right] \tag{166}$$

$$\tag{167}$$

and therefore, the total current is

$$j_p = \frac{\hbar}{2am_p^* i} \sum_k \left[\psi_{k,p}^* \psi_{k,p+1} - \psi_{k,p} \psi_{k,p+1}^* \right]. \tag{168}$$

Comparison with (149) indicates now that

$$j_p = \sum_k \frac{\hbar}{4\pi a^2 m_p^* i} \left[G_{p+1,p}^n - G_{p,p+1}^n \right] \tag{169}$$

$$= \frac{it_p}{2\pi\hbar} \left[G_{p,p+1}^n - G_{p+1,p}^n \right] \tag{170}$$

meaning that at site p, the current can be obtained directly from the off-diagonal elements of the non-equilibrium Greens function G^n.

6 Coherent transport in magnetic tunnel junctions

So far, we did not consider the electron's spin for our discussion of the coherent transport problem. However, for the description of electrons flowing through a magnetic tunnel junction, we will need to do so.
We are assuming that within a ferromagnetic layer, the local magnetization arises from the localized d-electrons while charge and angular momentum are transported by the non-localized s-electrons. The exchange interaction of the two introduces an energy-splitting of the potential the s-electron feels within the ferromagnetic domain.
Such a spin-dependent potential can be achieved by changing the finite differences Hamiltonian (93) from an $N \times N$ matrix to a $2N \times 2N$ matrix, meaning that every element H_{ij} becomes a 2×2 matrix [28, 71]. The general form of this spin-dependent version of the Hamiltonian reads

$$H_{ij} = \begin{cases} u_i + \left(t_{i-1/2} + t_{i+1/2}\right) \mathbb{1}_2 & i = j \\ -t_{i+1/2}\mathbb{1}_2 & j = i+1 \\ -t_{i-1/2}\mathbb{1}_2 & j = i-1 \\ 0_{2,2} & \text{else} \end{cases} \tag{171}$$

where $\mathbb{1}_2$ denotes the 2×2 identity matrix and $0_{2,2}$ is a zero matrix of the same size. Let's assume that the spin is polarized along the z-direction. If $U_i^{\uparrow} = U^{\uparrow}(x_i)$ is the spin up potential and $U_i^{\downarrow} = U^{\downarrow}(x_i)$ the spin down potential, then the potential in (171) is given by (172).

$$u_i = \left\{u_i^{\sigma\sigma'}\right\} = \begin{bmatrix} U_i^{\uparrow} & 0 \\ 0 & U_i^{\downarrow} \end{bmatrix} \qquad \text{(polarized along } \hat{\boldsymbol{z}}\text{)} \tag{172}$$

For our purposes, however, it has to be possible to vary the spin quantization axis locally, which can be achieved by rotating (172) to an arbitrary direction $\hat{\boldsymbol{n}}$. The resulting matrix can be rewritten as [74]

$$u_i = U_i \mathbb{1}_2 - \frac{J_i}{2}\, \hat{\boldsymbol{n}} \cdot \boldsymbol{s} \qquad \text{(polarized along } \hat{\boldsymbol{n}}\text{)} \tag{173}$$

with $\boldsymbol{\sigma} = (\sigma_x, \sigma_y, \sigma_z)^{\mathrm{T}}$ being the Pauli matrix vector and with the mean and spin-split potentials

$$U_i = \left(U_i^{\downarrow} + U_i^{\uparrow}\right)/2 \tag{174}$$

$$J_i = U_i^{\downarrow} - U_i^{\uparrow}. \tag{175}$$

It is straight forward to show that the expectation values of (173) are as expected

$$\langle \pm x | \, u_i \, | \pm x \rangle = U_i \pm J_i n_x / 2 \tag{176}$$
$$\langle \pm y | \, u_i \, | \pm y \rangle = U_i \pm J_i n_y / 2 \tag{177}$$
$$\langle \pm z | \, u_i \, | \pm z \rangle = U_i \pm J_i n_z / 2. \tag{178}$$

In the case of ferromagnetic materials, the local magnetization direction $\boldsymbol{m}_i$ indicates the spin quantization axis. Since the electron's spin and angular momentum point into opposite directions, meaning that the magnetization $\boldsymbol{m}_i$ is due to spins being directed into the $-\boldsymbol{m}_i$ direction, the local quantization axis is $\hat{\boldsymbol{n}} = -\boldsymbol{m}_i$.
The direction of the polarization in equation (173) can vary from site to site but within a thin ferromagnetic layer, it might be sufficient to assume a constant magnetization. This is because the exchange length is usually longer than the layer thickness of the stacks that we will investigate. From a more technical point of view, the same argument justifies that we are going to solve the Landau-Lifshitz-Gilbert equation (28) on a finite-element mesh with an average discretization length about an order of magnitude larger than the discretization of the finite-differences mesh used to compute the spintronic properties. In essence, this means that if the magnetization would vary strongly on the finite differences mesh, then the micromagnetic assumption would be violated.

6.1 Modeling of a magnetic tunnel junction

Now that we have clarified how the spin-dependent potential can be handled, it is a good time to ask how the discrete Hamiltonian of a magnetic tunnel junction looks specifically.

A basic tunnel junction consists of two ferromagnetic layers (FM1 and FM2) of length L_{FM1} and L_{FM2}, connected by a barrier region (B) of length L_{B}. The device is modeled to be contacted on both ends with two semi-infinite leads (L and R). The spacing a has to be chosen such that all interfaces lie on sampling points. As a convention, the left interface of the barrier region i.e. the FM1/B interface acts as the spatial origin.
We assume the spin-dependent potential and the effective mass are constant within domains, so that the device can be characterized by five sets of material parameters (U_m, J_m, m_m^*) with the index $m \in \{\mathrm{L}, \mathrm{FM1}, \mathrm{B}, \mathrm{FM2}, \mathrm{R}\}$ denoting the domain. The splitting J_m is only non-zero in the ferromagnetic layers FM1 and FM2. On the interfaces, the values of these parameters are averaged.
Since the resistivity of the insulator is much larger than the resistivity of all other layers, it is reasonable to assume that the voltage V_b applied to the device will drop solely on the insulator. Therefore, the potential landscape is altered by the

bias voltage induced potential (179).

$$v_i = \begin{cases} -eV_b/2 & z_i \leq 0 \\ z_i eV_b/L_\mathrm{B} - eV_b/2 & 0 < z_i < L_\mathrm{B} \\ eV_b/2 & L_\mathrm{B} \leq z_i \end{cases} \tag{179}$$

Putting together all the above assumptions yields the device Hamiltonian for magnetic tunnel junctions given by [28]

$$H_{ij}\left(k_\perp\right) = \begin{cases} h_m(k_\perp) + v_i \mathbb{1}_2 & i = j \\ -t_m \mathbb{1}_2 & j = i \pm 1 \\ 0_{2,2} & \text{else} \end{cases} \qquad \text{(within domains)} \tag{180}$$

for sites lying within the domain m and by

$$H_{ij}\left(k_\perp\right) = \begin{cases} \left[h_m(k_\perp) + h_n(k_\perp)\right]/2 + v_i \mathbb{1}_2 & i = j \\ -t_m \mathbb{1}_2 & j = i - 1 \\ -t_n \mathbb{1}_2 & j = i + 1 \\ 0_{2,2} & \text{else} \end{cases} \qquad \text{(on interfaces)} \tag{181}$$

for sites lying on interfaces between the domains m and n. The on-site energy

$$h_m(k_\perp) = \left(U_m + 2t_m + \frac{\hbar^2 k_\perp^2}{2m_m^*}\right) \mathbb{1}_2 + \frac{J_m}{2} \boldsymbol{m}_m \cdot \boldsymbol{\sigma} \tag{182}$$

is simply the main diagonal entry of (171) with the potential U_i modified according to (100) in order to account for transversal velocity components of the electrons entering the device region.
The above description can be compared to figure 10 in which the modeling of a magnetic tunnel junction is illustrated.

6.2 Spin-dependent open boundary conditions

We are now going to examine what the spin-dependence means for the open boundary conditions. For non-magnetic leads, the derivation from chapter 4.3 is still correct, but how do these boundary conditions look in the case of magnetic leads? In chapter 4.3, we derived them for electrons entering from the left and started from (104) and (105) i.e. we assumed that a wave function of amplitude A enters from the left and is reflected back in the left lead with ratio r and transmits into the right lead with ratio u.

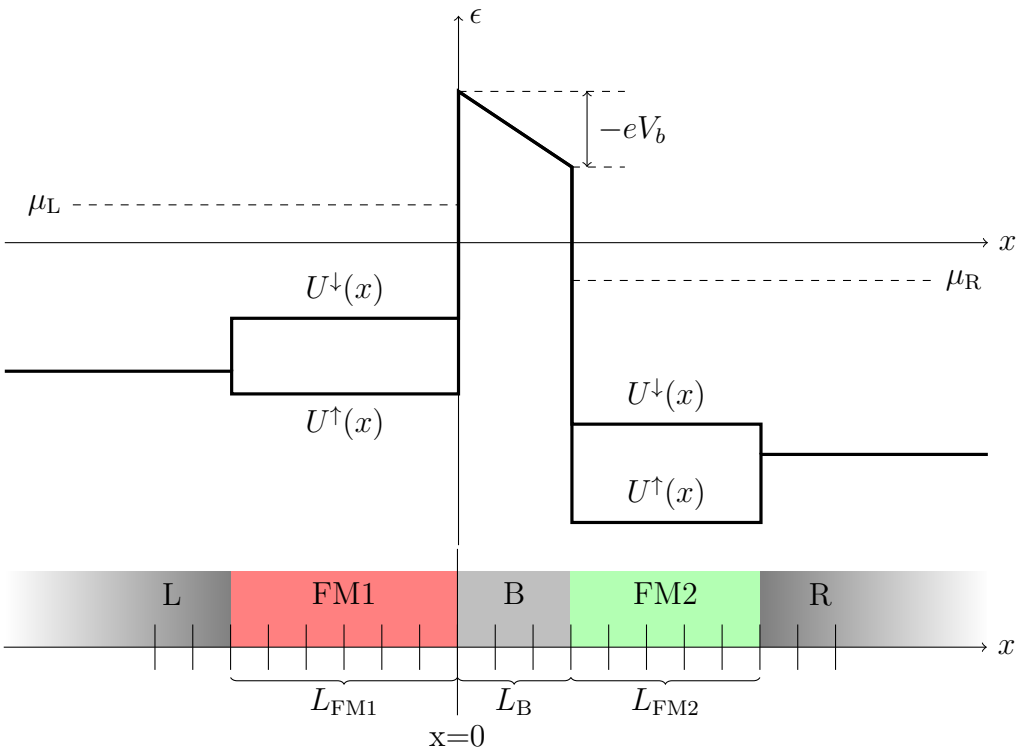

Figure 10: Modeling of magnetic tunnel junctions in finite differences. Within ferromagnetic domains, the potential felt by an electron depends on its spin. The entire voltage is assumed to drop at the insulator, inducing a shift by $\pm eV_b/2$ of the potentials and the chemical potentials μ_L and μ_R left and right of it. As convention, the left FM/B-interface is taken as origin. All interfaces have to lie on sample points.

The spin-polarized version of the ansatz [24] is a bit more complicated than (104) and (105). For a spin-up electron entering from the left, it reads

$$\psi^{(\uparrow)\uparrow}(x)\Big|_{x\in\Omega_\mathrm{L}} = A^\uparrow\left[e^{ik_\mathrm{L}^\uparrow x} + r^\uparrow e^{-k_\mathrm{L}^\uparrow x}\right] \tag{183}$$

$$\psi^{(\uparrow)\downarrow}(x)\Big|_{x\in\Omega_\mathrm{L}} = r^\downarrow e^{-k_\mathrm{L}^\downarrow x} \tag{184}$$

in the left lead and

$$\psi^{(\uparrow)\uparrow}(x)\Big|_{x\in\Omega_\mathrm{R}} = u^\uparrow e^{ik_\mathrm{R}^\uparrow x} \tag{185}$$

$$\psi^{(\uparrow)\downarrow}(x)\Big|_{x\in\Omega_\mathrm{R}} = u^\downarrow e^{ik_\mathrm{R}^\downarrow x} \tag{186}$$

in the right lead. Likewise, if an electron enters the problem region from the left in the spin-down state, the wave functions in the leads would be

$$\psi^{(\downarrow)\uparrow}(x)\Big|_{x\in\Omega_{\mathrm{L}}} = r^{\uparrow}e^{-k_{\mathrm{L}}^{\uparrow}x} \tag{187}$$

$$\psi^{(\downarrow)\downarrow}(x)\Big|_{x\in\Omega_{\mathrm{L}}} = A^{\downarrow}\left[e^{ik_{\mathrm{L}}^{\downarrow}x} + r^{\downarrow}e^{-k_{\mathrm{L}}^{\downarrow}x}\right] \tag{188}$$

in the left lead and

$$\psi^{(\downarrow)\uparrow}(x)\Big|_{x\in\Omega_{\mathrm{R}}} = u^{\uparrow}e^{ik_{\mathrm{R}}^{\uparrow}x} \tag{189}$$

$$\psi^{(\downarrow)\downarrow}(x)\Big|_{x\in\Omega_{\mathrm{R}}} = u^{\downarrow}e^{ik_{\mathrm{R}}^{\downarrow}x} \tag{190}$$

in the right lead. In the above expressions, we adopted the notation of reference [24] and indicate the original spin-state in brackets.
As before, we will first focus on the situation at the right. If the spin-quantization axis in the right lead is along the z-direction, then (185), (186), (189) and (190) yield

$$t_{\mathrm{R}}\left|\psi_{N-2}^{(\uparrow)}\right\rangle + \left[\mathbb{1}_2\epsilon - h_{\mathrm{R}} + t_{\mathrm{R}}\begin{bmatrix} e^{ik_{\mathrm{R}}^{\uparrow}a} & 0 \\ 0 & e^{ik_{\mathrm{R}}^{\downarrow}a}\end{bmatrix}\right]\left|\psi_{N-1}^{(\uparrow)}\right\rangle = 0 \tag{191}$$

and

$$t_{\mathrm{R}}\left|\psi_{N-2}^{(\downarrow)}\right\rangle + \left[\mathbb{1}_2\epsilon - h_{\mathrm{R}} + t_{\mathrm{R}}\begin{bmatrix} e^{ik_{\mathrm{R}}^{\uparrow}a} & 0 \\ 0 & e^{ik_{\mathrm{R}}^{\downarrow}a}\end{bmatrix}\right]\left|\psi_{N-1}^{(\downarrow)}\right\rangle = 0 \tag{192}$$

with the states at position i being

$$\left|\psi_i^{(\uparrow)}\right\rangle = \begin{bmatrix}\psi_i^{(\uparrow)\uparrow} \\ \psi_i^{(\uparrow)\downarrow}\end{bmatrix} \qquad \text{and} \qquad \left|\psi_i^{(\downarrow)}\right\rangle = \begin{bmatrix}\psi_i^{(\downarrow)\uparrow} \\ \psi_i^{(\downarrow)\downarrow}\end{bmatrix}. \tag{193}$$

These two equations can be combined into one.

$$t_{\mathrm{R}}\begin{bmatrix}\psi_{N-2}^{(\uparrow)\uparrow} & \psi_{N-2}^{(\downarrow)\uparrow} \\ \psi_{N-2}^{(\uparrow)\downarrow} & \psi_{N-2}^{(\downarrow)\downarrow}\end{bmatrix} + \left[\mathbb{1}_2\epsilon - h_{\mathrm{R}} + t_{\mathrm{R}}\begin{bmatrix} e^{ik_{\mathrm{R}}^{\uparrow}a} & 0 \\ 0 & e^{ik_{\mathrm{R}}^{\downarrow}a}\end{bmatrix}\right]\begin{bmatrix}\psi_{N-1}^{(\uparrow)\uparrow} & \psi_{N-1}^{(\downarrow)\uparrow} \\ \psi_{N-1}^{(\uparrow)\downarrow} & \psi_{N-1}^{(\downarrow)\downarrow}\end{bmatrix} = 0 \tag{194}$$

In general, the spin-quantization axis can lie in an arbitrary direction $-\boldsymbol{m}_{\mathrm{R}}$, but equation (194) can be easily transformed by the unitary matrix $R(\hat{\boldsymbol{n}})$ that rotates from $\hat{\boldsymbol{z}}$ to $\hat{\boldsymbol{n}}$ to express this. Applying $R(-\boldsymbol{m}_{\mathrm{R}})$ to the state vectors (193) yields the new state matrix

$$\Psi_i = R(-\boldsymbol{m}_{\mathrm{R}})\cdot\left[\left|\psi_i^{(\uparrow)}\right\rangle, \left|\psi_i^{(\downarrow)}\right\rangle\right] = R(-\boldsymbol{m}_{\mathrm{R}})\cdot\begin{bmatrix}\psi_i^{(\uparrow)\uparrow} & \psi_i^{(\downarrow)\uparrow} \\ \psi_i^{(\uparrow)\downarrow} & \psi_i^{(\downarrow)\downarrow}\end{bmatrix} \tag{195}$$

that is used in the general form of equation (194)

$$t_{\mathrm{R}}\Psi_{N-2} + \left[\mathbb{1}_2\epsilon - h_{\mathrm{R}} - \Sigma_{\mathrm{R}}^R\right]\Psi_{N-1} = 0 \tag{196}$$

with the self-energy matrix [71]

$$\Sigma_{\mathrm{R}}^R = R(-\boldsymbol{m}_{\mathrm{R}}) \cdot \begin{bmatrix} -t_{\mathrm{R}} e^{ik_{\mathrm{R}}^{\uparrow} a} & 0 \\ 0 & -t_{\mathrm{R}} e^{ik_{\mathrm{R}}^{\downarrow} a} \end{bmatrix} \cdot R^{\dagger}(-\boldsymbol{m}_{\mathrm{R}}). \tag{197}$$

Likewise, we can proceed for the left lead with (183), (184), (187) and (188) analogous to chapter 4.3. In a coordinate system with the spin-quantization axis along the z-direction, this results in

$$\left[\mathbb{1}_2\epsilon - h_{\mathrm{L}} + t_{\mathrm{L}} \begin{bmatrix} e^{ik_{\mathrm{L}}^{\uparrow} a} & 0 \\ 0 & e^{ik_{\mathrm{L}}^{\downarrow} a} \end{bmatrix}\right] \left|\psi_0^{(\uparrow)}\right\rangle + t_{\mathrm{L}} \left|\psi_1^{(\uparrow)}\right\rangle = \begin{bmatrix} S^{\uparrow} \\ 0 \end{bmatrix} \tag{198}$$

and

$$\left[\mathbb{1}_2\epsilon - h_{\mathrm{L}} + t_{\mathrm{L}} \begin{bmatrix} e^{ik_{\mathrm{L}}^{\uparrow} a} & 0 \\ 0 & e^{ik_{\mathrm{L}}^{\downarrow} a} \end{bmatrix}\right] \left|\psi_0^{(\downarrow)}\right\rangle + t_{\mathrm{L}} \left|\psi_1^{(\downarrow)}\right\rangle = \begin{bmatrix} 0 \\ S^{\downarrow} \end{bmatrix} \tag{199}$$

and for the general case of an arbitrary direction of the spin-polarization, the equation at the outermost node to the left reads

$$\left[\mathbb{1}_2\epsilon - h_{\mathrm{L}} - \Sigma_{\mathrm{L}}^R\right]\Psi_0 + t_{\mathrm{L}}\Psi_1 = R(-\boldsymbol{m}_{\mathrm{L}}) \cdot \begin{bmatrix} S^{\uparrow} & 0 \\ 0 & S^{\downarrow} \end{bmatrix} \tag{200}$$

with the self-energy being

$$\Sigma_{\mathrm{L}}^R = R(-\boldsymbol{m}_{\mathrm{R}}) \cdot \begin{bmatrix} -t_{\mathrm{L}} e^{ik_{\mathrm{L}}^{\uparrow} a} & 0 \\ 0 & -t_{\mathrm{L}} e^{ik_{\mathrm{L}}^{\downarrow} a} \end{bmatrix} \cdot R^{\dagger}(-\boldsymbol{m}_{\mathrm{L}}) \tag{201}$$

such that the in-scattering function is

$$\Sigma_{\mathrm{L}}^{\mathrm{in}} = i f_{\mathrm{L}}(\epsilon)\left(\Sigma_{\mathrm{L}}^R - \Sigma_{\mathrm{L}}^{R^{\dagger}}\right) = 2\pi a R(-\boldsymbol{m}_{\mathrm{L}}) \cdot \begin{bmatrix} |S^{\uparrow}|^2 & 0 \\ 0 & |S^{\downarrow}|^2 \end{bmatrix} \cdot R(-\boldsymbol{m}_{\mathrm{L}}). \tag{202}$$

The source terms can still be obtained from equation (124), but since the spin states are no longer degenerated, they have to be obtained with a spin-dependent wavenumber and spin-dependent amplitude of the entering wave function. Note that when we derived (124), we did already use the density of states associated with a single spin direction.

Non-magnetic leads can be treated as a special case of (197) and (201) with equal wavenumber for both spin directions. Since the rotation matrix is unitary, the self-energies will then be the same as (142) and (143) times a 2×2 identity matrix.

6.3 Spin-dependent Green's functions

Just as we did with the device Hamiltonian, we have to change the Green's functions introduced in chapter 5.1 and 5.2 from an $N \times N$ matrix to a $2N \times 2N$ matrix in order to account for the spin-dependence of the posed problem. This means that for every position, the Green's functions have 2×2 matrices as their values. However, the meaning of these matrices might not be very clear right away.

The retarded Green's function G^R is defined by

$$\left[\epsilon \mathbb{1}_{2N} - H(k_\perp) - \Sigma^R(\epsilon, k_\perp)\right] G^R(\epsilon, k_\perp) = \mathbb{1}_{2N} \tag{203}$$

with the Hamiltonian H being given by (180) and (181) and with Σ^R being

$$\Sigma^R(\epsilon, k_\perp) = \begin{cases} \Sigma_{\mathrm{L}}^R(\epsilon, k_\perp) & i = j = 0 \\ \Sigma_{\mathrm{R}}^R(\epsilon, k_\perp) & i = j = N-1 \\ 0_{2,2} & \text{else} \end{cases} \tag{204}$$

with the only two non-zero spatial entries being (197) and (201). The wavenumbers along the net-transport direction are

$$k_m^\sigma = \sqrt{\frac{2m_m^*}{\hbar^2}\left(\epsilon - U_m^\sigma\right) - k_\perp^2}. \tag{205}$$

The meaning of the sub-matrix entries of the retarded Green's function

$$G_{ij}^R = \left[\left|g_i^{(\uparrow)}\right\rangle, \left|g_i^{(\downarrow)}\right\rangle\right] = \begin{bmatrix} g_{ij}^{(\uparrow)\uparrow} & g_{ij}^{(\downarrow)\uparrow} \\ g_{ij}^{(\uparrow)\downarrow} & g_{ij}^{(\downarrow)\downarrow} \end{bmatrix} \tag{206}$$

can be inferred by (156) in combination with (198) and (199). The columns of (206) can be thought of as the reaction of the system at position i after an excitation at position j with the spin state indicated by the value in the brackets.

From the self-energies, the broadening matrices are obtained according to

$$\Gamma_{\mathrm{L}}(\epsilon, k_\perp) = i\left(\Sigma_{\mathrm{L}}^R(\epsilon, k_\perp) - \Sigma_{\mathrm{L}}^{R\dagger}(\epsilon, k_\perp)\right) \tag{207}$$

$$\Gamma_{\mathrm{R}}(\epsilon, k_\perp) = i\left(\Sigma_{\mathrm{R}}^R(\epsilon, k_\perp) - \Sigma_{\mathrm{R}}^{R\dagger}(\epsilon, k_\perp)\right). \tag{208}$$

Weighting them with Fermi functions

$$f_{\mathrm{m}}(\epsilon) = \frac{1}{\exp\left\{\beta\left(\epsilon - \mu_{\mathrm{m}}\right)\right\} + 1} \qquad m \in \{\mathrm{L}, \mathrm{R}\} \tag{209}$$

as the occupation functions [75] $f_{\mathrm{L}}(\epsilon)$ and $f_{\mathrm{R}}(\epsilon)$, and using the well-known shorthand $\beta = 1/k_b T$, yields the in-scattering matrix

$$\Sigma^{\mathrm{in}}(\epsilon, k_\perp) = \begin{cases} f_{\mathrm{L}}(\epsilon)\, \Gamma_{\mathrm{L}}(\epsilon, k_\perp) & i = j = 0 \\ f_{\mathrm{R}}(\epsilon)\, \Gamma_{\mathrm{R}}(\epsilon, k_\perp) & i = j = N-1 \\ 0_{2,2} & \text{else} \end{cases} \tag{210}$$

that allows to calculate the non-equilibrium Green's function.

$$G^n(\epsilon, k_\perp) = G^R(\epsilon, k_\perp)\Sigma^{in}(\epsilon, k_\perp)G^A(\epsilon, k_\perp) \tag{211}$$

$$G^n(\epsilon) = \int G^n(\epsilon, k_\perp)\mathrm{d}k_\perp \tag{212}$$

The sub-matrices are again some sort of correlation-matrix

$$G^n_{ij} = 2\pi a \sum_k \left[\left|\psi^{(\uparrow)}_{k,i}\right\rangle \left\langle\psi^{(\uparrow)}_{k,j}\right| + \left|\psi^{(\downarrow)}_{k,i}\right\rangle \left\langle\psi^{(\downarrow)}_{k,j}\right| \right] \tag{213}$$

with the sum being over the electrons entering from the left lead and the right lead. In comparison with (149) we have now explicitly written the sum for the two spin-states entering the problem region. The main diagonal of G^n is proportional to the actual density matrix. It is therefore possible to calculate average values of an observable A from it by the well-known relation

$$\langle A \rangle_{x=x_i} = \frac{1}{2\pi a} \mathrm{tr}\left[G^n_{ii} A\right]. \tag{214}$$

The local probability density is in consequence simply

$$n(x_i) = \frac{1}{2\pi a} \mathrm{tr}\left[G^n_{ii}\right]. \tag{215}$$

The off-diagonal elements of G^n can be used to compute the current density, as argued in chapter 5.3 [25].

$$j_e(x_p) = \int \frac{e t_p}{i 2\pi\hbar} \mathrm{tr}\left[G^n_{p,p+1} - G^n_{p+1,p}\right] \mathrm{d}\epsilon \tag{216}$$

Only states with energies that are lying closely around the region between the chemical potentials $\mu_{\mathrm{L}} = V_b/2$ and $\mu_{\mathrm{R}} = -V_b/2$ can contribute to the current. The shift between occupied and unoccupied states is softened by β, so that one should not only integrate the energies between μ_{L} and μ_{R} but instead on an interval broader by a few $k_B T$. The bias voltage V_b applied to the magnetic tunnel junction relates to the shift between the chemical potentials by $eV_b = \mu_R - \mu_L$.

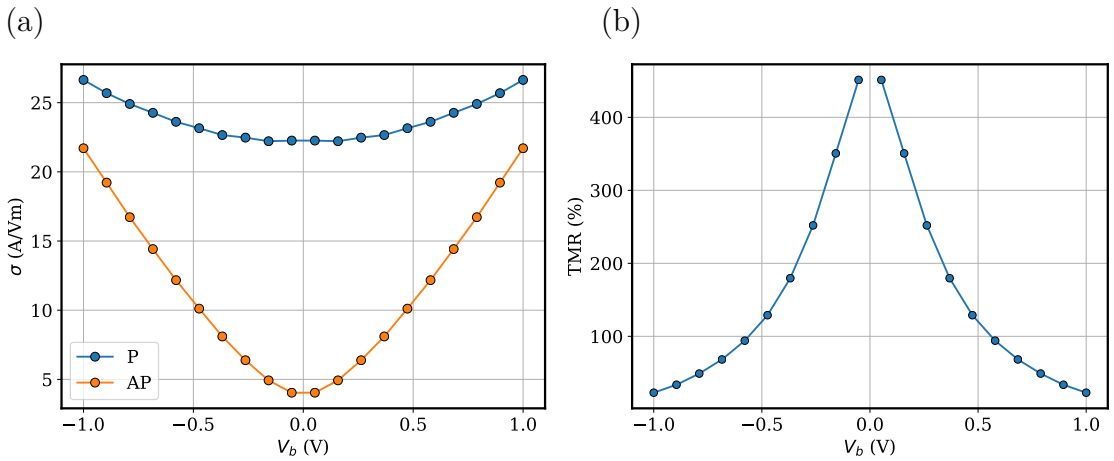

Figure 11: Voltage dependence of the (a) conductivity and (b) TMR ratio of a symmetric junction. The barrier has a length of $L_B = 0.7$ nm and its height is $U_B = 1.77$ eV. The potentials in the semi-infinite ferromagnetic leads are $U^{\uparrow} = -1.9$ eV and $U^{\downarrow} = -0.1$ eV and the effective mass is $m^* = 0.7\, m_e$.

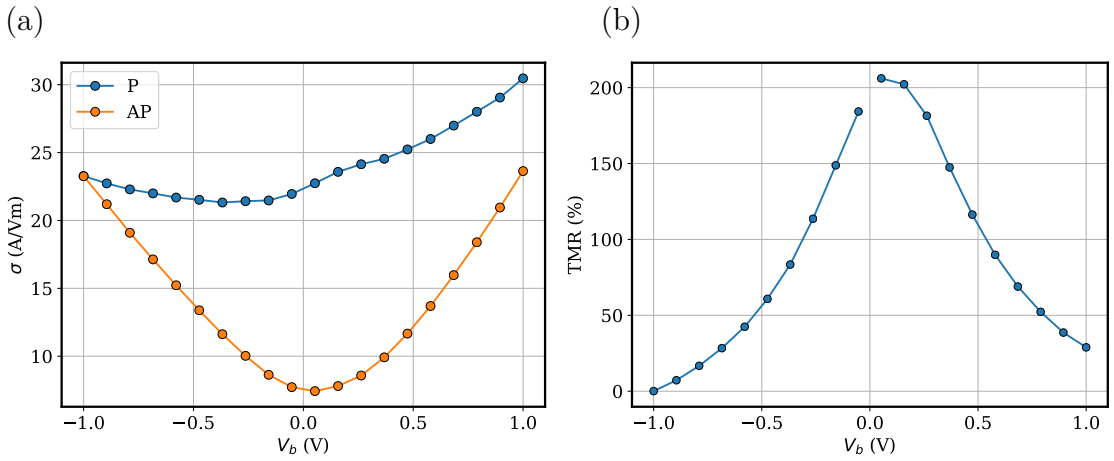

Figure 12: Voltage dependence of the (a) conductivity and (b) TMR ratio of an asymmetric junction. The barrier has a length of $L_B = 0.7$ nm and its height is $U_B = 1.77$ eV. The potentials in the left (right) ferromagnetic lead are $U^{\uparrow} = -1.6$ eV ($U^{\uparrow} = -3.2$ eV) and $U^{\downarrow} = -0.1$ eV ($U^{\downarrow} = -0.25$ eV). The effective mass is $m^* = 0.7\, m_e$.

The current density (216) can be used to calculate the dependence of the conductivity of the magnetic tunnel junction on the bias voltage and the angle between the magnetization $\boldsymbol{m}_{\mathrm{FM1}}$ and $\boldsymbol{m}_{\mathrm{FM2}}$ in the two ferromagnetic leads.

If the same magnetic material, modeled by the set of parameters $U^{\uparrow}$, $U^{\downarrow}$ and m^*, is used for both ferromagnetic layers and if both layers are of the same thickness or modeled semi-infinite, the MTJ is labeled symmetric. For a symmetric MTJ, the voltage dependence of the conductivity is also symmetric, which can be seen in figure 11(a) for the parallel and antiparallel configuration of $\boldsymbol{m}_{\mathrm{FM1}}$ and $\boldsymbol{m}_{\mathrm{FM2}}$. This implies that the TMR dependence on the bias voltage, which is shown in figure 11(b), is also symmetric. The general form of both is consistent with experimental findings [76–78]. Breaking the symmetry of the parameters used to model the MTJ also introduces an asymmetry to the conductivity and the TMR ratio, which can be seen for an exemplary set of parameters in figure 12. This asymmetry is also seen in experiments [79] and might even change the sign of the TMR ratio [80].

The angular dependence of the conductivity is depicted in figure 13 with the data points being values computed for different orientations of $\boldsymbol{m}_{\mathrm{FM2}}$ relative to $\boldsymbol{m}_{\mathrm{FM1}}$ while the lines are obtained from only the parallel and antiparallel conductivity [81] according to

$$\sigma(\theta) = \sigma_{\mathrm{P}} \cos^2(\theta/2) + \sigma_{\mathrm{AP}} \sin^2(\theta/2) \tag{217}$$

which is equivalent to a TMR of the form

$$\mathrm{TMR}(\theta) = \frac{\Delta\sigma\,(1 - \cos(\theta))}{\overline{\sigma} + \Delta\sigma\cos(\theta)} \tag{218}$$

with $\overline{\sigma} = (\sigma_{\mathrm{P}} + \sigma_{\mathrm{AP}})/2$ and $\Delta\sigma = (\sigma_{\mathrm{P}} - \sigma_{\mathrm{AP}})/2$.

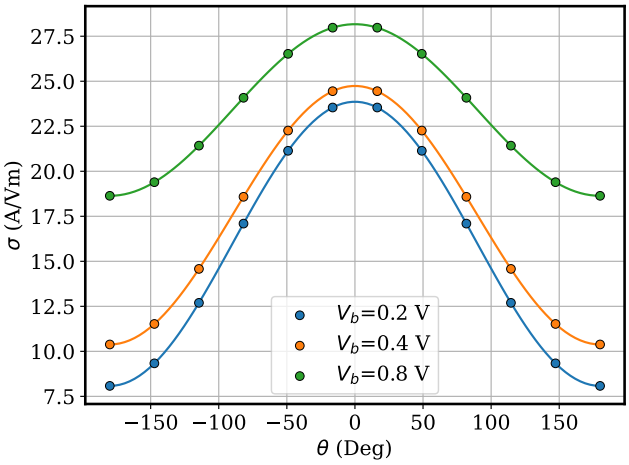

Figure 13: The angular dependence of the asymmetric tunnel junction from figure 12, calculated at different values of the bias voltage from the model (217) (solid lines) and directly from (216) (data points).

6.4 Spin-accumulation, spin-currents and torque

The fact that the main diagonal entries of the non-equilibrium Green's function are the local density matrices allows us to calculate the spin-accumulation $\boldsymbol{s}$ from them in an uncomplicated manner. The observables corresponding to the components of the spin-accumulation, which describes angular momentum rather than spin, are the Pauli matrices times the Bohr magneton μ_B. Thus, the spin-accumulation components are [23]

$$s_k(x_i) = -\frac{\mu_B}{2\pi a} \int \mathrm{tr}\left[G^n_{ii}(\epsilon) \cdot \sigma_k\right] \mathrm{d}\epsilon. \tag{219}$$

The spin-accumulation is often described as the local change in magnetic moment due to an applied current [49] and it is therefore reasonable to assume that the spin-accumulation is just the average value of the angular momentum observables integrated over all energies that contribute to the charge transport (216).
The spin-accumulation calculated with the described method for a symmetric tunnel junction with ferromagnetic leads to which a bias voltage of -0.5 V is applied is shown in figure 14(a). For these calculations, a barrier of height $U_\mathrm{B} = 1.7$ eV and of length $L_\mathrm{B} = 0.8$ nm was assumed, connected to ferromagnetic materials with $U^\uparrow = -2.4$ eV and $U^\downarrow = -0.1$ eV. The effective mass is $m^*_\mathrm{B} = 0.4\, m_e$ within the barrier region and $m^*_\mathrm{FM} = 0.8\, m_e$ in the ferromagnetic material.

In chapter 3.5, we already gave meaning to the components of the spin-accumulation (69) and (69) by linking them to the fieldlike and dampinglike torque terms. These components are plotted in figure 14(b). In both subplots, the electrons are injected from the left and the spin-accumulation appears larger on this side of the insulator. However, the components of the spin-accumulation that can contribute to a torque acting on the local magnetization are larger in the right lead. This is not very surprising. On one hand, one would expect the accumulation to stack up at the FM1/B interface due to a higher chance to reflect back than to tunnel through in the opposing lead. On the other hand, one would also expect that more of the angular momentum that was polarized by FM1 makes it into FM2 than what is reflected back from the B/FM2 interface into the left lead.
All the reduction in the oscillation of the spin-accumulation with further distance of the interfaces is the result of some form of superposition of waves getting out of step with each other, but only the decay of the fieldlike and dampinglike spin-accumulation in the right lead, which is the lead the angular momentum was transported to, is the result of the spin dephasing effect discussed in chapter 2.1.

From (219), the torque exerted on the local magnetization can be computed according to equation (65). The coupling constant is the coupling energy between

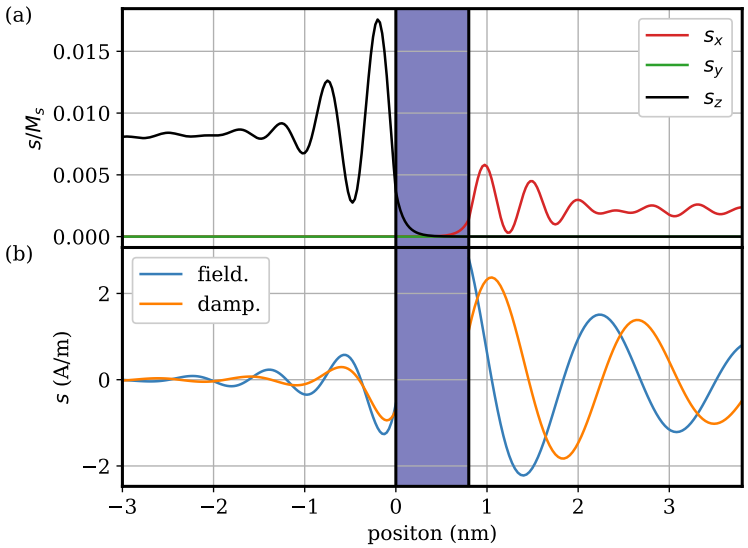

Figure 14: Spatial dependence of the spin accumulation in a magnetic tunnel junction for $\boldsymbol{m}_{\mathrm{FM1}} = \hat{\boldsymbol{z}}$ and $\boldsymbol{m}_{\mathrm{FM2}} = \hat{\boldsymbol{x}}$ at $V_b = -0.5$ V. The barrier region is marked in blue and is modeled by the parameters $U_{\mathrm{B}} = 1.7$ eV and $m^*_{\mathrm{B}} = 0.4\, m_e$. The parameters in the ferromagnetic materials are $U^{\uparrow} = -2.4$ eV, $U^{\downarrow} = -0.1$ eV and $m^*_{\mathrm{FM}} = 0.8\, m_e$. (a) The spin-accumulation is largely directed along the local magnetization direction. Electron flow is from the left to the right, leading to a larger magnitude of the spin-density in the left lead. (b) The components perpendicular to the local magnetization are however larger in the right lead since they do not arise solely from reflection. There values were obtained by projecting the spin-accumulation from equation (219) according to (69) and (70). The polarization vector is chosen according to (48).

the s-electrons and the d-electrons J_i, so that the torque at position x_i is

$$\boldsymbol{T}_i = -\frac{J_i}{\hbar M_s} \boldsymbol{m}_i \times \boldsymbol{s}_i. \tag{220}$$

There is another method of calculating the torque but since it involves the spin-current flowing through the device, we will have to calculate this property first. Its angular momentum components at position p are computed similar to the current density (216) [82].

$$Q_k(x_p) = \int \frac{i\mu_B t_p}{2\pi\hbar} \mathrm{tr}\left[\left(G^n_{p,p+1} - G^n_{p+1,p}\right) \cdot \sigma_k\right] \mathrm{d}\epsilon \tag{221}$$

The static source equation (54) for the spin-accumulation without spin-flip scat-

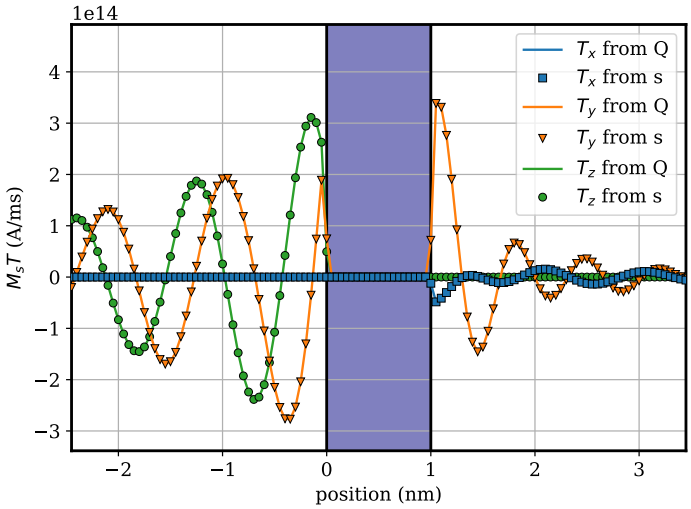

Figure 15: Equivalence of the spin-transfer torque for $\boldsymbol{m}_{\mathrm{FM1}} = \hat{\boldsymbol{x}}$ and $\boldsymbol{m}_{\mathrm{FM2}} = \hat{\boldsymbol{z}}$, calculated from the spin-accumulation according to equation (220) and the spin-current according to equation (224). The barrier (blue region) is of length $L_B = 1$ nm and its height is $U_B = 0.93$ eV. The junction is symmetric and the spin-dependent potentials are $U^{\uparrow} = -2.25$ eV and $U^{\downarrow} = -0.1$ eV with the effective mass being equal to m_e. The applied bias voltage is $V_b = 0.3$ V.

tering i.e. in the limit of $\tau_{\mathrm{sf}} \to \infty$ can be used to relate the torque (65) with the gradient of the spin-current. For a transversally homogeneous spin-accumulation, the above assumptions result in

$$\frac{\partial \boldsymbol{Q}}{\partial x} = -J \frac{\boldsymbol{s} \times \boldsymbol{m}}{\hbar} \tag{222}$$

and therefore, the torque (65) is

$$\boldsymbol{T} = -\frac{1}{M_s} \frac{\partial \boldsymbol{Q}}{\partial x} \tag{223}$$

or, for our numerical assessment,

$$\boldsymbol{T}_i = \frac{1}{a M_s} \left[\boldsymbol{Q}_i - \boldsymbol{Q}_{i+1} \right]. \tag{224}$$

The equivalence between the torque calculated from the spin-accumulation (220) i.e. the main diagonal of G^n and the torque calculated from the spin-current (224) i.e. the off-diagonal of G^n was shown and investigated in reference [82] and can be seen in figure 15.

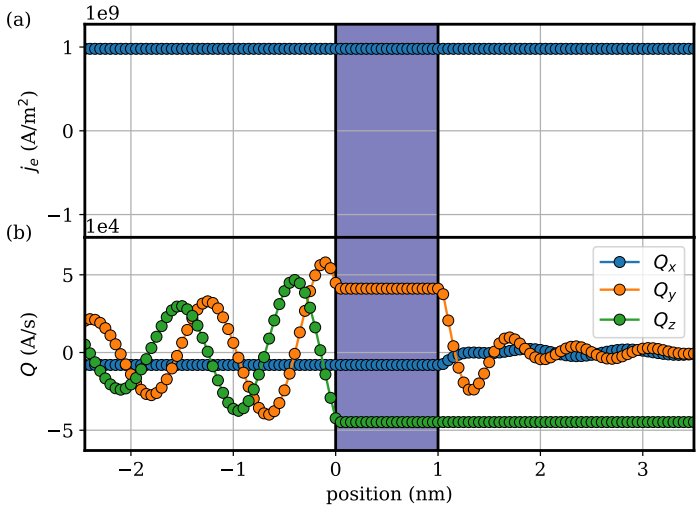

Figure 16: Spatial dependence of (a) the charge-current and (b) the spin-current. Within the barrier region (shaded in blue), all currents are constant. In the semi-infinite ferromagnetic layers, the spin-current component parallel to the local magnetization ($\boldsymbol{m}_{\mathrm{FM2}} = \hat{\boldsymbol{x}}$ and $\boldsymbol{m}_{\mathrm{FM2}} = \hat{\boldsymbol{z}}$) are also constant. The same parameters as in figure 15 were used.

The spin-current that was used to compute the torque in figure 15 is depicted in figure 16 together with the charge current. Note how the charge current in figure 16(a) is constant while the spin-current components are only constant within the barrier region and for components aligned with the local magnetization, which is consistent with the fact that the torque acts only perpendicular to the magnetization direction.

We have already argued before that in the context of this work, the layer thicknesses of the magnetic materials will be small enough to justify the assumption of a homogeneous magnetization within a layer. We have also pointed out that the finite-element mesh used for the simulation of the magnetization dynamics has an average element length around an order of magnitude longer than the spacing a of the finite differences mesh on which the Green's functions are solved. To use the torque in the magnetization dynamics simulations, we therefore need an averaged value of (220).

If the length of the material is L_m, then the average torque acting on the magnetization within this layer is

$$\langle \boldsymbol{T} \rangle_{\Omega_m} = \frac{1}{L_m} \int_{\Omega_m} \boldsymbol{T}(x) \mathrm{d}x. \tag{225}$$

If the layer is sampled by N_m nodes, this average can be approximated by

$$\langle \boldsymbol{T} \rangle_{\Omega_m} \approx -\frac{J_m}{\hbar M_s} \boldsymbol{m}_m \times \frac{1}{N_m} \sum\nolimits_i \boldsymbol{s}_i \tag{226}$$

which assumes a constant magnetization and coupling constant. Similarly, the average torque can be obtained from the spin-current instead. Summing up all torques calculated according to (224) between two positions x_a and x_b simplifies to the difference of the spin-currents at these positions, thus resulting in [24].

$$\langle \boldsymbol{T} \rangle_{x_a \leq x \leq x_b} = \frac{1}{x_b - x_a} \int_{x_a}^{x_b} \boldsymbol{T}(x) \mathrm{d}x \tag{227}$$

$$= \frac{\boldsymbol{Q}(x_a) - \boldsymbol{Q}(x_b)}{M_s \left(x_b - x_a\right)}. \tag{228}$$

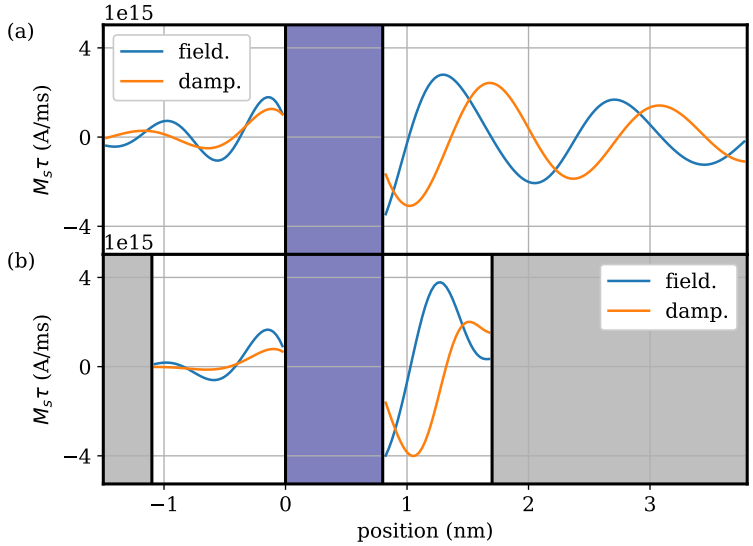

Figure 17: Comparison of the torque calculated for (a) a three domain Hamiltonian with semi-infinite ferromagnetic leads and (b) a five domain Hamiltonian with ferromagnetic domains of finite length, contacted by semi-infinite non-magnetic leads. Since there is no precession of the spin in non-magnetic leads and the first derivative of the wave function has to be continuous, the change of the torque components is zero at the FM/NM interfaces. The used parameters are $U_\mathrm{B} = 2.1$ eV and $m^*_\mathrm{B} = 0.4\, m_e$ in the barrier region, $U^\uparrow = -2.4$ eV, $U^\downarrow = -0.2$ eV and $m^*_\mathrm{FM} = 0.8\, m_e$ in the ferromagnetic materials and $U_\mathrm{NM} = -3$ eV and $m^*_\mathrm{NM} = m_e$ in the non-magnetic leads.

One could go about calculating the average torques for magnetic layers of finite length in two different ways. The first would be to assume semi-infinite magnetic leads in the context of solving the Schrödinger equation with spin-dependent open boundary conditions and to average the torque starting from the barrier interfaces over the length of the leads [24]. Another possibility is to model the ferromagnetic leads to be of finite length to begin with in the Hamiltonian, just like it is illustrated in figure 10. Figure 17 contrasts the two methods. Figure 17(a) shows the spatial dependence of the fieldlike and dampinglike torque component for semi-infinite magnetic leads while the torques in subplot (b) are obtained from a five-domain Hamiltonian. The latter method does include effects from the interfaces between the ferromagnetic materials and the semi-infinite non-magnetic leads.

Figures 18 and 19 contain data on the voltage dependence of the two torque terms obtained for a three-domain model and a five-domain model for two sets of parameters, showing no significant qualitative difference, but they do show a quantitative difference. It should be noted that in the context of the discussed algorithm, including the two additional interfaces comes with only limited additional computational cost since the semi-infinite non-magnetic leads can be sampled with only a few sample points.

The field components in figures 18 and 19 were computed for $\boldsymbol{m}_{\mathrm{FM1}}$ and $\boldsymbol{m}_{\mathrm{FM2}}$ being orthogonal to each other. The fields can therefore be related to the torque coefficients directly.

$$H_{\mathrm{fl}}\left(\theta = 90^{\circ}\right) = \frac{1}{\gamma}\tau_{\mathrm{fl}} \tag{229}$$

$$H_{\mathrm{dl}}\left(\theta = 90^{\circ}\right) = \frac{1}{\gamma}\tau_{\mathrm{dl}} \tag{230}$$

It is noteworthy that while the field components are dependent on the angle θ between the magnetization directions, the torque coefficients are constant, which can be seen in figure 20.

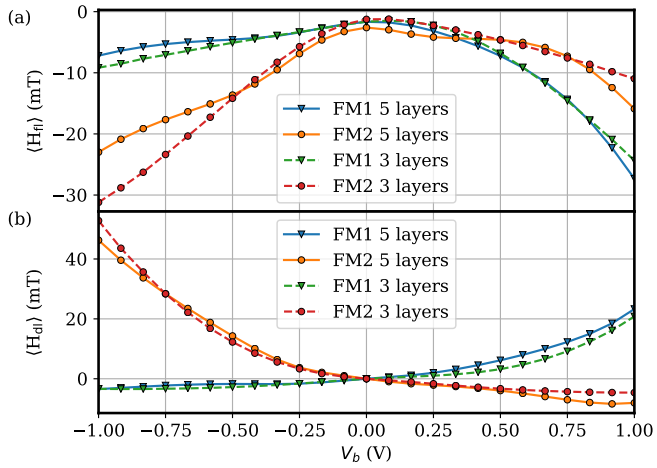

Figure 18: Voltage dependence of the fields corresponding to (a) the fieldlike torque and (b) the dampinglike torque for $\boldsymbol{m}_{\mathrm{FM1}} \perp \boldsymbol{m}_{\mathrm{FM2}}$. The barrier length and height are $L_{\mathrm{B}} = 0.8$ nm and $U_{\mathrm{B}} = 1.7$ eV. The potentials are $U^{\uparrow} = -2.4$ eV and $U^{\downarrow} = -0.2$ eV in ferromagnetic layers and $U_{\mathrm{NM}} = -3$ eV within the non-magnetic leads. The effective mass is $m_{\mathrm{B}}^{*} = 0.4\, m_e$ in the barrier region and $0.8\, m_e$ everywhere else. In the five layer model, the length of the ferromagnetic layers are $L_{\mathrm{FM1}} = 1.1$ nm and $L_{\mathrm{FM2}} = 0.9$ nm. In the three layer model, the fields are averaged over the same lengths.

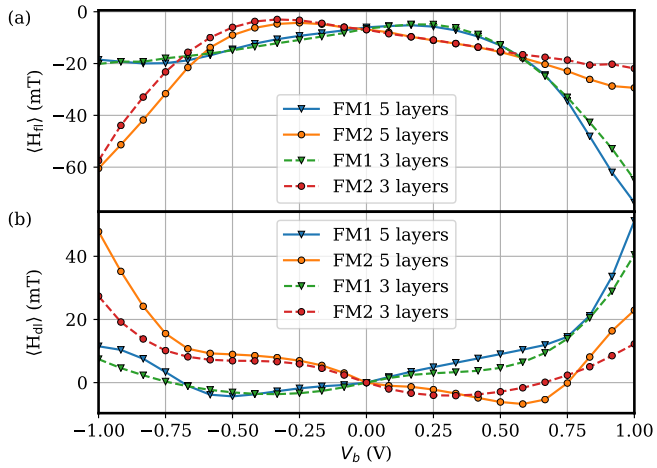

Figure 19: As in figure 18, but for a stack that exhibits a second zero-crossing of the dampinglike torque. The layer thicknesses are $L_{\mathrm{B}} = 0.8$ nm, $L_{\mathrm{FM1}} = 1.1$ nm and $L_{\mathrm{FM2}} = 1.2$ nm, the potentials are $U_{\mathrm{B}} = 0.9$ eV, $U^{\uparrow} = -2.5$ eV, $U^{\downarrow} = -0.2$ eV and $U_{\mathrm{NM}} = -3$ eV. The effective mass is $m_{\mathrm{B}}^{*} = 0.6\, m_e$ in the barrier region and $0.9\, m_e$ everywhere else.

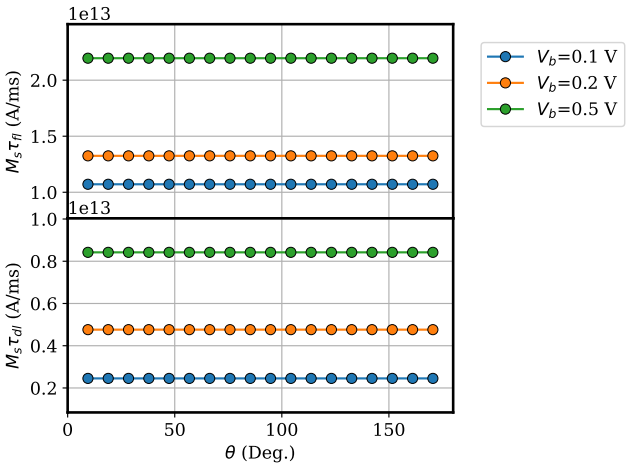

Figure 20: For magnetic tunnel junctions described in the coherent transport regime, the torque coefficients of the STT do not depend on the angle between the magnetizations. The junction is modeled to be connecting semi-infinite ferromagnetic leads and the parameters used are $U_{\mathrm{B}} = 1.9$ eV, $U^{\uparrow} = -2.4$ eV, $U^{\uparrow} = -0.2$ eV and $m^* = m_e$.

6.5 Quadratic behavior of dampinglike torque component

The STT calculated in the ballistic regime from a free electron model differs quite substantially from the torque obtained from the SDD model for the diffusive regime in GMR spin-valve structures. According to (50) and (51), the torque scales linearly with the applied current in context of the SDD model, but this is not the case for the torques in STT-driven MTJs. Instead, both torque components behave similar to quadratic functions of the bias voltage. This can even include an additional change of sign on the positive voltage branch, just like it occurs in figure 19(b). The quadratic nature of the torque terms was studied extensively in various theoretical works on the subject [23–26, 83] but was also observed experimentally [27, 84].

In the referenced theoretical works, the torque is often computed not as an average over some layer thickness but instead as a total over the whole semi-infinite ferromagnetic leads. This is possible since the torque, which is proportional to the change of the spin-current, vanishes for long enough distances from the barrier and so the total torque is proportional only to the spin-current at the interfaces. The same argument could be made when the average torque is computed via (228) for long enough leads. Figure 21 shows the voltage dependence of the spin-currents at the I/FM2-interface for the same sets of parameters that were used to calculate the

data in figures 18 and 19. The voltage dependence of the spin-current components that follow the same symmetry as the fieldlike and dampinglike torque are [26]

$$Q_{\mathrm{fl}}(V_b) = a_0 + a_1 V_b + a_2 V_b^2 \tag{231}$$

$$Q_{\mathrm{dl}}(V_b) = b_1 V_b + b_2 V_b^2 \tag{232}$$

In order to understand the quadratic nature of the dampinglike component, we will follow the argumentation provided by Theodonis et al. in reference [23] and the reader should refer to this work for a more detailed and general explanation.

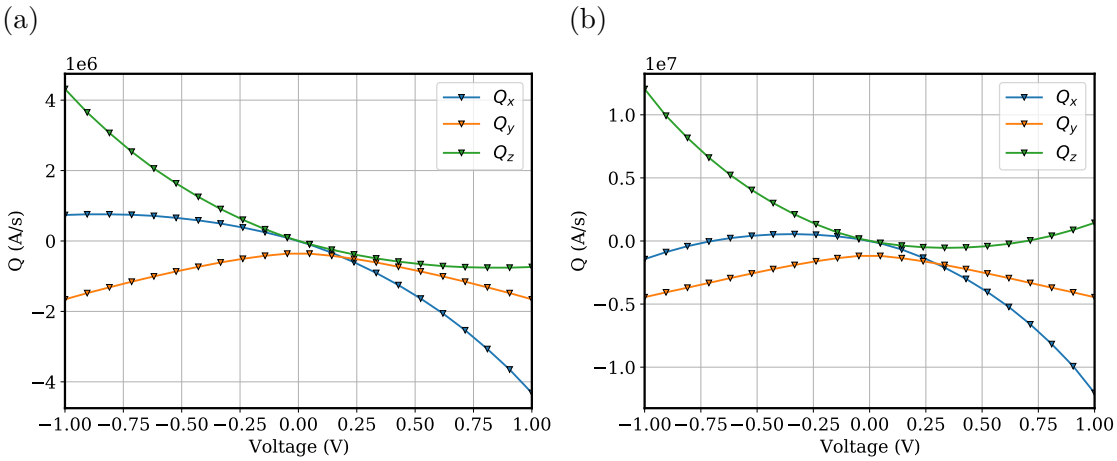

Figure 21: The bias voltage dependence of the spin-current components within the barrier region for the three layer stacks characterized in figures 18 and 19 are the subplots (a) and (b), respectively. Since the magnetizations are $\boldsymbol{m}_{\mathrm{FM1}} = \hat{\boldsymbol{z}}$ and $\boldsymbol{m}_{\mathrm{FM2}} = \hat{\boldsymbol{x}}$, the Q_y component determines the fieldlike torque for both layers. Q_x is proportional to the total torque in FM1 and Q_z to the total torque in FM2 with the symmetry $Q_x(V_b) = -Q_z(-V_b)$ reflecting the symmetry of the structure and the direction of rotation.

Let's consider a symmetric junction with semi-infinite magnetic leads. The basic idea of Theodonis et al. is that the average torque can be calculated from the spin-current according to (228) and that the spin-dependent conductivities should follow a $\cos^2(\theta/2)$ behavior for spins that do not change their state during transport and $\sin^2(\theta/2)$ for spins that change from spin up to spin down or vice-versa. Arguing that for long enough leads the spin current would vanish at the outer point of (228), they assess that the dampinglike torque component would be proportional to the difference between the only non-zero component of the spin current for the

parallel and antiparallel alignment at the FM/I interface.

$$\tau_{\mathrm{dl}}(V_b) \propto Q_{\mathrm{AP}}(V_b) - Q_{\mathrm{P}}(V_b) \tag{233}$$

In a symmetric junction, it is easy to see from figure 22 that $Q_{\mathrm{P}}(V_b)$ is an odd function of the bias voltage while $Q_{\mathrm{AP}}(V_b)$ is even, meaning that the sign of the spin-current will not change with the polarity of the voltage for the antiparallel configuration while it does change for the parallel alignment. Therefore, the dampinglike torque is expected to be the sum of an even and an odd function of the applied voltage. The argument made about the sign of the spin-currents can be extended to asymmetric functions, but without them being exactly even or uneven functions.

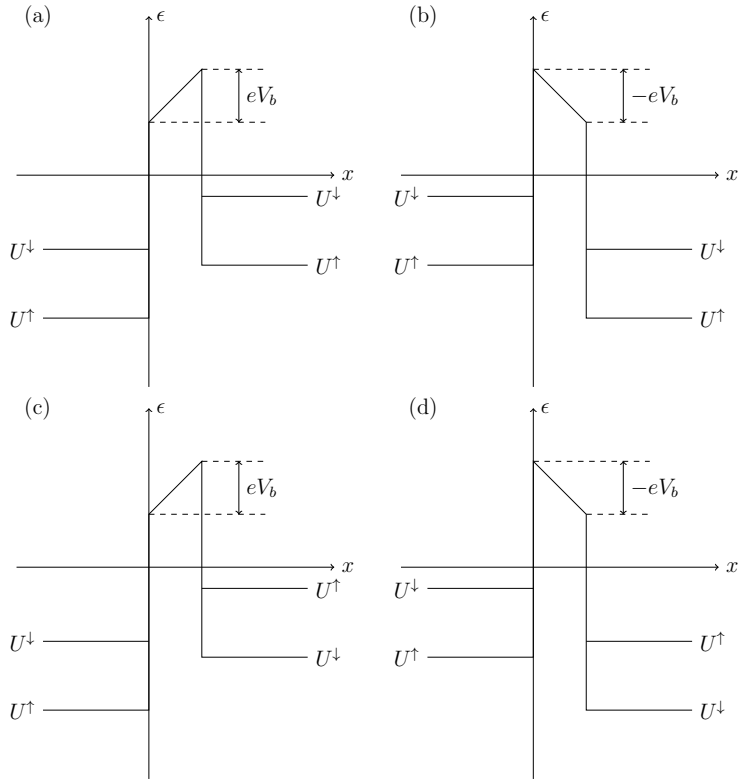

Figure 22: The spin-current through a symmetric tunnel junction in its parallel configuration changes sign when the voltage is reversed, as can be argued from the symmetry of (a) and (b). In the antiparallel configuration, there is only a spatial symmetry if the spin directions are mirrored. This indicates that the spin current does not change sign in the antiparallel case, which can be seen by comparing (c) and (d).

6.6 Interlayer exchange coupling in magnetic tunnel junctions

A noteworthy feature of the fieldlike torque is that it does not vanish when no bias voltage is applied. Instead, it and the associated spin-current component do have an offset value that gives rise to an interlayer coupling. This form of coupling was first derived by Slonczewski from a free electron model in reference [17] and was contrasted to the interlayer exchange coupling for stacks with a conducting spacer layer in reference [85] by Bruno. They found the coupling constant to be following an exponential decay with increasing spacer thickness for an insulating spacer while the exchange constant oscillates for a conducting spacer layer in accordance with the RKKY theory. Measurements of this interlayer coupling show the exponential behavior predicted by theoretical assessments [86].
The exponential behavior of the interlayer coupling constant A_{iec} is reproduced in figure 23(a) for different barrier heights. It is determined from the average fieldlike torque but weighted by the thickness of the ferromagnetic layer in order to compare it with the interlayer exchange (42). Due to the oscillatory nature of the coherent solution of the spin-dependent wave functions, A_{iec} does oscillate with varying thickness of the ferromagnetic lead and becomes constant only for larger thicknesses. This can be seen in figure 23(b).

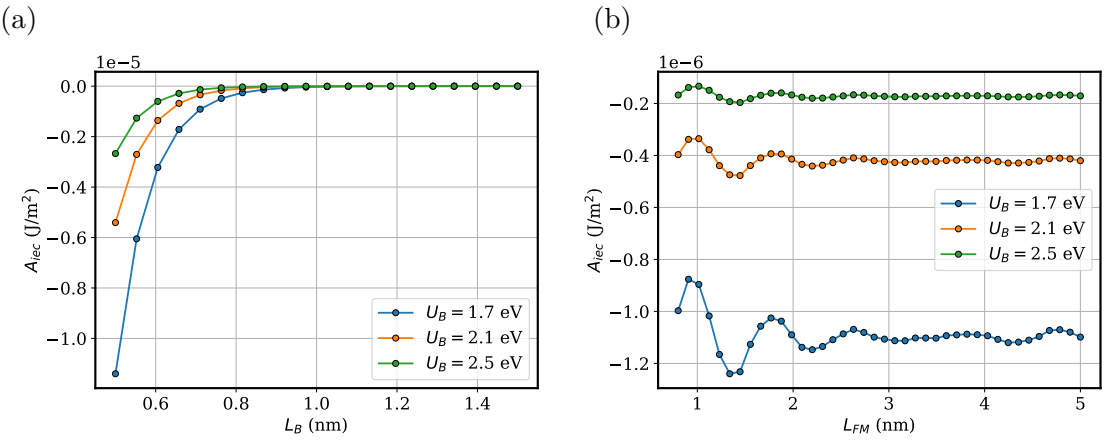

Figure 23: (a) Exponential dependence of the interlayer coupling on the thickness of the barrier region L_B arising from the free-electron model at $V_b = 0$ for different heights of the barrier U_B. (b) Since the interlayer coupling is an interfacial effect, the coupling constant is usually assumed to be independent of the thickness of the ferromagnetic layers. Due to the oscillatory nature of the wave function, this is approximately true only for thick ferromagnetic layers within this model. The parameters are $U^{\uparrow} = -2.4$ eV, $U^{\downarrow} = -0.1$ eV, $m^* = 0.7\, m_e$ and $M_{s,\text{FL}} = 1$ T.

There are other effects leading to a coupling between the ferromagnetic layers in MTJs like the so-called Néel orange-peel effect, that arises from rough surfaces [87], or pinhole coupling [88]. While these effect might be negligible for samples of good quality, others may not. For example, oxygen vacancies, which pose a common defect of MgO layers, were found to be the cause for sharp changes in sign of the coupling constant at small spacer layer thicknesses in reference [89].

6.7 Coupling to magnetization dynamics

We have everything we need to perform self-consistent simulations of magnetization dynamics governed by the Landau-Lifshitz-Gilbert equation (28) with torques obtained for spin-polarized tunnel-currents. For a given set of magnetizations, the Hamiltonian defined by (180) and (181) can be constructed and from it, the non-equilibrium Green's function (212) is calculated via (203) and (211). The torque that acts back on the magnetization can then be obtained either from (226) or (228) and time-integration of (28) yields the set of magnetization for the next time step [30].

It is however easy to see how the matrix inversion in (203) would slow down the time integration of the LLG significantly and an efficient solution strategy is required, as we have already discussed in reference [90].
For a constant bias voltage, there is no need to solve for the non-equilibrium Green's function in every time step. Since the torque coefficients τ_{fl} and τ_{dl} are constant, they can be precomputed and stored so that in each time step, the torques can be constructed via (46) and (47) from them. The same can be done for the components of the spin-accumulation that are associated with the torque terms, (69) and (70), if the solver for the LLG accounts for the torque by implementing the field term (66) instead.

If the voltage changes frequently or even constantly, it might be useful to precompute an entire lookup table of the torque coefficients and to interpolate values between them. The same can be done for simulations in which the charge current density is set instead of the voltage. This comes however with the added difficulty that for a set current, the torque components are no longer constant with respect to θ, requiring a second dimension to the table data.

Self-consistent coupling with the LLG allows to simulate the switching behavior of STT-driven MTJs as demonstrated in figure 24(a). The simulations show the magnetization reversal for a stack with perpendicular anisotropy in both directions for different bias voltages. The potentials are $U_{\mathrm{B}} = 1.7$ eV, $U^{\uparrow} = -2.4$ eV, $U^{\downarrow} = -0.1$ eV and $U_{\mathrm{NM}} = -3$ eV. The effective mass is $m^{*}_{\mathrm{B}} = 0.4\, m_e$ in the barrier region and $0.8\, m_e$ everywhere else. The anisotropy constants are $K_{u,\mathrm{RL}} = 1 \cdot 10^{6}$ J/m^3

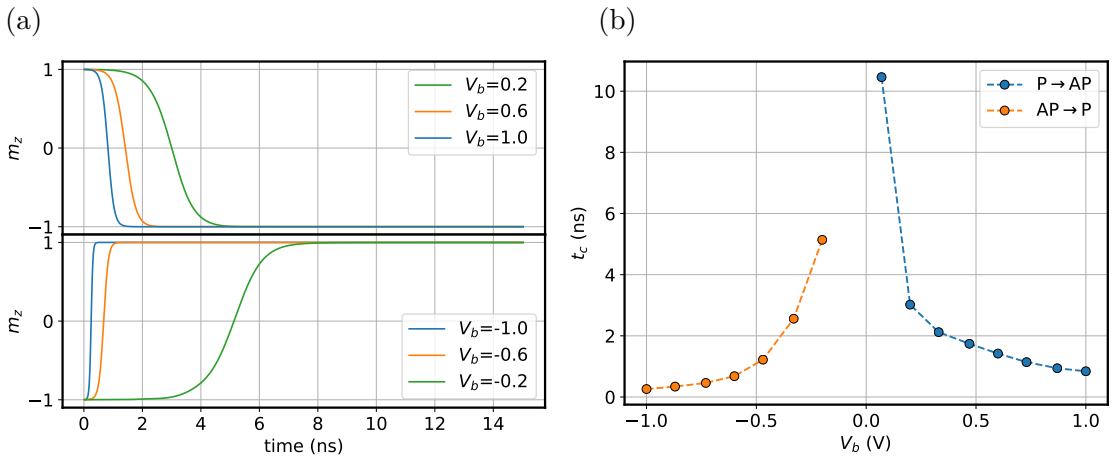

Figure 24: (a) Exemplary switching dynamics of the perpendicular magnetization component for different values of the voltage in the P $\rightarrow$ AP and AP $\rightarrow$ P direction. The reference layer magnetization is pointing in the positive z-direction. The net-flow of electrons is from the reference layer into the free layer if $V_b < 0$. (b) The minimal time required for a successful reversal of the free-layer magnetization. The parameters for the simulations are stated in the text.

and $K_{u,\mathrm{FL}} = 4 \cdot 10^3$ J/m^3, the saturation magnetizations are $M_{s,\mathrm{RL}} = 1.25$ T and $M_{s,\mathrm{FL}} = 1$ T and the Gilbert damping parameter was $\alpha = 0.08$. The exchange constant was set to $A = 2.8 \cdot 10^{-11}$ J/m, meaning that the exchange length is $L_{\mathrm{ex,RL}} = 5.9$ nm in the reference layer and $L_{\mathrm{ex,FL}} = 59$ nm in the free layer, well above the respective layer thicknesses which are $L_{\mathrm{RL}} = 1.1$ nm and $L_{\mathrm{FL}} = 0.9$ nm. The length of the barrier is $L_{\mathrm{B}} = 0.7$ nm.

The minimum time the voltage needs to be applied to the tunnel junction in order to successfully switch the magnetization is called the critical switching time t_c. This is the time of the m_z component passing the unstable equilibrium position between the energy contributions by the anisotropy and the interlayer coupling due to the fieldlike torque at zero voltage $H_{\mathrm{fl}}(V_b = 0)$. If the voltage would be cut i.e. set to zero at any later point, the free layer magnetization would still relax into the desired direction. The voltage dependence of the critical switching time for both the P $\rightarrow$ AP (parallel to antiparallel) and AP $\rightarrow$ P (antiparallel to parallel) switching direction is shown in figure 24(b).

6.8 Back-hopping

Judging from figure 24(b), it might seem reasonable to assume that higher absolute values of the voltage would result in faster switching. The fact that the torque depends linearly on the current flow in the SDD model might only further affirm this thought, but the quadratic nature of (232) suggests that this might not be true for magnetic tunnel junctions. We have discussed in chapter 3.6 how the dampinglike torque is the main driving force behind the magnetization reversal, and so the free electron transport calculations we have presented so far indicate that at some point, the dampinglike torque will have a trend reversal on one voltage branch and eventually will even change its sign. This means not only that the critical switching time would start to increase from a certain voltage on but also that the switching direction would change altogether.

It was suggested [91] that this might be related to the back-hopping effect that occurs in some STT-MRAM cells and leads to an increase in writing error rates at high voltages.
The back-hopping effect was found to occur on either one [31] or both voltage branches [32]. In the original work by Min et al. [32], an experiment was conducted in which a voltage pulse with gradually increasing height was applied to MTJs. After each pulse, the resistance of the device was measured to determine its current state. They found that after successfully switching the free layer at some value of the bias voltage, the magnetization would hop back to its original direction at a higher voltage. From there on out, the device is found to jump back and forth between the high and low resistance state in what occurs to be a random process.

Utilizing a macro-spin model with a dampinglike torque term that scales linearly in the current, computational studies found that such behavior could be attributed to the dynamics of the reference layer, if the STT acting back on it is large enough to overcome its stabilizing energy contributions [92–94]. The basic idea is that the STT acting on one layer would always try to align it in parallel with the other while the STT acting on the second layer would try to achieve an antiparallel configuration. If the stabilizing fields like e.g. the uniaxial anisotropy are large enough to hold the layers in position for a short amount of time but small enough so that the process can take place in principle, this would result in an alternating switching of the magnetic layers that is illustrated in figure 25(a).

In reference [91], Devolder et al. conducted experiments that include time resolved measurements of the resistance to determine whether the back-hopping in STT-MRAM cells stems from the dynamic process described before or if it is linked to the quadratic nature of the dampinglike torque component.
In their study, they found that on the P $\rightarrow$ AP branch of the resistance versus

voltage loops, the device would switch back to a parallel configuration, giving rise to a second hysteresis loop. It was pointed out that the resistance of the parallel state the device enters in this second loop does vary from the resistance of the original P state. Devolder et al. therefore reasoned that this P′ state has to differ from the original P.
Subsequent time resolved measurements for the devices showed that the P′ state can be reached at a fixed voltage starting from the P state in two switching events, P → AP and AP → P′. Between them, the device was found to stay in the AP state for a short time. Additionally, the system was found to relax back into the AP when the current was cut. From these results, it was concluded that the P′ would therefore arise from a switching event in the reference system.
Still, the back-hopping observed by Devolder et al. differs in its manifestation as a second hysteresis loop in the resistance versus voltage measurement from the back and forth switching reported by Min et al. in reference [32] and Oh et al. in reference [31].

Coupled NEGF+LLG simulations allow us to examine both potential origins of the back-hopping effect that were considered by Devolder et al in reference [91]. In contrast to the simulation work carried out in references [92–94], the torque is not assumed to behave according to the diffusive transport regime but is calculated from a free electron model in the purely coherent regime and is therefore not proportional to the current flow through the device.
We will compare the hysteresis of two stacks, that are modeled by the parameters found in tables 1 and 2. Both stacks, A and B, have a perpendicular magnetic anisotropy and a reference layer that is pinned by a bias field, simulating an interlayer exchange coupling to a hard layer. This simplification of the stack geometry is illustrated in figure 25(b). The magnetization of the reference layer is additionally subject to the uniaxial anisotropy, but the interlayer exchange outweighs it so that only the direction indicated by the sign of A_{IEX} is stable.
The crucial difference between the two stacks is the form of the dampinglike torque acting on the free layer, shown in figure 26. Both stacks have a trend reversal of the dampinglike torque on the positive voltage branch, but for stack B, this leads to a change of sign around $V_b = 0.75$ V. This leads to distinctly different hysteresis loops, depicted in figure 27.
The substantially larger dampinglike torque of stack A can overcome the pinning of the RKKY coupled reference layer, resulting in the cyclic switching process described earlier. This process goes on for the duration of the applied writing pulse, which was $t_V = 8$ ns for stack A. After this time, the voltage is cut and the system can relax for $t_r = 8$ ns. The free layer relaxes either into the P or AP direction, depending on its state when the voltage was cut. Note that P and AP are indeed well-defined and coincide with the low and high resistance states

ID	stack	$U_\uparrow$ (eV)	$U_\downarrow$ (eV)	U_B (eV)	m^*_B/m_e	m^*_C/m_e
A	FM(0.9)/I(0.7)/FM(1.1)	-2.2	-0.1	1.4	0.4	0.8
B	FM(1.1)/I(0.8)/FM(1.2)	-2.5	-0.2	0.9	0.6	0.9

Table 1: Parameters of the stacks required to obtain the spin accumulation from the NEGF formalism.

ID	A_IEX (J/m^2)	$J_{s,\mathrm{RL}}$ (T)	$J_{s,\mathrm{FL}}$ (T)	$K_{u,\mathrm{RL}}$ (J/m^3)	$K_{u,\mathrm{FL}}$ (J/m^3)
A	$5.5 \cdot 10^{-4}$	1.3	1	$1.2 \cdot 10^4$	$8 \cdot 10^4$
B	$5.5 \cdot 10^{-4}$	1.24	1	$1.6 \cdot 10^4$	$8 \cdot 10^4$

Table 2: Parameters of the stacks used for the time integration of equation (28).

of the tunnel junction since the reference layer will always return into its original configuration due to the RKKY coupling. The magnetization of the free layer is sampled after the relaxation time has passed. The height of the writing pulses is first increased from step to step before it is sequentially decreased back to the starting value. The resulting hysteresis in figure 27(a) showing the back-hopping phenomenon as a randomly alternating series of P and AP, reminiscent to references [32] and [31]. Applying the same measurement procedure to stack B with $t_V = 10$ ns and $t_r = 12$ ns yields a hysteresis that looks very different, exhibiting no dynamic back-hopping but a second loop as a result of the additional zero-crossing of the dampinglike torque. The loop depicted in figure 27(b) resembles therefore the resistance versus voltage loops presented in reference [91]. However, this resemblance might only be superficial since the additional switching in our simulations remains stable when the voltage is cut.

If the writing process of an STT-MRAM cell was unsuccessful because of the quadratic form of the dampinglike torque i.e. if it were to behave similar to stack B, then the writing would fail certainly for high currents. When the back-hopping occurs as a dynamic process as in stack A, the switching probability would decrease but would not be zero since the state in which the device ends up in after the voltage is cut depends on the length of the writing pulse. This is illustrated in figure 28, where the dynamics of both the free layer and the reference layer are shown. Gray areas mark the time intervals in which cutting the voltage instantaneously would yield a successful P $\rightarrow$ AP writing process if the reference and free layer were completely uncoupled.
Figure 29 shows the voltage dependence of the estimated switching probability for the P $\rightarrow$ AP direction. The shown probabilities are computed by convolution of

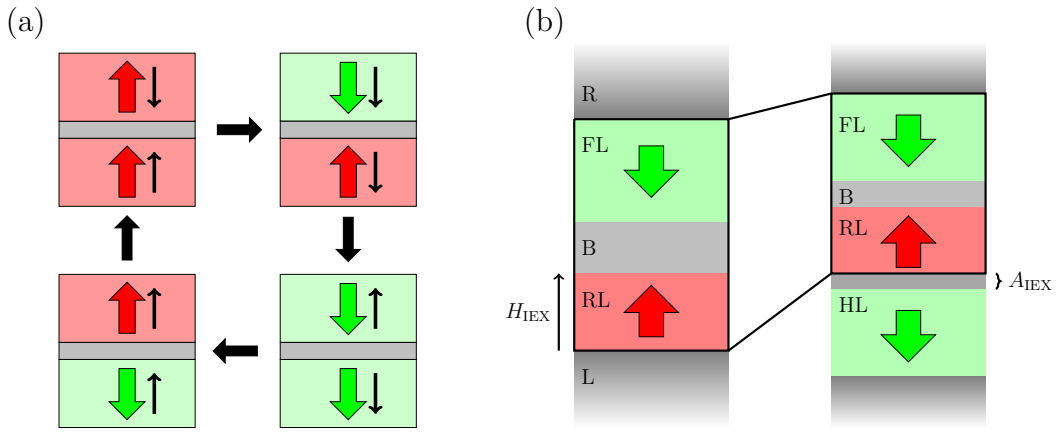

Figure 25: (a) Cyclic process of back-hopping due to switching of the reference layer. The large arrows indicate the magnetization of the layers while the small arrows indicate the energetically preferred direction due to STT. (b) The simulations account for the reference layer (RL) being anti-ferromagnetically coupled to a static hard layer (HL) only by introducing a bias exchange field within the reference layer. In neither the transport calculations nor the magnetization dynamics calculations the hard layer is modeled explicitly.

the success function

$$s(x) = \begin{cases} 1 & m_{z,\mathrm{FL}}(x) > 0 \\ 0 & \text{else} \end{cases} \tag{234}$$

with a probability distribution function for the writing pulse length. The function (234) determines whether the current magnetization would relax into the desired direction if it was not coupled to $\boldsymbol{m}_{\mathrm{RL}}$ and coincides with the regions marked in gray in figure 28. It should be pointed out that $\boldsymbol{m}_{\mathrm{RL}}$ and $\boldsymbol{m}_{\mathrm{FL}}$ are coupled even at zero bias, as we have discussed in chapter 6.6, and the switching probabilities in figure 29 can therefore only be understand as estimates. However, a connection between longer pre-switching times of the reference layer with higher success probabilities can be made by comparing figure 28 and figure 29.

To conclude the discussion of the different switching behaviors found for stack A and B, we would like to point out that the destabilization of the reference layer and the dynamic counter switching can occur for both polarities of the voltage although one branch might be preferable due to the monotonic increase of the dampinglike torque on it. This contrasts the dynamic effect further to the back switching in stack B, which can only occur on the voltage branch that holds the sign-reversal of the dampinglike torque.

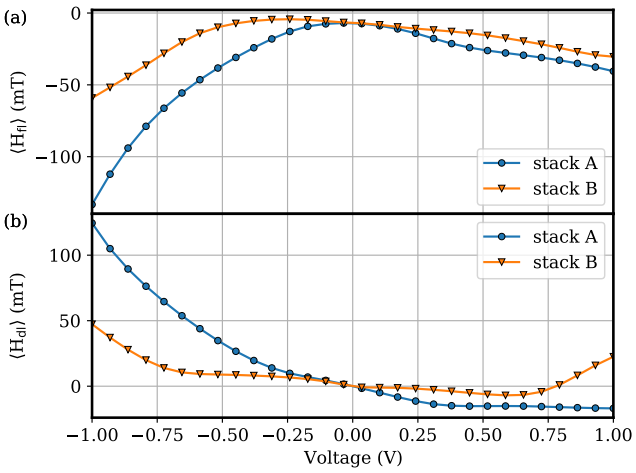

Figure 26: Average values of H_{fl} and H_{dl} acting on the magnetization of the free layer for $\boldsymbol{m}_{\mathrm{RL}} \perp \boldsymbol{m}_{\mathrm{FL}}$. For stack B, the dampinglike component has an additional sign reversal around 0.75 V.

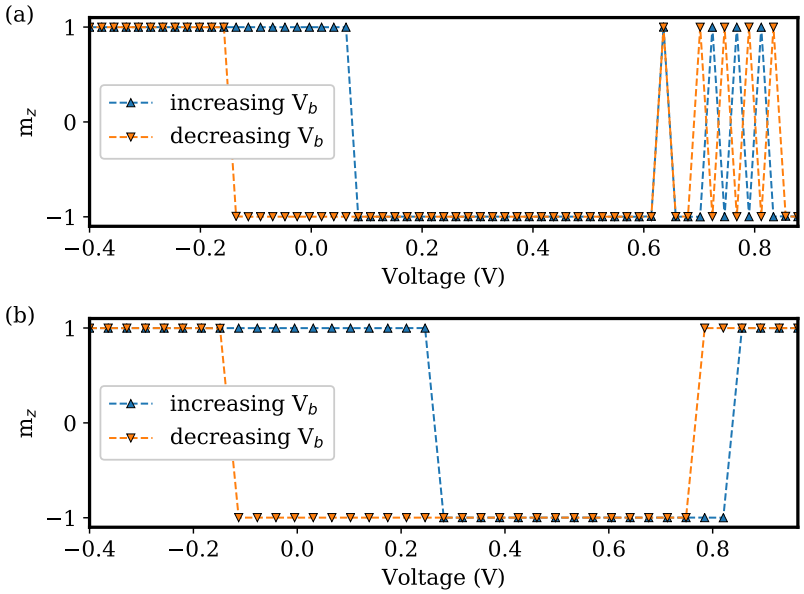

Figure 27: Simulation of the STT-induced switching behavior of (a) stack A, including back-hopping that appears as a dynamic effect, and (b) stack B, showing a second hysteresis loop. The free layer out-of-plane component was sampled after first applying the indicated voltage for t_V and then letting the system relax for t_r. The equilibrium direction of the reference layer is $\boldsymbol{m}_{\mathrm{RL}} = \hat{\boldsymbol{z}}$.

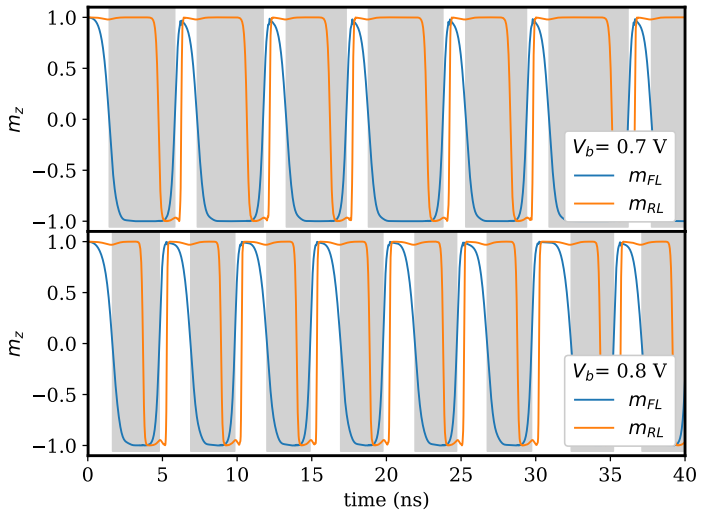

Figure 28: Dynamics of the out-of-plane component of free and reference layer for stack A at $V_b = 0.7$ V and $V_b = 0.8$ V. If the voltage would be cut, $\boldsymbol{m}_{\mathrm{RL}}$ would always relax into the z-direction. Grey regions mark time intervals in which cutting of the voltage spontaneously would lead to an uncoupled $\boldsymbol{m}_{\mathrm{FL}}$ to relax into the negative z-direction and thus to an successful P $\rightarrow$ AP switching.

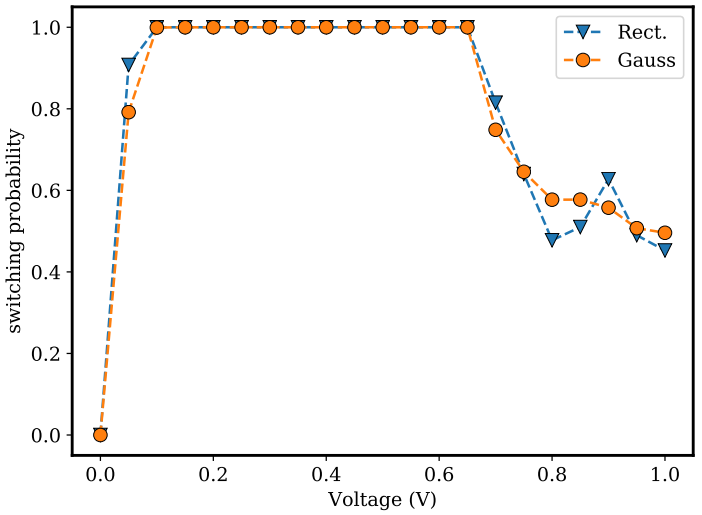

Figure 29: P $\rightarrow$ AP switching probability for stack A, assuming the switching pulse duration is Gaussian (rectangular) distributed with $\mu = 18$ ns and $\sigma = 4$ ns ($\mu = 18$ ns and $L = 8$ ns).

7 Conclusion

Within this thesis, we have discussed spin torque in spintronic devices on the mesoscopic scale in two different transport regimes. The first is the diffusive regime in which transport is dominated by scattering. In this regime, the dynamics of the spin-accumulation can be described by the micromagnetic spin-drift diffusion model, which can be coupled self-consistently with the Landau-Lifshitz-Gilbert equation to describe the magnetization dynamics in conjunction with the flow of charge and spin. We gave an overview over the torques arising from this modeling in two common spintronic device working principles, spin-transfer torque and spin-orbit torque. By comparison with experiments, we then discussed how spin-orbit torque can be used to modify the effective damping of an oscillating magnetization in a Pt/Co/Ta stack with perpendicular magnetic anisotropy. It was found that the form of the damping modification dependents on the direction of the in-plane component of an applied external field. The effective damping was found to change linearly with the applied current when the in-plane field is collinear with the polarization of the spins injected into the ferromagnetic layer i.e. if the in-plane field is perpendicular to the in-plane current while the dependence appeared quadratic for the case of the in-plane field being directed along the current direction.

We then shifted our attention to the coherent or ballistic transport regime in which the movement of the spin carrying free electrons is governed by the Schrödinger equation. We used the non-equilibrium Green's function formalism to calculate the spin-accumulation and spin-current in magnetic tunnel junctions and presented a computationally efficient strategy to couple the torques obtained from this model to magnetization dynamics simulations. Finally, we employed these coupled simulations to investigate the back-hopping effect in STT-MRAM cells. We compared two possible origins, the quadratic nature of the dampinglike torque term and the destabilization of the reference system and showed that the latter gives rise to the back and forth between the high and low resistance state of the tunnel junction. This appears consistent with most measurements on the subject while the former would result in an additional hysteresis loop at one voltage branch.

References

[1] E. E. Fullerton and J. R. Childress. *Spintronics, Magnetoresistive Heads, and the Emergence of the Digital World*. Proceedings of the IEEE, **104**(10), pp. 1787, 2016. doi:10.1109/JPROC.2016.2567778.

[2] C. Tsang, M.-M. Chen, T. Yogi and K. Ju. *Gigabit density recording using dual-element MR/inductive heads on thin-film disks*. IEEE Transactions on Magnetics, **26**(5), pp. 1689, 1990. doi:10.1109/20.104493.

[3] G. Binasch, P. Grünberg, F. Saurenbach and W. Zinn. *Enhanced magnetoresistance in layered magnetic structures with antiferromagnetic interlayer exchange*. Phys. Rev. B, **39**, pp. 4828, 1989. doi:10.1103/PhysRevB.39.4828.

[4] M. N. Baibich, J. M. Broto, A. Fert, F. N. Van Dau, F. Petroff, P. Etienne, G. Creuzet, A. Friederich and J. Chazelas. *Giant Magnetoresistance of (001)Fe/(001)Cr Magnetic Superlattices*. Phys. Rev. Lett., **61**, pp. 2472, 1988. doi:10.1103/PhysRevLett.61.2472.

[5] B. Dieny, V. Speriosu, B. Gurney, S. Parkin, D. Wilhoit, K. Roche, S. Metin, D. Peterson and S. Nadimi. *Spin-valve effect in soft ferromagnetic sandwiches*. Journal of Magnetism and Magnetic Materials, **93**, pp. 101, 1991. doi:https://doi.org/10.1016/0304-8853(91)90311-W.

[6] B. Dieny, V. S. Speriosu, S. Metin, S. S. P. Parkin, B. A. Gurney, P. Baumgart and D. R. Wilhoit. *Magnetotransport properties of magnetically soft spin-valve structures (invited)*. Journal of Applied Physics, **69**(8), pp. 4774, 1991. doi:10.1063/1.348252.

[7] B. Dieny, V. S. Speriosu, S. S. P. Parkin, B. A. Gurney, D. R. Wilhoit and D. Mauri. *Giant magnetoresistive in soft ferromagnetic multilayers*. Phys. Rev. B, **43**, pp. 1297, 1991. doi:10.1103/PhysRevB.43.1297.

[8] B. Dieny. *Giant magnetoresistance in spin-valve multilayers*. Journal of Magnetism and Magnetic Materials, **136**(3), pp. 335, 1994. doi:https://doi.org/10.1016/0304-8853(94)00356-4.

[9] D. Heim, R. Fontana, C. Tsang, V. Speriosu, B. Gurney and M. Williams. *Design and operation of spin valve sensors*. IEEE Transactions on Magnetics, **30**(2), pp. 316, 1994. doi:10.1109/20.312279.

[10] C. Tsang, R. Fontana, T. Lin, D. Heim, V. Speriosu, B. Gurney and M. Williams. *Design, fabrication and testing of spin-valve read heads for high density recording*. IEEE Transactions on Magnetics, **30**(6), pp. 3801, 1994. doi:10.1109/20.333909.

[11] S. Bhatti, R. Sbiaa, A. Hirohata, H. Ohno, S. Fukami and S. Piramanayagam. *Spintronics based random access memory: a review.* Materials Today, **20**(9), pp. 530, 2017. doi:https://doi.org/10.1016/j.mattod.2017.07.007.

[12] S. S. Parkin, C. Kaiser, A. Panchula, P. M. Rice, B. Hughes, M. Samant and S.-H. Yang. *Giant tunnelling magnetoresistance at room temperature with MgO (100) tunnel barriers.* Nature materials, **3**(12), pp. 862, 2004. doi: https://doi.org/10.1038/nmat1256.

[13] M. Julliere. *Tunneling between ferromagnetic films.* Physics Letters A, **54**(3), pp. 225, 1975. doi:https://doi.org/10.1016/0375-9601(75)90174-7.

[14] T. Miyazaki and N. Tezuka. *Giant magnetic tunneling effect in $Fe/Al_2O_3/Fe$ junction.* Journal of Magnetism and Magnetic Materials, **139**(3), pp. L231, 1995. doi:https://doi.org/10.1016/0304-8853(95)90001-2.

[15] J. S. Moodera, L. R. Kinder, T. M. Wong and R. Meservey. *Large Magnetoresistance at Room Temperature in Ferromagnetic Thin Film Tunnel Junctions.* Phys. Rev. Lett., **74**, pp. 3273, 1995. doi:10.1103/PhysRevLett.74.3273.

[16] H. J. Richter. *The transition from longitudinal to perpendicular recording.* Journal of Physics D: Applied Physics, **40**(9), pp. R149, 2007. doi:10.1088/0022-3727/40/9/r01.

[17] J. C. Slonczewski. *Conductance and exchange coupling of two ferromagnets separated by a tunneling barrier.* Phys. Rev. B, **39**, pp. 6995, 1989. doi: 10.1103/PhysRevB.39.6995.

[18] L. Berger. *Emission of spin waves by a magnetic multilayer traversed by a current.* Phys. Rev. B, **54**, pp. 9353, 1996. doi:10.1103/PhysRevB.54.9353.

[19] J. Slonczewski and J. Sun. *Theory of voltage-driven current and torque in magnetic tunnel junctions.* Journal of Magnetism and Magnetic Materials, **310**(2, Part 1), pp. 169, 2007. doi:https://doi.org/10.1016/j.jmmm.2006.10.507. Proceedings of the 17th International Conference on Magnetism.

[20] Y. Huai, F. Albert, P. Nguyen, M. Pakala and T. Valet. *Observation of spin-transfer switching in deep submicron-sized and low-resistance magnetic tunnel junctions.* Applied Physics Letters, **84**(16), pp. 3118, 2004. doi:10.1063/1.1707228.

[21] Y. Huai. *Spin-transfer torque MRAM (STT-MRAM): Challenges and prospects.* AAPPS Bulletin, **18**, 2008.

[22] C. Caroli, R. Combescot, P. Nozieres and D. Saint-James. *Direct calculation*

of the tunneling current. Journal of Physics C: Solid State Physics, **4**(8), pp. 916, 1971. doi:10.1088/0022-3719/4/8/018.

[23] I. Theodonis, N. Kioussis, A. Kalitsov, M. Chshiev and W. H. Butler. *Anomalous Bias Dependence of Spin Torque in Magnetic Tunnel Junctions*. Phys. Rev. Lett., **97**, p. 237205, 2006. doi:10.1103/PhysRevLett.97.237205.

[24] A. Manchon, N. Ryzhanova, A. Vedyayev, M. Chschiev and B. Dieny. *Description of current-driven torques in magnetic tunnel junctions*. Journal of Physics: Condensed Matter, **20**(14), p. 145208, 2008. doi:10.1088/0953-8984/20/14/145208.

[25] A. Kalitsov, M. Chshiev, I. Theodonis, N. Kioussis and W. H. Butler. *Spin-transfer torque in magnetic tunnel junctions*. Phys. Rev. B, **79**, p. 174416, 2009. doi:10.1103/PhysRevB.79.174416.

[26] M. Chshiev, A. Manchon, A. Kalitsov, N. Ryzhanova, A. Vedyayev, N. Strelkov, W. H. Butler and B. Dieny. *Analytical description of ballistic spin currents and torques in magnetic tunnel junctions*. Phys. Rev. B, **92**, p. 104422, 2015. doi:10.1103/PhysRevB.92.104422.

[27] H. Kubota, A. Fukushima, K. Yakushiji, T. Nagahama, S. Yuasa, K. Ando, H. Maehara, Y. Nagamine, K. Tsunekawa, D. D. Djayaprawira, N. Watanabe and Y. Suzuki. *Quantitative measurement of voltage dependence of spin-transfer torque in MgO-based magnetic tunnel junctions*. Nature Physics, **4**(1), pp. 37, 2008. doi:10.1038/nphys784.

[28] D. Datta, B. Behin-Aein, S. Salahuddin and S. Datta. *Quantitative Model for TMR and Spin-transfer Torque in MTJ devices*. In *2010 IEEE International Electron Devices Meeting (IEDM)*, pp. 22.8.1 – 22.8.4. 2011. doi:10.1109/IEDM.2010.5703417.

[29] S. Zhang, P. M. Levy and A. Fert. *Mechanisms of Spin-Polarized Current-Driven Magnetization Switching*. Phys. Rev. Lett., **88**, p. 236601, 2002. doi:10.1103/PhysRevLett.88.236601.

[30] S. Salahuddin and S. Datta. *Self-consistent simulation of quantum transport and magnetization dynamics in spin-torque based devices*. Applied Physics Letters, **89**(15), p. 153504, 2006. doi:10.1063/1.2359292.

[31] S.-C. Oh, S.-Y. Park, A. Manchon, M. Chshiev, J. Han, H.-W. Lee, J.-E. Lee, K.-T. Nam, Y. Jo, Y.-C. Kong, B. Dieny and K.-J. Lee. *Bias-voltage dependence of perpendicular spin-transfer torque in asymmetric MgO-based magnetic tunnel junctions*. Nature Physics, **5**, p. 898, 2009. doi:10.1038/nphys1427.

[32] T. Min, J. Z. Sun, R. Beach, D. Tang and P. Wang. *Back-hopping after spin torque transfer induced magnetization switching in magnetic tunneling junction cells.* Journal of Applied Physics, **105**(7), p. 07D126, 2009. doi: 10.1063/1.3063672.

[33] M. Stiles and J. Miltat. *Spin Transfer Torque and Dynamics*, p. 225–308. Spin Dynamics in Confined Magnetic Structures III: Topics in Applied Physics 101, Springer Berlin / Heidelberg, Heidelberg, DE, 2006.

[34] P. M. Haney, H.-W. Lee, K.-J. Lee, A. Manchon and M. D. Stiles. *Current induced torques and interfacial spin-orbit coupling: Semiclassical modeling.* Phys. Rev. B, **87**, p. 174411, 2013. doi:10.1103/PhysRevB.87.174411.

[35] A. Manchon, J. Železný, I. M. Miron, T. Jungwirth, J. Sinova, A. Thiaville, K. Garello and P. Gambardella. *Current-induced spin-orbit torques in ferromagnetic and antiferromagnetic systems.* Rev. Mod. Phys., **91**, p. 035004, 2019. doi:10.1103/RevModPhys.91.035004.

[36] I. Mihai Miron, G. Gaudin, S. Auffret, B. Rodmacq, A. Schuhl, S. Pizzini, J. Vogel and P. Gambardella. *Current-driven spin torque induced by the Rashba effect in a ferromagnetic metal layer.* Nature materials, **9**(3), pp. 230, 2010.

[37] L. Liu, T. Moriyama, D. C. Ralph and R. A. Buhrman. *Spin-Torque Ferromagnetic Resonance Induced by the Spin Hall Effect.* Phys. Rev. Lett., **106**, p. 036601, 2011. doi:10.1103/PhysRevLett.106.036601.

[38] L. Liu, C.-F. Pai, Y. Li, H. W. Tseng, D. C. Ralph and R. A. Buhrman. *Spin-Torque Switching with the Giant Spin Hall Effect of Tantalum.* Science, **336**(6081), pp. 555, 2012. doi:10.1126/science.1218197.

[39] S. Emori, T. Nan, A. M. Belkessam, X. Wang, A. D. Matyushov, C. J. Babroski, Y. Gao, H. Lin and N. X. Sun. *Interfacial spin-orbit torque without bulk spin-orbit coupling.* Phys. Rev. B, **93**, p. 180402, 2016. doi: 10.1103/PhysRevB.93.180402.

[40] L. Liu, O. J. Lee, T. J. Gudmundsen, D. C. Ralph and R. A. Buhrman. *Current-Induced Switching of Perpendicularly Magnetized Magnetic Layers Using Spin Torque from the Spin Hall Effect.* Phys. Rev. Lett., **109**, p. 096602, 2012. doi:10.1103/PhysRevLett.109.096602.

[41] J. E. Hirsch. *Spin Hall Effect.* Phys. Rev. Lett., **83**, pp. 1834, 1999. doi: 10.1103/PhysRevLett.83.1834.

[42] Y. Niimi and Y. Otani. *Reciprocal spin Hall effects in conductors with strong*

spin–orbit coupling: a review. Reports on progress in physics, **78**(12), p. 124501, 2015.

[43] A. M. Humphries, T. Wang, E. R. J. Edwards, S. R. Allen, J. M. Shaw, H. T. Nembach, J. Q. Xiao, T. J. Silva and X. Fan. *Observation of spin-orbit effects with spin rotation symmetry.* Nature Communications, **8**(1), p. 911, 2017.

[44] R. Ramaswamy, J. M. Lee, K. Cai and H. Yang. *Recent advances in spin-orbit torques: Moving towards device applications.* Applied Physics Reviews, **5**(3), p. 031107, 2018. doi:10.1063/1.5041793.

[45] H. Ishizuka and N. Nagaosa. *Large anomalous Hall effect and spin Hall effect by spin-cluster scattering in the strong-coupling limit.* Phys. Rev. B, **103**, p. 235148, 2021. doi:10.1103/PhysRevB.103.235148.

[46] A. Ghosh, K. Garello, C. Avci, M. Gabureac and P. Gambardella. *Interface enhanced spin-orbit torques and current-induced magnetization switching of Pd/Co/AlO_x layers.* Physical Review Applied, **7**, 2017. doi:10.1103/PhysRevApplied.7.014004.

[47] M.-H. Nguyen, D. C. Ralph and R. A. Buhrman. *Spin Torque Study of the Spin Hall Conductivity and Spin Diffusion Length in Platinum Thin Films with Varying Resistivity.* Phys. Rev. Lett., **116**, p. 126601, 2016. doi:10.1103/PhysRevLett.116.126601.

[48] X. Tao, Q. Liu, B. Miao, R. Yu, Z. Feng, L. Sun, B. You, J. Du, K. Chen, S. Zhang et al. *Self-consistent determination of spin Hall angle and spin diffusion length in Pt and Pd: The role of the interface spin loss.* Science advances, **4**(6), p. eaat1670, 2018.

[49] C. Abert. *Micromagnetics and spintronics: models and numerical methods.* The European Physical Journal B, **92**(6), pp. 1, 2019.

[50] L. Landau and E. Lifshitz. *3 - On the theory of the dispersion of magnetic permeability in ferromagnetic bodies, Reprinted from Physikalische Zeitschrift der Sowjetunion 8, Part 2, 153, 1935.* In L. PITAEVSKI (editor), *Perspectives in Theoretical Physics*, pp. 51–65. Pergamon, Amsterdam, 1992.

[51] T. L. Gilbert. *A Lagrangian formulation of the gyromagnetic equation of the magnetization field.* Phys. Rev., **100**, p. 1243, 1955.

[52] W. Brown Jr. *Micromagnetics.* New York, 1963.

[53] A. Aharoni. *Magnetostatic energy calculations.* IEEE Transactions on Magnetics, **27**(4), pp. 3539, 1991. doi:10.1109/20.102925.

[54] A. Aharoni et al. *Introduction to the Theory of Ferromagnetism*. Clarendon Press, 2000.

[55] T. Kasuya. *A Theory of Metallic Ferro- and Antiferromagnetism on Zener's Model*. Progress of Theoretical Physics, **16**(1), pp. 45, 1956. doi:10.1143/PTP.16.45.

[56] K. Yosida. *Magnetic Properties of Cu-Mn Alloys*. Phys. Rev., **106**, pp. 893, 1957. doi:10.1103/PhysRev.106.893.

[57] C. Abert, L. Exl, F. Bruckner, A. Drews and D. Suess. *magnum.fe: A micromagnetic finite-element simulation code based on FEniCS*. Journal of Magnetism and Magnetic Materials, **345**, pp. 29 , 2013. doi:https://doi.org/10.1016/j.jmmm.2013.05.051.

[58] G. S. Abo, Y. Hong, J. Park, J. Lee, W. Lee and B. Choi. *Definition of Magnetic Exchange Length*. IEEE Transactions on Magnetics, **49**(8), pp. 4937, 2013. doi:10.1109/TMAG.2013.2258028.

[59] J. Slonczewski. *Currents and torques in metallic magnetic multilayers*. Journal of Magnetism and Magnetic Materials, **247**(3), pp. 324, 2002. doi:https://doi.org/10.1016/S0304-8853(02)00291-3.

[60] J. Xiao, A. Zangwill and M. D. Stiles. *Macrospin models of spin transfer dynamics*. Phys. Rev. B, **72**, p. 014446, 2005. doi:10.1103/PhysRevB.72.014446.

[61] K. Garello, I. Miron, C. Avci, F. Freimuth, Y. Mokrousov, S. Blügel, S. Auffret, O. Boulle, G. Gaudin and P. Gambardella. *Symmetry and magnitude of spin-orbit torques in ferromagnetic heterostructures*. Nature nanotechnology, **8**, 2013. doi:10.1038/nnano.2013.145.

[62] M. Hayashi, J. Kim, M. Yamanouchi and H. Ohno. *Quantitative characterization of the spin-orbit torque using harmonic Hall voltage measurements*. Phys. Rev. B, **89**, p. 144425, 2014. doi:10.1103/PhysRevB.89.144425.

[63] S. Dutta, A. Bose, A. A. Tulapurkar, R. A. Buhrman and D. C. Ralph. *Interfacial and bulk spin Hall contributions to fieldlike spin-orbit torque generated by iridium*. Phys. Rev. B, **103**, p. 184416, 2021. doi:10.1103/PhysRevB.103.184416.

[64] M. Dyakonov and V. Perel. *Current-induced spin orientation of electrons in semiconductors*. Physics Letters A, **35**(6), pp. 459, 1971. doi:https://doi.org/10.1016/0375-9601(71)90196-4.

[65] S. Saha, P. Flauger, C. Abert, A. Hrabec, Z. Luo, J. Zhou, V. Scagnoli,

D. Suess and L. J. Heyderman. *Control of damping in perpendicularly magnetized thin films using spin-orbit torques.* Phys. Rev. B, **101**, p. 224401, 2020. doi:10.1103/PhysRevB.101.224401.

[66] S. Saha, R. Mandal, S. Barman, D. Kumar, B. Rana, Y. Fukuma, S. Sugimoto, Y. Otani and A. Barman. *Tunable Magnonic Spectra in Two-Dimensional Magnonic Crystals with Variable Lattice Symmetry.* Advanced Functional Materials, **23**(19), pp. 2378, 2013. doi:https://doi.org/10.1002/adfm.201202545.

[67] S. Pal, B. Rana, O. Hellwig, T. Thomson and A. Barman. *Tunable magnonic frequency and damping in [Co/Pd]8 multilayers with variable Co layer thickness.* Applied Physics Letters, **98**(8), p. 082501, 2011. doi:10.1063/1.3559222.

[68] S. Mondal, S. Choudhury, N. Jha, A. Ganguly, J. Sinha and A. Barman. *All-optical detection of the spin Hall angle in* W/CoFeB/SiO_2 *heterostructures with varying thickness of the tungsten layer.* Phys. Rev. B, **96**, p. 054414, 2017. doi:10.1103/PhysRevB.96.054414.

[69] R. K. Mains, I. Mehdi and G. I. Haddad. *Effect of spatially variable effective mass on static and dynamic properties of resonant tunneling devices.* Applied Physics Letters, **55**(25), pp. 2631, 1989. doi:10.1063/1.101958.

[70] S. Datta. *Nanoscale device modeling: the Green's function method.* Superlattices and Microstructures, **28**(4), pp. 253 , 2000. doi:https://doi.org/10.1006/spmi.2000.0920.

[71] A. A. Yanik, G. Klimeck and S. Datta. *Quantum transport with spin dephasing: A nonequlibrium Green's function approach.* Phys. Rev. B, **76**, p. 045213, 2007. doi:10.1103/PhysRevB.76.045213.

[72] S. Datta. *Electronic Transport in Mesoscopic Systems.* Cambridge Studies in Semiconductor Physics and Microelectronic Engineering. Cambridge University Press, 1 edition, 1995.

[73] M. Paulsson. *Non equilibrium green's functions for dummies: Introduction to the one particle NEGF equations.* arXiv preprint cond-mat/0210519, 2002. doi:10.48550/arXiv.cond-mat/0210519.

[74] D. Datta, H. Dixit, S. Agarwal, A. Dasgupta, M. Tran, D. Houssameddine, Y. S. Chauhan, D. Shum and F. Benistant. *Quantitative model for switching asymmetry in perpendicular MTJ: A material-device-circuit co-design.* In *2017 IEEE International Electron Devices Meeting (IEDM)*, pp. 31.5.1–31.5.4. 2017. doi:10.1109/IEDM.2017.8268482.

[75] K. Y. Camsari, S. Ganguly, D. Datta and S. Datta. *Non-Equilibrium Green's*

Function Based Circuit Models for Coherent Spin Devices. IEEE Transactions on Nanotechnology, **18**, pp. 858, 2019. doi:10.1109/TNANO.2018.2889443.

[76] D. Wang, C. Nordman, J. Daughton, Z. Qian and J. Fink. *70% TMR at room temperature for SDT sandwich junctions with CoFeB as free and reference Layers*. IEEE Transactions on Magnetics, **40**(4), pp. 2269, 2004. doi:10.1109/TMAG.2004.830219.

[77] S. Ringer, M. Vieth, L. Bär, M. Rührig and G. Bayreuther. *Conductance anomalies of CoFeB/MgO/CoFeB magnetic tunnel junctions*. Phys. Rev. B, **90**, p. 174401, 2014. doi:10.1103/PhysRevB.90.174401.

[78] K. Ogata, Y. Nakayama, G. Xiao and H. Kaiju. *Observation and theoretical calculations of voltage-induced large magnetocapacitance beyond 330% in MgO-based magnetic tunnel junctions*. Scientific reports, **11**(1), pp. 1, 2021.

[79] C. Tiusan, J. Faure-Vincent, C. Bellouard, M. Hehn, E. Jouguelet and A. Schuhl. *Interfacial Resonance State Probed by Spin-Polarized Tunneling in Epitaxial* Fe/MgO/Fe *Tunnel Junctions*. Phys. Rev. Lett., **93**, p. 106602, 2004. doi:10.1103/PhysRevLett.93.106602.

[80] A. Thomas, D. Meyners, D. Ebke, N.-N. Liu, M. D. Sacher, J. Schmalhorst, G. Reiss, H. Ebert and A. Hütten. *Inverted spin polarization of Heusler alloys for spintronic devices*. Applied Physics Letters, **89**(1), p. 012502, 2006. doi:10.1063/1.2219333.

[81] H. Jaffrès, D. Lacour, F. Nguyen Van Dau, J. Briatico, F. Petroff and A. Vaurès. *Angular dependence of the tunnel magnetoresistance in transition-metal-based junctions*. Phys. Rev. B, **64**, p. 064427, 2001. doi:10.1103/PhysRevB.64.064427.

[82] A. Kalitsov, I. Theodonis, N. Kioussis, M. Chshiev, W. H. Butler and A. Vedyayev. *Spin-polarized current-induced torque in magnetic tunnel junctions*. Journal of Applied Physics, **99**(8), p. 08G501, 2006. doi:10.1063/1.2151796.

[83] M. Chshiev, I. Theodonis, A. Kalitsov, N. Kioussis and W. Butler. *Voltage Dependence of Spin Transfer Torque In Magnetic Tunnel Junctions*. Magnetics, IEEE Transactions on, **44**, pp. 2543 , 2008. doi:10.1109/TMAG.2008.2002605.

[84] J. C. Sankey, Y.-T. Cui, J. Z. Sun, J. C. Slonczewski, R. A. Buhrman and D. C. Ralph. *Measurement of the spin-transfer-torque vector in magnetic tunnel junctions*. Nature Physics, **4**(1), pp. 67, 2008. doi:10.1038/nphys783.

[85] P. Bruno. *Theory of interlayer magnetic coupling.* Phys. Rev. B, **52**, pp. 411, 1995. doi:10.1103/PhysRevB.52.411.

[86] W. Skowroński, T. Stobiecki, J. Wrona, K. Rott, A. Thomas, G. Reiss and S. van Dijken. *Interlayer exchange coupling and current induced magnetization switching in magnetic tunnel junctions with MgO wedge barrier.* Journal of Applied Physics, **107**(9), p. 093917, 2010.

[87] B. D. Schrag, A. Anguelouch, S. Ingvarsson, G. Xiao, Y. Lu, P. L. Trouilloud, A. Gupta, R. A. Wanner, W. J. Gallagher, P. M. Rice and S. S. P. Parkin. *Néel "orange-peel" coupling in magnetic tunneling junction devices.* Applied Physics Letters, **77**(15), pp. 2373, 2000. doi:10.1063/1.1315633.

[88] P. W. T. Pong, C. L. Dennis, A. Castillo, A. Chen and W. F. Egelhoff. *Detection of pinholes in magnetic tunnel junctions by magnetic coupling.* Journal of Applied Physics, **103**(7), p. 07A902, 2008. doi:10.1063/1.2829018.

[89] T. Katayama, S. Yuasa, J. Velev, M. Y. Zhuravlev, S. S. Jaswal and E. Y. Tsymbal. *Interlayer exchange coupling in Fe/MgO/Fe magnetic tunnel junctions.* Applied Physics Letters, **89**(11), p. 112503, 2006. doi:10.1063/1.2349321.

[90] P. Flauger, C. Abert and D. Suess. *Efficient solution strategy to couple micromagnetic simulations with ballistic transport in magnetic tunnel junctions.* Phys. Rev. B, **105**, p. 134407, 2022. doi:10.1103/PhysRevB.105.134407.

[91] T. Devolder, O. Bultynck, P. Bouquin, V. D. Nguyen, S. Rao, D. Wan, B. Sorée, I. P. Radu, G. S. Kar and S. Couet. *Back hopping in spin transfer torque switching of perpendicularly magnetized tunnel junctions.* Phys. Rev. B, **102**, p. 184406, 2020. doi:10.1103/PhysRevB.102.184406.

[92] Z. Hou, Y. Liu, S. Cardoso, P. P. Freitas, H. Chen and C.-R. Chang. *Dynamics of the reference layer driven by spin-transfer torque: Analytical versus simulation model.* Journal of Applied Physics, **109**(11), p. 113914, 2011.

[93] C. Safranski and J. Z. Sun. *Interface moment dynamics and its contribution to spin-transfer torque switching process in magnetic tunnel junctions.* Phys. Rev. B, **100**, p. 014435, 2019. doi:10.1103/PhysRevB.100.014435.

[94] C. Abert, H. Sepehri-Amin, F. Bruckner, C. Vogler, M. Hayashi and D. Suess. *Back-Hopping in Spin-Transfer-Torque Devices: Possible Origin and Countermeasures.* Phys. Rev. Applied, **9**, p. 054010, 2018. doi:10.1103/PhysRevApplied.9.054010.